Supporting information

Construction of ratiometric optical thermometers by linking chiral cyclometalated dicyanidoiridates(III) with europium(III) luminophores into cluster compounds

Jan Rzepiela,[a,b] Mikolaj Zychowicz,[a,b] Jakub J. Zakrzewski,[a] Shin-ichi Ohkoshi,[c] Sebastian Baś,[a] and Szymon Chorazy*[a]

[a]Faculty of Chemistry, Jagiellonian University, Gronostajowa 2, 30-387 Kraków, Poland. [b]Jagiellonian University, Doctoral School of Exact and Natural Sciences, Łojasiewicza 11, 30-348 Kraków, Poland. [c]Department of Chemistry, School of Science, The University of Tokyo, 7-3-1 Hongo, Bunkyo-ku, Tokyo 113-0033, Japan
*Corresponding author: simon.chorazy@uj.edu.pl

Experimental details

Materials

Iridium(III) chloride hydrate, 4-fluoroacetophenone, (*R,S*)-myrtenal, and bromine were purchased from Sigma-Aldrich and used without any purification. All other common reagents and solvents were purchased from Sigma-Aldrich or TCI Chemicals and used as received unless otherwise noted. The reagents used for the preparation of previously reported compounds (*R*,*R*-pinppyH and ***R*,*R*-Ir**) are described in Ref. S1.

Synthesis of 2-phenyl-4,5-pinenopyridine (*R*,*R*-pinppyH) and TBA[$\mathrm{Ir^{III}(CN)_2}$(*R*,*R*-pinppy)$_2$]·2MeCN (*R*,*R*-Ir)

The TBA[$\mathrm{Ir^{III}(CN)_2}$(*R*,*R*-pinppy)$_2$]·2MeCN (***R*,*R*-Ir**, TBA = tetrabutylammonium, *R*,*R*-pinppy = carbanion of (*R*,*R*)-2-phenyl-4,5-pinenopyridine) hybrid salt, further used for the synthesis of one of the reported heterometallic molecular assemblies (i.e., **$\mathrm{Eu_2Ir_2}$**, see below), was prepared starting from the (*R*,*R*)-2-phenyl-4,5-pinenopyridine (*R*,*R*-pinppyH) organic precursor. Both the ***R*,*R*-Ir** salt as well as the *R*,*R*-pinppyH precursor were obtained following the recently published procedures.[S1]

Synthesis of 2-(4-fluorophenyl)-4,5-pinenopyridine (*R*,*R*-FpinppyH)

The solution of 4-fluoroacetophenone (**P1**, see scheme below; 15.0 g, 109 mmol, i.e., 13.18 mL, 1.0 eq.) in 50 mL of acetic acid was prepared and cooled to 0 °C. Then, at this decreased temperature, bromine (19.7 g, 120 mmol, i.e., 6.15 mL, 1.1 eq.) was added dropwise. While still keeping 0 °C, the reaction was mixed for 20 minutes and then allowed to warm up to room temperature. After the resulting disappearance of the red color, the reaction mixture was diluted with dichloromethane (dcm) and extracted carefully with the 3 M NaOH solution. The organic layers were dried over $\mathrm{MgSO_4}$, filtered, and evaporated to dryness. The obtained residue was dissolved in 50 ml of dcm and pyridine (12.9 g, 164 mmol, i.e., 13.2 mL, 1.5 eq.) was added. Then, the reaction mixture was mixed overnight. The precipitated product (**P2**, see scheme below) was filtered off, washed with diethyl ether, and dried. It was used in the next step without further purification or characterization. Yield: 28.7 g (89%).

To the Ace pressure vessel, the solution of **P2** (10.85 g, 36.6 mmol, 1.1 eq) and $\mathrm{NH_4OAc}$ (5.13 g, 66.6 mmol, 2.0 eq) in 100 mL of anhydrous ethanol was added. To this mixture, the (*R,S*)-myrtenal precursor (5.0 g, 33.3 mmol, i.e., 5.05 mL, 1.0 eq) was added. Then, the pressure vessel was closed and heated to 110 °C overnight. After cooling, the reaction mixture was diluted with dcm (300 mL). The precipitated solid was filtered on a silica pad, and the resulting solution was washed three times with water. The organic layers were dried over anhydrous sodium sulfate, evaporated, and purified by column chromatography of silica gel (Hx:AcOEt, 95:5) to give the final pure product of 2-(4-fluorophenyl)-4,5-pinenopyridine (*R*,*R*-FpinppyH, see scheme below). Yield: 8.90 g (72 %). Single crystals for XRD studies were obtained by cooling the saturated solution of the powder sample of *R*,*R*-FpinppyH in pentane to 0 °C overnight.

Rf: 0.29 (Hx:AcOEt, 95:5)

^{1}H NMR (400 MHz, $\mathrm{CDCl_3}$, $\mathrm{Me_4Si}$) δ 8.19 (s, 1H), 7.97 – 7.90 (m, 2H), 7.45 (s, 1H), 7.16 – 7.07 (m, 2H), 3.00 (d, J = 2.6 Hz, 2H), 2.84 (t, J = 5.5 Hz, 1H), 2.70 (dt, J = 9.6, 5.8 Hz, 1H), 2.30 (tt, J = 5.8, 2.8 Hz, 1H), 1.41 (s, 3H), 1.22 (d, J = 9.6 Hz, 1H), 0.65 (s, 3H).

^{13}C{^{1}H} NMR (101 MHz, $\mathrm{CDCl_3}$, $\mathrm{Me_4Si}$) δ 163.3 (d, J = 247.4 Hz), 154.7, 146.0, 145.4, 141.2, 136.1, 128.5 (d, J = 8.2 Hz), 119.8, 115.6 (d, J = 21.5 Hz), 44.4, 40.2, 39.4, 33.0, 32.0, 26.1, 21.5. ^{13}C NMR spectrum was not decoupled from fluorine.

The scheme below visualizes the whole synthetic pathway leading to enantiopure *R*,*R*-FpinppyH.

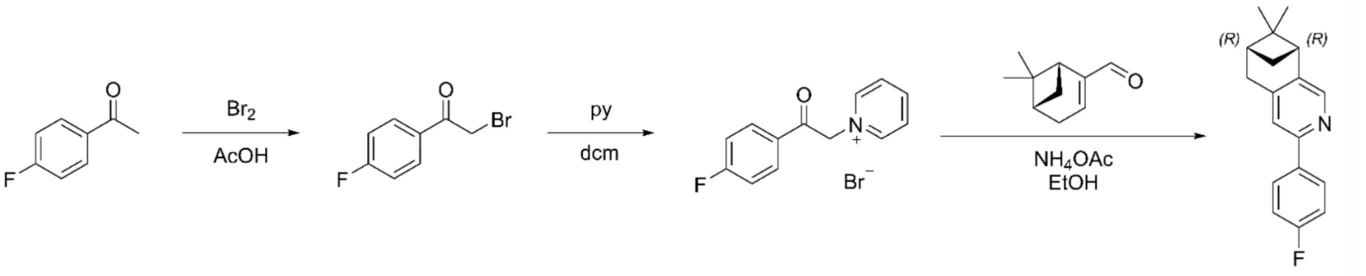

P1 **P2** ***R*,*R*-FpinppyH**

Synthesis of TBA[$\mathrm{Ir^{III}(CN)_2}$(*R*,*R*-Fpinppy)$_2$]·2MeCN (*R*,*R*-FIr)

The three-step synthesis of ***R*,*R*-FIr** started by mixing iridium(III) chloride hydrate (200 mg, 0.67 mmol, 1.0 eq) and *R*,*R*-FpinppyH (450 mg, 1.68 mmol, 2.5eq) in a mixture of 15 mL of ethoxyethanol and 5 mL of water. After 24 h of refluxing this mixture, the product of [$\mathrm{Ir^{III}_2(\mu_2\text{-}Cl)_2}$(*R*,*R*-Fpinppy)$_4$][S1] was precipitated with water, filtered on a sintered glass funnel, washed subsequently with water and pentane, then dried. Yield: 436 mg, about 90%.

In the second step, the as-prepared powder sample of [$\mathrm{Ir^{III}_2(\mu_2\text{-}Cl)_2}$(*R*,*R*-Fpinppy)$_4$] (436 mg, 0.30 mmol, 1 eq) was dissolved in the mixture of methanol (100 mL) and dcm (50 mL). Then, KCN (80 mg, 1.23 mmol, 4.1 eq) was added, and the reaction mixture was refluxed for 24 h. After being cooled, the reaction mixture was filtered, and the resulting filtrate was evaporated to dryness. The resulting potassium salt of the objective Ir(III) complex, i.e., K[$Ir^{III}(CN)_2$(*R*,*R*-Fpinppy)$_2$] was dried and used directly in the last step.

The entire product was dissolved in 100 mL of methanol, and 215 mg of tetrabutylammonium (TBA) perchlorate (0.63 mmol, ca. two times the excess) was added. The resulting mixture was refluxed for 24 h, and the resulting precipitate was filtered. The filtrate was evaporated to dryness, dissolved in a small amount of chloroform, filtered, and the product was precipitated with diethyl ether. The last two steps resulted in 560 mg (yield of ca. 95 %) of yellow powder of the objective Ir(III) complex in the form of an organic salt. A single crystal of ***R,R*-FIr** was obtained by slow diffusion of diethyl ether into the acetonitrile (MeCN) solution of the respective originally obtained powder sample. Its composition of TBA[$Ir^{III}(CN)_2$(*R*,*R*-Fpinppy)$_2$]·2MeCN (***R,R*-FIr$^{\mathbf{solution}}$**, M_W = 1060.46 g·mol^{-1}) was determined by the single-crystal X-ray diffraction (SC-XRD) analysis. The crystals of ***R,R*-FIr$^{\mathbf{solution}}$** are hygroscopic and in the air atmosphere slowly lose the acetonitrile molecule and replace it with two water molecules, creating the hydrate form with the formula of TBA[$Ir^{III}(CN)_2$(*R*,*R*-Fpinppy)$_2$]·2H$_2$O (***R,R*-FIr**, M_W = 1055.54 g·mol^{-1}). This compositional change was confirmed by TGA and IR spectroscopy. Moreover, during this solvent exchange, the crystallinity of the product is not lost, and the phase purity and its air stability were proven by the powder X-ray diffraction (P-XRD) method. Elemental analysis calculated for the hydrated form, ***R,R*-FIr** ($C_{54}H_{76}F_2Ir_1N_5O_2$): C, 61.45 %; H, 7.07 %; N, 6,64 %. Found: C, 61.91 %; H, 7.14 %; N, 6.57 %. TG (Fig. S2) shows the loss of 2 H_2O molecules per formula unit. Calcd.: 3.41%; found: 3.51 %.

Synthesis of Eu$_2$Ir$_2$ cluster compound

The equimolar solution of freshly filtrated crystals of ***R,R*-Ir** (31 mg, 0.0315 mmol, 1.0 eq.) and europium(III) nitrate hexahydrate (14.1 mg, 0.0315 mmol, 1.0 eq.) in 2 mL of acetonitrile was prepared and slowly diffused with diethyl ether. After a few days, well-shaped yellow crystals of **Eu$_2$Ir$_2$** appeared. Yield: 37 mg (44%). Their composition of (TBA)$_2${[$Eu^{III}(NO_3)_3(H_2O)_{0.5}$]$_2$[$Ir^{III}(CN)_2$(*R*,*R*-pinppy)$_2$]$_2$}·2H$_2$O (**Eu$_2Ir_2$$^{\mathbf{solution}}$**, M_W = 2687.84 g·mol^{-1}) was determined by the SC-XRD analysis, while the purity of the phase and its air stability were proven by the P-XRD method. Exposure of **Eu$_2$Ir$_2$$^{\mathbf{solution}}$** in the air causes the stabilization of the tetrahydrate composition of (TBA)$_2${[$Eu^{III}(NO_3)_3(H_2O)_{0.5}$]$_2$[$Ir^{III}(CN)_2$(*R*,*R*-pinppy)$_2$]$_2$}·4H$_2$O (**Eu$_2Ir_2$**, M_W = 2714.85 g·mol^{-1}), without any structural transformation, which was confirmed by P-XRD, CHN elemental analysis, and TGA results. Elemental analysis calculated for the hydrated form, **Eu$_2$Ir$_2$** ($C_{108}H_{152}Ir_2Eu_2N_{16}O_{22}$): C, 47.78 %; H, 5.64 %; N, 8.26 %. Found: C, 48.23 %; H, 5.56 %; N, 8.19 %. TG (Fig. S2) shows the loss of 4 H_2O molecules per formula unit. Calcd.: 2.66 %; found: 3.12 %.

Synthesis of Eu$_2$FIr$_2$ cluster compound

The equimolar solution of freshly filtrated crystals of ***R,R*-FIr** (30 mg, 0.0284 mmol, 1.0 eq.) and europium(III) nitrate hexahydrate (12.7 mg, 0.0284 mmol, 1.0 eq.) in 2 mL of acetonitrile was prepared and slowly diffused by diethyl ether. After a few days, well-shaped yellow crystals of **Eu$_2$FIr$_2$** appeared. Yield 30 mg (39%). Their composition of (TBA)$_2${[$Eu^{III}(NO_3)_3(H_2O)_{0.5}$]$_2$[$Ir^{III}(CN)_2$(*R*,*R*-Fpinppy)$_2$]$_2$}·*n*H$_2$O (**Eu$_2FIr_2$$^{\mathbf{solution}}$**, M_W = 2732.77(+*n*H$_2$O) g·mol^{-1}) was proven by the comparison of P-XRD diffractograms with **Eu$_2$Ir$_2$** (as the related single crystals of the sufficient quality for the SC-XRD analysis were not obtained). The P-XRD data also confirm the phase purity and the air stability of the obtained material. Exposure of **Eu$_2$FIr$_2$$^{\mathbf{solution}}$** in the air causes the stabilization of the hexahydrate composition of (TBA)$_2${[$Eu^{III}(NO_3)_3(H_2O)_{0.5}$]$_2$[$Ir^{III}(CN)_2$(*R*,*R*-Fpinppy)$_2$]$_2$}·6H$_2$O (**Eu$_2FIr_2$**, M_W = 2822.85 g·mol^{-1}), without any structural transformation, which was confirmed by P-XRD, CHN elemental analysis, and TGA results. Elemental analysis calculated for the hydrated form, **Eu$_2$FIr$_2$·6H$_2$O** ($C_{108}H_{152}F_4Ir_2Eu_2N_{16}O_{24}$): C, 45.95 %; H, 5.43 %; N, 7.94 %. Found: C, 45.46 %; H, 5.36 %; N, 7.63 %. TG (Fig. S2) shows the loss of 6 H_2O molecules per formula unit. Calcd.: 3.83 %; found: 3.44 %.

Comment on the determination of the composition of Eu$_2$Ir$_2$ and Eu$_2$FIr$_2$ cluster compounds: It is worth discussing the method used for the precise determination of the composition of the two obtained cluster compounds of **Eu$_2$Ir$_2$** and **Eu$_2$FIr$_2$**. The first evidence on their composition was provided by the results of the SC-XRD data, which were successfully gathered and analyzed for **Eu$_2$Ir$_2$** (see Structural studies, as well as Fig. S5 and Table S1, below). The analogous analysis was unsuccessful for **Eu$_2$FIr$_2$**, but the P-XRD data proved that this compound is isostructural to **Eu$_2$Ir$_2$** (Fig. S6); thus, the conclusions from the SC-XRD analysis of **Eu$_2$Ir$_2$** were assumed to be valid for **Eu$_2$FIr$_2$**. From the SC-XRD data of **Eu$_2$Ir$_2$**, it can be undoubtedly stated that the molecular building unit (determined by taking into account the asymmetric unit and the symmetry elements) contains a single tetrametallic coordination (i.e., cyanido-bridged) cluster based on two Eu(III) and two Ir(III) complexes, i.e., {Eu$_2$Ir$_2$}. For each such molecular cluster, two positively charged TBA$^+$ cations are present in the crystal structure (Fig. S5 and S39). Despite the large structural disorder detected in the crystal structure in the remaining space between the mentioned molecular components, no additional TBA$^+$ cation may be present in the structure due to its too large size and the lack of residual electron densities that could suggest its presence. Thus, the remaining space is occupied by the weakly bonded solvent molecules of crystallization. Most probably, there are water molecules of crystallization, whose a few representative positions with partial occupancies were found. The other solvent used in the synthesis, i.e., acetonitrile, was not found in the SC-XRD data. There was also no sign of its presence in the results of other measurements, such as IR spectra (Fig. S1). Therefore, it can be concluded that the coordination $\{Eu_2Ir_2\}$ cluster should reveal the overall negative charge of (2–) to complete the neutral composition of the whole material, assuming that no other, i.e., besides TBA^+, counter-ions (e.g., OH^- or H_3O^+, which could have been difficult to detect by the accessible SC-XRD data) exist in the crystal structure. With this information, we attempted to analyze the crucial composition of the $\{Eu_2Ir_2\}$ cluster. It was found to be a difficult task due to the large structural disorder of the part of the clusters related to the nitrato ligands coordinated to Eu(III) centers. Most of their atoms had to be refined with two alternative positions with partial occupancies. Moreover, some of these nitrato ligands partially occupied the same position as the coordinated water molecule. In our initial attempts to describe this disordered part of the cluster, we found that presumably six nitrato ligands and one water molecule are present in the single $\{Eu_2Ir_2\}$ cluster; however, taking into account the large structural disorder, these findings demanded additional evidence. Thus, we analyzed the other parts of the cluster, which were found from the SC-XRD data easily and without doubt on their number and integrity. In each cluster, we found two Eu^{3+} ions, two Ir^{3+} ions, four cyanido (CN^-) ligands, and four *R*,*R*-pinppy ligands (each *R*,*R*-pinppy ligand reveals (1–) charge due to the deprotonation of a single C–H bond in the *R*,*R*-pinppyH precursor, which is a typical behavior for cyclometalated Ir(III) complexes, visible in the SC-XRD data, observed also in the precursor complex, and supported by the broad related literature, see ref. S1 and references therein; see the more detailed comment on this issue on Page S77 and the accompanying Fig. S42). Thus, the overall charge of non-nitrato molecular components (with the well-established charges) in the cluster can be calculated as follows: 2 x (3+) + 2 x (3+) + 4 x (1–) + 4 x (1–) = (4+). As mentioned above, two TBA^+ cations correspond to each $\{Eu_2Ir_2\}$ cluster. Thus, to fulfill the requirement of the neutrality of the whole material, six NO_3^- anions should be present in each cluster, which agrees with our findings from the initial analysis of the SC-XRD data. Following these considerations, we described the structural disorder of the nitrato ligands accordingly, finding six nitrato ligands and a single water molecule corresponding to each $\{Eu_2Ir_2\}$ cluster. In such a case, the combined charge of all cationic molecular components of the material is well balanced by the combined charge of all embedded anionic molecular components, leading to the neutral composition of the whole material. The precise analysis of the charges of all components of the molecular building unit of **Eu₂Ir₂** is presented in Fig. S39 and Table S30 (see below). This output leads to the presented composition of **Eu₂Ir₂** of $(TBA)_2\{[Eu^{III}(NO_3)_3(H_2O)_{0.5}]_2[Ir^{III}(CN)_2(R,R\text{-pinppy})_2]_2\}\cdot 2H_2O$ (note two non-coordinated water molecules were also found in the SC-XRD analysis, but they do not affect the charge balance). Therefore, the tetrametallic coordination cluster reveals the charge (2–) (Table S30) counter-balanced by two TBA^+ cations. The analogous composition was proposed for the isostructural **Eu₂FIr₂**, i.e., $(TBA)_2\{[Eu^{III}(NO_3)_3(H_2O)_{0.5}]_2[Ir^{III}(CN)_2(R,R\text{-Fpinppy})_2]_2\}\cdot nH_2O$ (the number of non-coordinated water molecules was not proposed due to the lack of the related SC-XRD data). Therefore, also for the second reported compound, the tetrametallic cluster was assumed to reveal the charge (2–) counter-balanced by two TBA^+ cations.

The additional evidence of the proposed number of intracluster nitrato ligands (i.e., six per the formula unit) is provided by the CHN elemental analyses, which were found to confirm the proposed composition, only with a different number of water molecules of crystallization. This is not surprising, as only part of the water molecules of crystallization could have been detected crystallographically for **Eu₂Ir₂** due to their large structural disorder. More importantly, the number of water molecules of crystallization is not crucial in confirming the presence of the proposed number of nitrato ligands per the formula unit, as they do not affect the key C-to-N ratio. This ratio is dependent on the number of other molecular components, including those containing N-atoms (cyanido, nitrato, and pinppy ligand, as well as TBA^+ cations) and those containing C-atoms (cyanido and pinppy ligands, as well as TBA^+ cations, but not nitrato ligands). The calculated C-to-N ratios for the proposed formula are expected to be identical for **Eu₂Ir₂** and **Eu₂FIr₂**, as both these compounds contain 108 C-atoms and 16 N-atoms for the formula unit. This leads to the calculated C/N ratio of 5.8, which agrees well with the experimental ones that were found to be 5.9(2) and 6.0(2) for **Eu₂Ir₂** and **Eu₂FIr₂**, respectively.

Our findings on the formulas of **Eu₂Ir₂** and **Eu₂FIr₂**, including the postulated composition and the overall (2–) charge of the incorporated tetrametallic cluster moiety, are supported by the comparison with the previously reported compounds.[S1,S29] In 2024, we reported the La^{III}-containing structural analog of **Eu₂Ir₂**, i.e., $(TBA)_2\{[La^{III}(NO_3)_3(H_2O)_{0.5}]_2[Ir^{III}(CN)_2(R,R\text{-pinppy})_2]_2\}$ (**La₂Ir₂**). They contain the analogous tetrametallic clusters based on two La^{3+} ions (instead of Eu^{3+}, presented in this work), two Ir^{3+} ions, four *R*,*R*-pinppy ligands, and four cyanido ligands, which were postulated to be completed with six nitrato ligands, leading to the overall (2–) charge, counter-balanced by two TBA^+ cations (Fig. S39 and Table S30). Thus, the analogous case as described above was found in our previous work, including also the significant structural disorder detected in the part of the molecular cluster related to coordinated nitrato anions. The considerations and conclusions were analogous to what is presented above. Moreover, in 2012, M. D. Ward et al. reported the structurally similar compound of $(PPN)_2\{[Eu^{III}(NO_3)_3(H_2O)_{0.5}]_2[Ir^{III}(CN)_2(ppy)]_2\}\cdot 5MeCN$ (PPN = bis (triphenylphosphine)iminium, ppy = a carbanion of 2-phenypyridine, Fig. S39). This compound was based on dicyanido Ir^{III} complexes with the non-chiral ppy ligands instead of *R*,*R*-pinppy ligands, which are presented here. The different counter-ion of PPN^+ was also used instead of TBA^+ ions, explored in this work. However, even with these changes, the mentioned compound reveals an analogous crystal structure to the reported materials. It also contains tetrametallic coordination clusters $\{Eu_2Ir_2\}$ built of two Eu^{3+} ions, two Ir^{3+} ions, four ppy ligands (each with the (1–) charge), four cyanido ligands, and six nitrato ligands. They altogether lead to the overall (2–) charge of the cluster, identical to those found in **Eu_2Ir_2** and **Eu_2FIr_2**, and the mentioned **La_2Ir_2** (Fig. S39, Table S30). This charge is counter-balanced by two organic counter-ions of PPN^+. The cluster's charge in the work of M. D. Ward et al. was more precisely identified due to the lack of structural disorder within the cluster and the lowered crystal symmetry (i.e., a $P\overline{1}$ space group of a triclinic crystal system versus a $P6_222$ space group of a hexagonal crystal system for **Eu_2Ir_2** in this work). As a result of both mentioned effects, there were no overlapping positions of nitrato ligands and coordinated water molecules, and the determination of the positions of all related atoms was very certain. The resulting number of these components per the formula unit, i.e., six nitrato ligands and one coordinated water molecule, is identical to those proposed for the compounds reported here. This additionally indicates the tendency of the investigated tetrametallic cyanido-bridged clusters to crystallize in the form of (2–) molecular anions, as was postulated and discussed above.

Comment on the air stability of *R*,*R*-Ir, *R*,*R*-FIr, Eu_2Ir_2, and Eu_2FIr_2: All the obtained materials change the solvent content upon exposure to air. However, this solvent change is slow and does not modify the respective P-XRD patterns (Fig. S6). Thus, the integrity of the structural features upon exposure to air can be postulated. However, to prevent eventual problems in the data interpretation, for all crucial optical measurements, the freshly prepared powder samples of the presented compounds were used, which eliminates the role of the variation in the solvent content as much as possible.

Structural studies

Single crystal X-ray diffraction (SC-XRD) analyses of *R*,*R*-FpinppyH, ***R*,*R*-FIr**, and **Eu_2Ir_2** were performed at 100(2) K, ensured by the CRYOStream 800 Plus system, using the Bruker D8 Quest Eco Photo50 CMOS diffractometer, equipped with a molybdenum X-ray lamp (Mo Kα 0.71073 Å), TRIUMPH monochromator, and CPAD Photon II detector. The single crystals of the respective compound were taken directly from the mother liquid, covered in Apiezon® N grease, and mounted on the Micro Mounts™ holder. The crystal structures were solved by an intrinsic phasing method using the SHELXT program within the Apex3 package.[S2] The crystal structures were refined within the WinGx software (ver. 2021.3) by the application of a weighted full-matrix least squares method on F^2.[S3] All non-hydrogen metals were refined anisotropically, while hydrogen atoms were calculated in their ideal positions and refined using the riding model. In a few special cases, hydrogen atoms were found directly from the electron density map. A reasonable number of DFIX, ISOR, and DELU restraints were applied for some of the most disordered atoms to ensure proper geometry and convergence of the refinement process. This was necessary as, especially in the case of **Eu_2Ir_2**, a large structural disorder was detected. By applying all of these procedures, satisfactory refinement parameters for all reported crystal structures were obtained. For **Eu_2Ir_2**, two structural A-type alerts remained, which were thoroughly explained in the CIF file along with the B-type alerts that are present both in **Eu_2Ir_2** as well as ***R*,*R*-FIr** (see respective CIF files for details). In addition, due to the non-negligible structural disorder, larger in **Eu_2Ir_2** and smaller in ***R*,*R*-FIr**, the respective Flack *x*-parameters deviate from the ideal value of zero. They are, however, at the very low levels of 0.066(6) and 0.025(3) for **Eu_2Ir_2** and ***R*,*R*-FIr**, respectively, as expected for the enantiopure compounds. The SC-XRD data of all investigated compounds, *R*,*R*-FpinppyH, ***R*,*R*-FIr**, and **Eu_2Ir_2**, were deposited in the CCDC database with numbers 2420768, 2420770, and 2420769, respectively. The details of the refinement process and crystal data are summarized in Table S1, while the detailed structure parameters were gathered in Tables S2 and S3. Fig. 1 and S3–S5 visualize the crystal structures of the obtained compounds. They were prepared using Mercury 2022.3 software. Powder X-ray diffraction (P-XRD) experiments were performed on a Bruker D8 Advance ECO diffractometer equipped with a Cu Kα lamp (X-ray wavelength of 1.5419 Å) and an SSD160 detector. Polycrystalline samples of all compounds were ground, inserted into a 0.5 mm glass capillary, and mounted into the diffractometer. All the measurements were performed at room temperature in the transmission mode with an appropriate setup for rotating capillaries.

Physical techniques

^1H and $^{13}C\{^1H\}$ NMR spectra were recorded for solutions in $CDCl_3$ containing TMS (Me_4Si) as an internal standard, at room temperature, by using a Jeol 400 MHz ECZR spectrometer. CHN elemental analyses were performed with standard microanalysis procedures using the Elementar Vario Micro Cube CHN analyzer. The infrared (IR) absorption spectra were collected on a Nicolet iN10 MX FT-IR microscope in transmission mode. Measurements were made in the range of 3800–670 cm^{-1} for selected single crystals on a BaF_2 window. Thermogravimetric (TG) measurements were performed on a NETZSCH TG 209 F1 Libra apparatus under inert gas (N_2) at a heating rate of 1 $°C\cdot min^{-1}$ in the temperature range of 20–400 °C. The ESI-TOF mass spectra (MS) were gathered for the acetonitrile solutions of the investigated compounds using a microTOF-II mass spectrometer of Bruker Daltonics.

The second harmonic generation (SHG) activity was checked using a homemade optical setup equipped with a 1040 nm femtosecond laser as an excitation light source.[S4] To verify the SHG origin of the output light, its power and wavelength dependencies were measured. To quantify the SH intensities, a potassium dihydrogen phosphate (KDP) was used as a reference sample under identical experimental conditions.

Solid-state UV-vis absorption spectra were measured in the range of 220−750 nm on a Shimadzu UV-3600i plus spectrometer using the thin films of the powder samples of respective compounds inserted between quartz plates. Solid-state photoluminescent properties were measured using an FS5 spectrofluorometer equipped with an Xe (150 W) arc lamp as an excitation source and a Hamamatsu photomultiplier of the R928P type as a detector. Emission lifetime measurements were conducted on the FS5 spectrofluorometer using a time-correlated single photon counting method with an EPLED-380 picosecond pulsed light-emitting diode (wavelength of 374.4 nm). Absolute photoluminescence quantum yields (PL-QYs) were determined using a direct excitation method with an integrating sphere module for the FS5 spectrofluorometer.[S5] The temperature-variable emission and excitation spectra were collected on the same spectrofluorometer using a CS204SI-FMX-1SS cooling power optical helium cryostat equipped with a DE-204SI closed cycle cryo-cooler (cold head), water-cooled He compressor (ARS-4HW model), and the model 335 cryogenic temperature controller. Luminescent background corrections were performed within the Fluoracle software provided by Edinburgh Instruments.

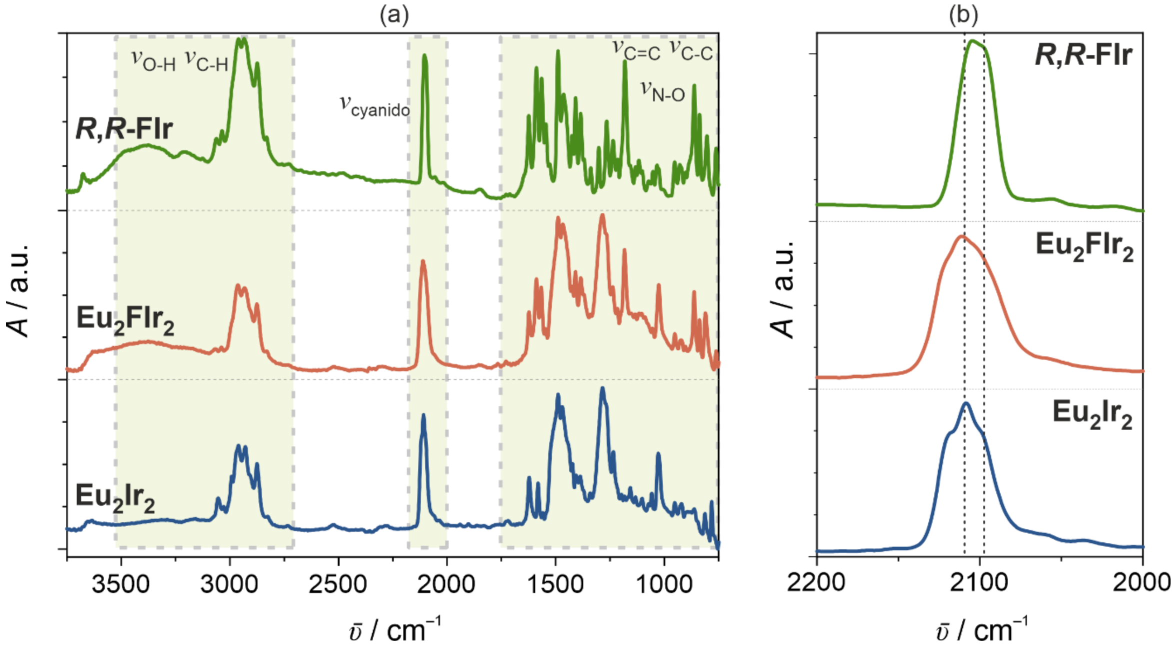

Fig. S1 Infrared (IR) absorption spectra for the crystalline samples of ***R*,*R*-FIr**, **Eu$_2$FIr$_2$**, and **Eu$_2$Ir$_2$**, presented in the broad range of 3750–750 cm^{-1} (a) and the limited range of 2200-2000 cm^{-1} that corresponds to the stretching vibrations of cyanido ligands (b). The vertical dotted lines in (b) visualize the shift of the maxima going from ***R*,*R*-FIr** to **Eu$_2$FIr$_2$** and **Eu$_2$Ir$_2$**.

Comment to Fig. S1: Absorption of IR light in the range of 3150–2600 cm^{-1} is related to stretching vibrations ν(C–H) of the aromatic and aliphatic parts of organic ligands, cations, and solvent molecules. The IR spectra in the 1700–670 cm^{-1} range are composed of many characteristic absorption peaks connected with skeletal vibrations such as ν(C–C), ν(N=O), and ν(N–O). In part (b), the peaks corresponding to the characteristic stretching vibrations of cyanido ligands are presented. There is a shift of these absorption going from ***R*,*R*-FIr** to **Eu$_2$FIr$_2$** and **Eu$_2$Ir$_2$** which agrees well with the structural data as the ***R*,*R*-FIr** compound contains only the terminal cyanido ligands whose stretching vibrations are of lower energy while **Eu$_2$FIr$_2$** and **Eu$_2$Ir$_2$** contain only the bridging cyanido ligands whose stretching vibrations are expected to be of higher energy. This is a typical trend observed for cyanido stretching vibrations in the family of polycyanidometallate-based coordination compounds.[S1,S6]

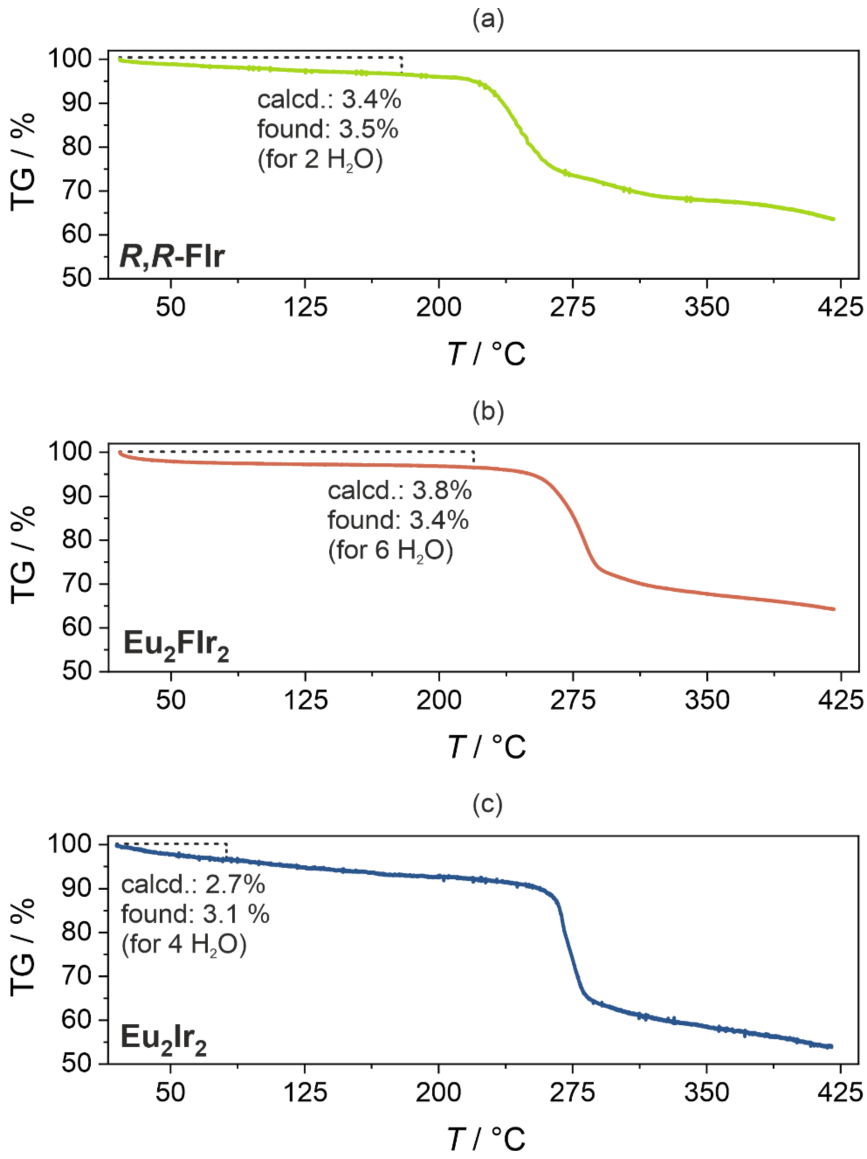

Fig. S2 Thermogravimetric (TG) curves for crystalline samples of ***R*,*R*-FIr**, **Eu_2FIr_2**, and **Eu_2Ir_2** (a–c, respectively), collected in the range of 20–420 °C. On each curve, the calculated and experimental steps related to the removal of solvent molecules of crystallization are depicted.

Comment to Fig. S2: The data gathered in the figure above were measured for polycrystalline samples, which were filtered and left in air for a few hours. As indicated by the CHN analyses, all investigated compounds contain water molecules of crystallization. The TG analyses confirm the presence of solvent molecules. The related steps in the thermogravimetric curves can be observed, and they are depicted on the graphs. In all cases, there is a gradual, relatively small decrease in the sample weight (TG) upon heating as only the weakly solvent molecules of crystallization (water) are removed. For ***R*,*R*-FIr** and **Eu_2FIr_2**, the observed mass change within the broad, gradual heating-induced step corresponds well to the values expected for the water content indicated by the CHN analyses (see Experimental details). For **Eu_2Ir_2**, this gradual heating-induced step is deeper, so it can be interpreted by means of the further removal of other molecular components, e.g., coordinated water molecules and/or organic counter-ions. In all cases, at higher temperatures, above 250–275 °C, a much larger decrease in the sample mass is observed, which is related to the decomposition of the respective crystal structures.

Table S1 Crystal data and structure refinement parameters for *R,R*-FpinppyH, ***R,R*-FIr**, and **Eu_2Ir_2**, compared with the analogous data for previously reported TBA[$Ir^{III}(CN)_2$(*R,R*-pinppy)$_2$]·2MeCN (***R,R*-Ir**).[S1]

Compound	*R,R*-FpinppyH	***R,R*-FIr**	**Eu_2Ir_2**	***R,R*-Ir** [ref. S1]
Formula	$C_{18}H_{18}FN$	$C_{58}H_{76}F_2IrN_7$	$C_{108}H_{150}Eu_2Ir_2N_{16}O_{21}$	$C_{58}H_{78}IrN_7$
Formula weight / g·mol^{-1}	267.33	1101.45	2696.75	1065.47
***T* / K**	100(2)			
***λ* / Å**	0.71073 (Mo Kα)			
Crystal system	orthorhombic	orthorhombic	hexagonal	orthorhombic
Space group	$P\,2_12_12_1$	$P\,2_12_12_1$	$P\,6_222$	$P\,2_12_12_1$
***a* / Å**	5.7780(3)	13.8335(7)	17.3485(8)	13.624(3)
***b* / Å**	12.3807(8)	14.0896(6)	17.3485(8)	14.206(2)
***c* / Å**	19.4561(12)	27.5937(13)	37.291(3)	27.254(5)
***α* / °**	90	90	90	90
***β* / °**	90	90	90	90
***γ* / °**	90	90	120	90
***V* / Å^3**	1391.81(14)	5378.2(4)	9719.8(11)	5275.0(16)
Z	4	4	3	4
Density / g·cm^{-1}	1.276	1.360	1.382	1.342
Crystal shape	block	block	block	block
Crystal size / mm x mm x mm	0.900 x 0.600 x 0.450	0.470 x 0.170 x 0.120	0.360 x 0.290 x 0.250	0.150 x 0.140 x 0.130
Absorption coefficient / cm^{-1}	0.083	2.533	3.066	2.575
***F*(000)**	568	2272	4074	2208
***Θ* range / °**	2.663–25.015	2.537–25.025	2.348–25.034	2.554–35.027
Limiting indices	$-6 < h < 6$ $-14 < k < 14$ $-23 < l < 23$	$-16 < h < 16$ $-16 < k < 16$ $-32 < l < 32$	$-20 < h < 18$ $-14 < k < 20$ $-44 < l < 43$	$-16 < h < 16$ $-16 < k < 16$ $-32 < l < 32$
Collected reflections	20763	149958	58162	61588
Unique reflections	2442	9483	5741	9286
R_{int}	0.0215	0.0400	0.0553	0.0455
Completeness / %	99.1	99.9	99.7	99.7
Flack *x*-parameter	−0.06(16)	0.025(3)	0.066(6)	0.015(3)
Data/restraints/parameters	2442/0/181	9483/32/631	5741/142/382	9286/0/597
GOF on F^2	1.061	1.121	1.262	1.088
Final *R* indices (R_1 for [$I > 2\sigma(I)$], wR_2 for all data)	$R_1 = 0.029$ $wR_2 = 0.077$	$R_1 = 0.0264$ $wR_2 = 0.0626$	$R_1 = 0.0723$ $wR_2 = 0.1786$	$R_1 = 0.0244$ $wR_2 = 0.0524$
Largest diff. peak and hole / e·Å^{-3}	0.161 −0.140	0.959 −0.787	1.001 −2.560	0.907 −1.087

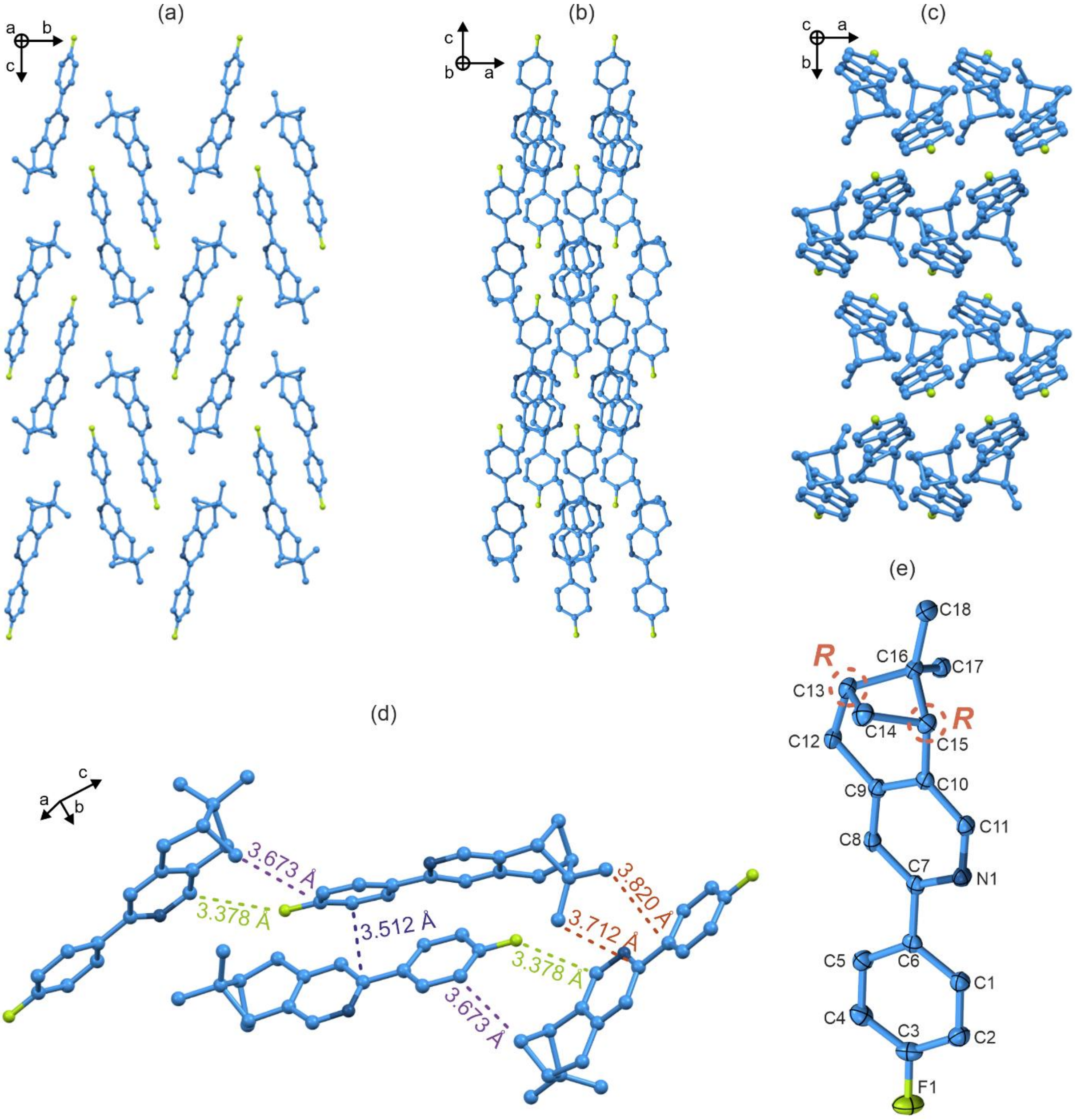

Fig. S3 The representative views of the crystal structure of *R*,*R*-FpinppyH, including its presentation along main crystallographic axes (a, b, and c), the detailed insight into the intermolecular interaction with the depicted closest intermolecular distances (d), and the asymmetric unit of the structure with thermal ellipsoids of atoms shown at the 50% probability level (the atoms labeling scheme is additionally presented; hydrogen atoms were omitted for clarity) (e). The chirality of the ligand is depicted in the (e) part.

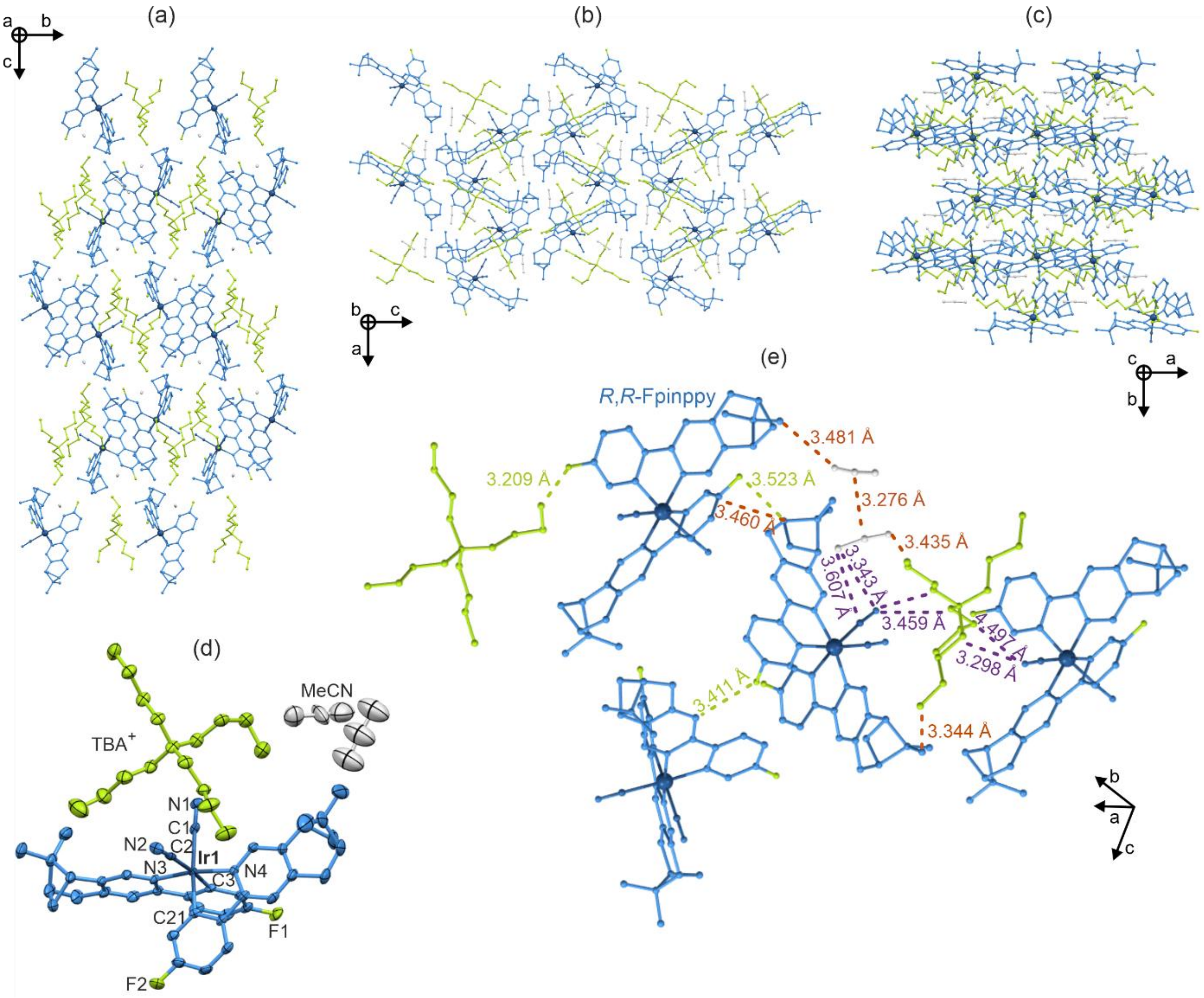

Fig. S4 Representative views of the crystal structure of ***R,R*-FIr**, including its presentation along main crystallographic axes (a, b, and c), the detailed insight into the asymmetric unit with the atoms presented with their thermal ellipsoids (50% probability level) and labeling scheme (d), and the view on the intermolecular contacts between cationic and anionic molecular building blocks (e). Hydrogen atoms were omitted everywhere for clarity.

Table S2 Selected detailed structure parameters of ***R*,*R*-FIr**.

Selected bond distances in *cis*–[Ir1(CN)$_2$(*R*,*R*-Fpinppy)$_2$]$^-$ complexes / Å					
Ir1–C1	2.052(6)	**Ir1–C3**	2.047(5)	**Ir1–N3**	2.059(5)
Ir1–C2	2.057(6)	**Ir1–C21**	2.048(6)	**Ir1–N4**	2.051(5)
Selected angles in *cis*–[Ir1(CN)$_2$(*R*,*R*-Fpinppy)$_2$]$^-$ complexes / °					
C1–Ir1–C2	87.9(2)	**C2–Ir1–C3**	173.7(2)	**C3–Ir1–N3**	80.0(2)
C1–Ir1–C3	93.1(2)	**C2–Ir1–C21**	90.5(2)	**C3–Ir1–N4**	90.8(2)
C1–Ir1–C21	173.5(3)	**C2–Ir1–N3**	93.8(2)	**C21–Ir1–N3**	94.8(2)
C1–Ir1–N3	91.6(2)	**C2–Ir1–N4**	95.3(2)	**C21–Ir1–N4**	79.8(2)
C1–Ir1–N4	94.1(2)	**C3–Ir1–C21**	89.1(2)	**N3–Ir1–N4**	169.4(2)

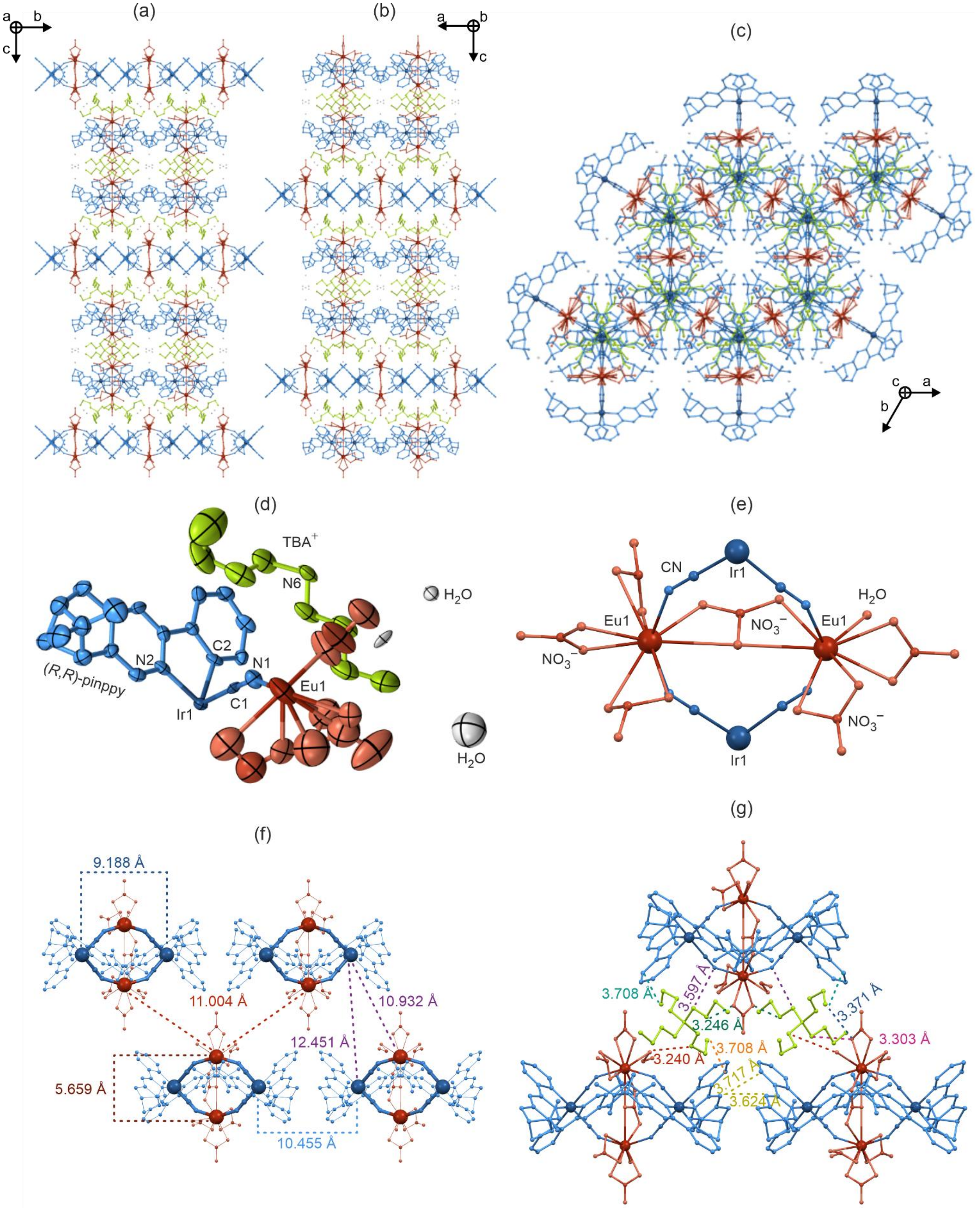

Fig. S5 Representative views of the crystal structure of **Eu_2Ir_2**, including its presentation along main crystallographic axes (a, b, and c), the detailed view of the asymmetric unit with the atoms presented by thermal ellipsoids at the 40% probability level (d), the visualization of the arrangement of bridging nitrato and cyanido ligands within the molecular anions (e), the visualization of the intercluster interactions within the structure (f), and the analogous view of the intermolecular interactions between the cationic and anionic components embedded in the structure (g). Hydrogen atoms were omitted everywhere for clarity.

Table S3 Selected detailed structure parameters of **Eu$_2$Ir$_2$**.

<table>
<tr><th colspan="6">Selected bond distances and angles in <i>cis</i>–[Ir1(μ–CN)$_2$(<i>R</i>,<i>R</i>-pinppy)$_2$]$^-$ complexes / Å, °</th></tr>
<tr><td>Ir1–C1</td><td>2.050(17)</td><td>Ir1–C2</td><td>2.062(14))</td><td>Ir1–N2</td><td>2.045(15)</td></tr>
<tr><td>C1–Ir1–C1</td><td>87.3(9)</td><td>C1–Ir1–N2</td><td>95.6(6) / 88.9(6)</td><td>C2–Ir1–N2</td><td>80.7(6) / 94.7(7)</td></tr>
<tr><td>C1–Ir1–C2</td><td>92.2(6) / 176.3(8)</td><td>C2–Ir1–C2</td><td>88.5(8)</td><td>N2–Ir1–N2</td><td>173.7(7)</td></tr>
<tr><th colspan="6">Selected bond distances and angles in [Eu1(μ–NC)$_2$(κ^2–NO$_3$)$_3$(μ,κ^2–NO$_3$)]$^{3-}$ and [Eu1(μ–NC)$_2$(κ^2–NO$_3$)$_2$(μ,κ^2–NO$_3$)(H$_2$O)]$^{2-}$ complexes / Å °</th></tr>
<tr><td>Eu1–N1</td><td>2.411(15)</td><td>N1–Eu1–O7</td><td>78.6(9) / 81.7(10)</td><td>O3–Eu1–O8</td><td>73.10</td></tr>
<tr><td>Eu1–O1</td><td>2.43(2)</td><td>N1–Eu1–O8</td><td>75.11</td><td>O4–Eu1–O4</td><td>126.0(5)</td></tr>
<tr><td>Eu1–O3</td><td>2.62(3)</td><td>O1–Eu1–O1</td><td>53.7(11)</td><td>O4–Eu1–O5</td><td>50.32(8) / 120.4(3)</td></tr>
<tr><td>Eu1–O4</td><td>2.627(6)</td><td>O1–Eu1–O3</td><td>94.6(17) / 116.0(12)</td><td>O4–Eu1–O7</td><td>73.0(10) / 153.4(8)</td></tr>
<tr><td>Eu1–O5</td><td>2.687(6)</td><td>O1–Eu1–O4</td><td>66.1(10) / 66.1(9)</td><td>O4–Eu1–O8</td><td>117.01</td></tr>
<tr><td>Eu1–O7</td><td>2.42(4)</td><td>O1–Eu1–O5</td><td>62.0(9) / 102.1(9)</td><td>O5–Eu1–O5</td><td>163.25</td></tr>
<tr><td>Eu1–O8</td><td>2.830</td><td>O1–Eu1–O7</td><td>138.3(13) / 115.8(14)</td><td>O5–Eu1–O7</td><td>53.8(11) / 141.5(11)</td></tr>
<tr><td>N1–Eu1–N1</td><td>150.2(7)</td><td>O1–Eu1–O8</td><td>153.28</td><td>O5–Eu1–O8</td><td>98.37</td></tr>
<tr><td>N1–Eu1–O1</td><td>80.5(6)/ 128.6(6)</td><td>O3–Eu1–O3</td><td>146.2(17)</td><td>O7–Eu1–O7</td><td>97(2)</td></tr>
<tr><td>N1–Eu1–O3</td><td>86.3(16) / 85.1(19)</td><td>O3–Eu1–O4</td><td>49.9(6) / 155.1(18)</td><td>O7–Eu1–O8</td><td>48.62</td></tr>
<tr><td>N1–Eu1–O4</td><td>76.6(14)/ 114.8(13)</td><td>O3–Eu1–O5</td><td>35.3(17) / 154.2(19)</td><td>C1–N1–Eu1</td><td>148.9(14)</td></tr>
<tr><td>N1–Eu1–O5</td><td>75.6(5) / 118.9(5)</td><td>O3–Eu1–O7</td><td>24.7(12) / 121.6(15)</td><td>-</td><td>-</td></tr>
</table>

<table>
<tr><th colspan="2">Selected distances and angles between metal centers within the {Eu$^{III}{}_2$Ir$^{III}{}_2$} clusters / Å °</th><th colspan="2">Selected distances between metal centers within the {Eu$^{III}{}_2$Ir$^{III}{}_2$} clusters / Å</th></tr>
<tr><td>Eu1–Eu1</td><td>5.659</td><td>Eu1–Eu1
(in [021] and [02-1])</td><td>11.004</td></tr>
<tr><td>Eu1–Ir1</td><td>5.396</td><td>Eu1–Eu1
(in [100] and [010])</td><td>17.349</td></tr>
<tr><td>Ir1–Ir1</td><td>9.188</td><td>Ir1–Ir1 (in [001])</td><td>12.451</td></tr>
<tr><td>Eu1–Ir1–Eu1</td><td>63.26</td><td>-</td><td>-</td></tr>
<tr><td>Ir1–Eu1–Ir1</td><td>116.74</td><td>-</td><td>-</td></tr>
</table>

Table S4 Results of Continuous Shape Measure (CShM) analysis for six-coordinated Ir(III) complexes in ***R*****,*****R*****-FIr** and **Eu$_2$Ir$_2$**.

Compound	CShM parameter*					Geometry
	HP-6	PPY-6	OC-6	TPR-6	JPPY-6	
R**,*****R*****-FIr**	30.400	26.347	**0.570**	14.050	30.239	**OC-6**
Eu$_2$Ir$_2$	28.566	27.725	**0.454**	15.783	31.146	**OC-6**

Comment on Table S4: Continuous Shape Measure (CShM) analysis for the Ir(III) and Eu(III) complexes was performed using SHAPE software ver. 2.1.21.[S7] The Continuous Shape Measure (CShM) parameter represents the distortion from ideal geometry. It equals 0 for an ideal polyhedron and increases with increasing distortion. Due to the significant disorder in the crystal structure of **Eu$_2$Ir$_2$** (see Experimental section above), some DFIX restraints were applied for the Eu−O bond distances to ensure its proper geometry and the convergence of the refinement procedure. Therefore, the CShM analysis is strongly affected providing a large error. Thus, the results for the Eu(III) complexes are not presented (9- and 10-coordinated complexes were considered). However, for the record, the geometries for the nine-coordinated Eu(III) complexes in **Eu$_2$Ir$_2$** were found the best described by the strongly distorted MFF-9 (muffin, C_s), while the ten-coordinated complexes are best characterized by the geometry of strongly deformed JSPC-10 (sphenocorona, C_{2v}). On the other hand, the Ir(III) complexes in both ***R*****,*****R*****-FIr** and **Eu$_2$Ir$_2$** are well described by an octahedral geometry.

*Continuous Shape Measure (CShM) Parameters:[S8]

six-coordinated complexes

CShM HP-6 – the parameter related to the hexagon (D_{6h} symmetry)

CShM PPY-6 – the parameter related to the pentagonal pyramid (C_{5v})

CShM OC-6 – the parameter related to the octahedron (O_h)

CShM TPR-6 – the parameter related to the trigonal prism (D_{3h})

CShM JPPY-6 – the parameter related to the Johnson pentagonal pyramid (C_{5v})

nine-coordinated complexes[S9]

CShM MFF-9 – the parameter related to the Muffin (C_s)

ten-coordinated complexes[S10]

CShM JSPC-10 the parameter related to the sphenocorona (C_{2v})

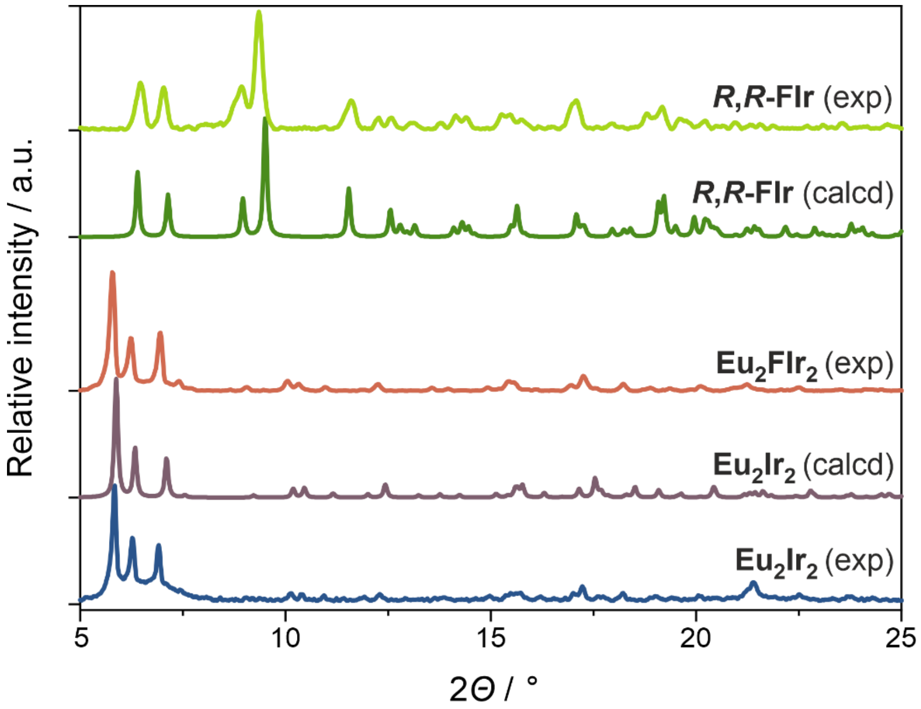

Fig. S6 Comparison of experimental (exp) and theoretical (calcd, i.e., calculated based on the structural model obtained within the SC-XRD structural analysis) powder XRD diffractograms for reported compounds, presented in the range of 5–30° of the 2*Θ* angle.

Comment on Fig. S6: The crystals of compound **Eu_2FIr_2** were not suitable for the reliable SC-XRD analysis. However, the P-XRD analysis of the obtained polycrystalline sample of this material reveals that it is isostructural with the **Eu_2Ir_2** compound for which both the SC-XRD as well as the P-XRD analyses were successfully performed.

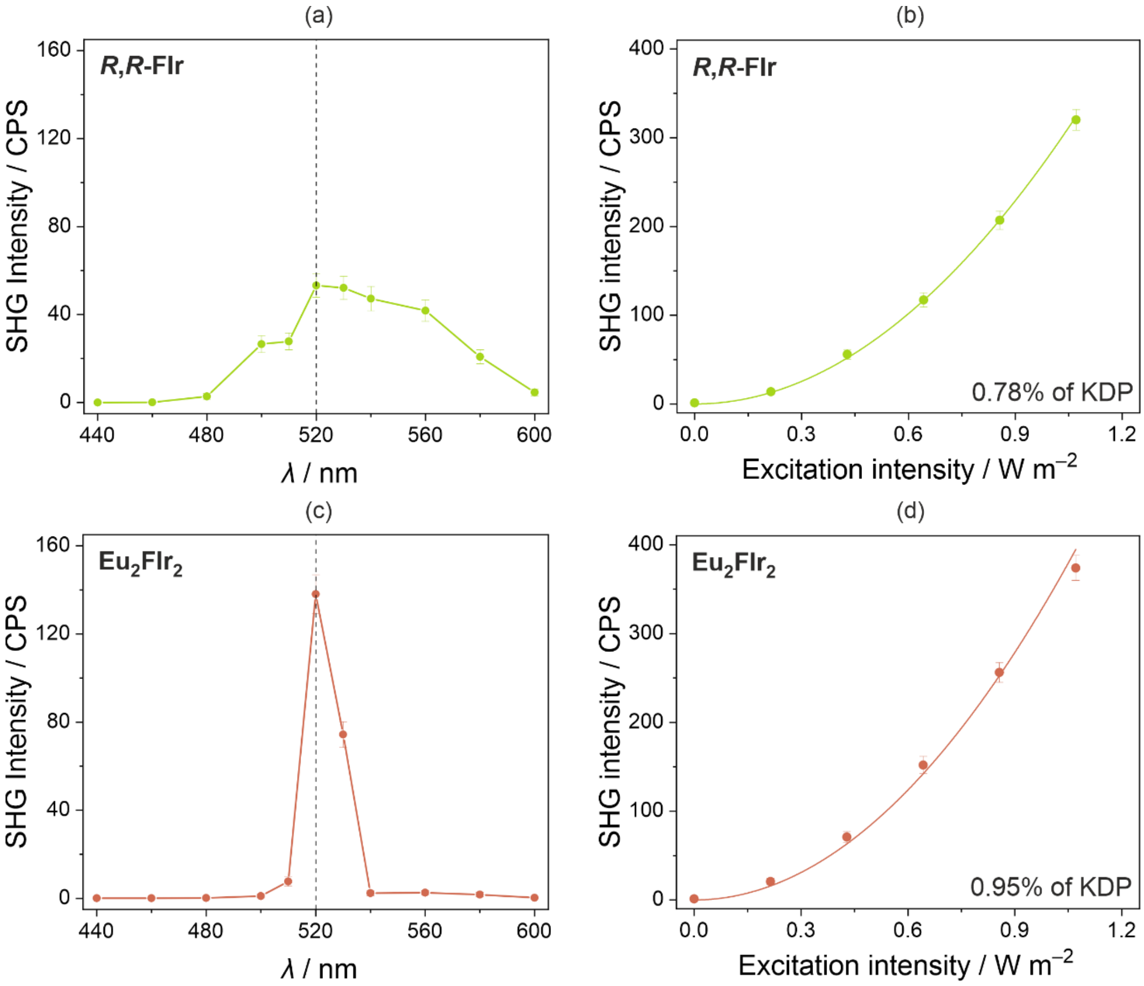

Fig. S7 Detailed SHG characteristics for ***R,R*-FIr** and **Eu$_2$FIr$_2$** for the irradiation by the 1040 nm laser, including the wavelength dependences for the SHG output light (a and c for ***R,R*-FIr** and **Eu$_2$FIr$_2$**, respectively) and the respective power dependences for the SHG light at 520 nm (b and d). In the (b) and (d) parts, the strength of the SHG light for the depicted compound compared with that for the KDP (potassium dihydrogen phosphate) reference material is presented. Note that the wavelength dependences were gathered for the maximal accessible excitation intensity, but the observed SHG intensity was found to be weaker than for the preceded measurement of the power dependences due to the gradual degradation of the samples under the prolonged strong laser irradiation. For such a reason, the analogous data could not be reliably measured for **Eu$_2$Ir$_2$**, which was found to be much more sensitive to laser irradiation.

Table S5 Comparison of the SHG intensities for the reported compounds and the previously published reference materials.[S1]

Compound	Formula	Space group	SHG intensity as a percentage of the signal for KDP
***R*,*R*-FIr** /this work/	TBA[Ir^{III}(CN)$_2$(*R*,*R*-Fpinppy)$_2$]·2H$_2$O	$P\ 2_12_12_1$	0.78%
***R*,*R*-Ir**[S1]	TBA[Ir^{III}(CN)$_2$(*R*,*R*-pinppy)$_2$]·2H$_2$O	$P\ 2_12_12_1$	0.17%
Eu$_2$FIr$_2$ /this work/	(TBA)$_2${[Eu^{III}(NO$_3$)$_3$(H$_2$O)$_{0.5}$]$_2$[Ir^{III}(CN)$_2$(*R*,*R*-Fpinppy)$_2$]$_2$}·6H$_2$O	$P\ 6_222$	0.96%
Eu$_2$Ir$_2$ /this work/	(TBA)$_2${[Eu^{III}(NO$_3$)$_3$(H$_2$O)$_{0.5}$]$_2$[Ir^{III}(CN)$_2$(*R*,*R*-pinppy)$_2$]$_2$}·4H$_2$O	$P\ 6_222$	~0% /not stable under the laser irradiation/
La$_2$Ir$_2$[S1]	(TBA)$_2${[La^{III}(NO$_3$)$_3$(H$_2$O)$_{0.5}$]$_2$[Ir^{III}(CN)$_2$(*R*,*R*-pinppy)$_2$]$_2$}·4.5H$_2$O	$P\ 6_222$	0.045 %

Comment on Table S5: According to the Kleinman symmetry rule,[S11,S12] the *422*, *432*, and *622* point groups should not exhibit second harmonic generation. However, according to the literature,[S13–S15] this principle was shown to be often violated in non-ideal media, i.e., dispersive ones, such as in the powder samples of molecular materials. This explains why the non-zero SHG values can be obtained in the **Eu$_2$FIr$_2$** material, and were observed in the analogous La(III)-containing compound, **La$_2$Ir$_2$**.[S1]

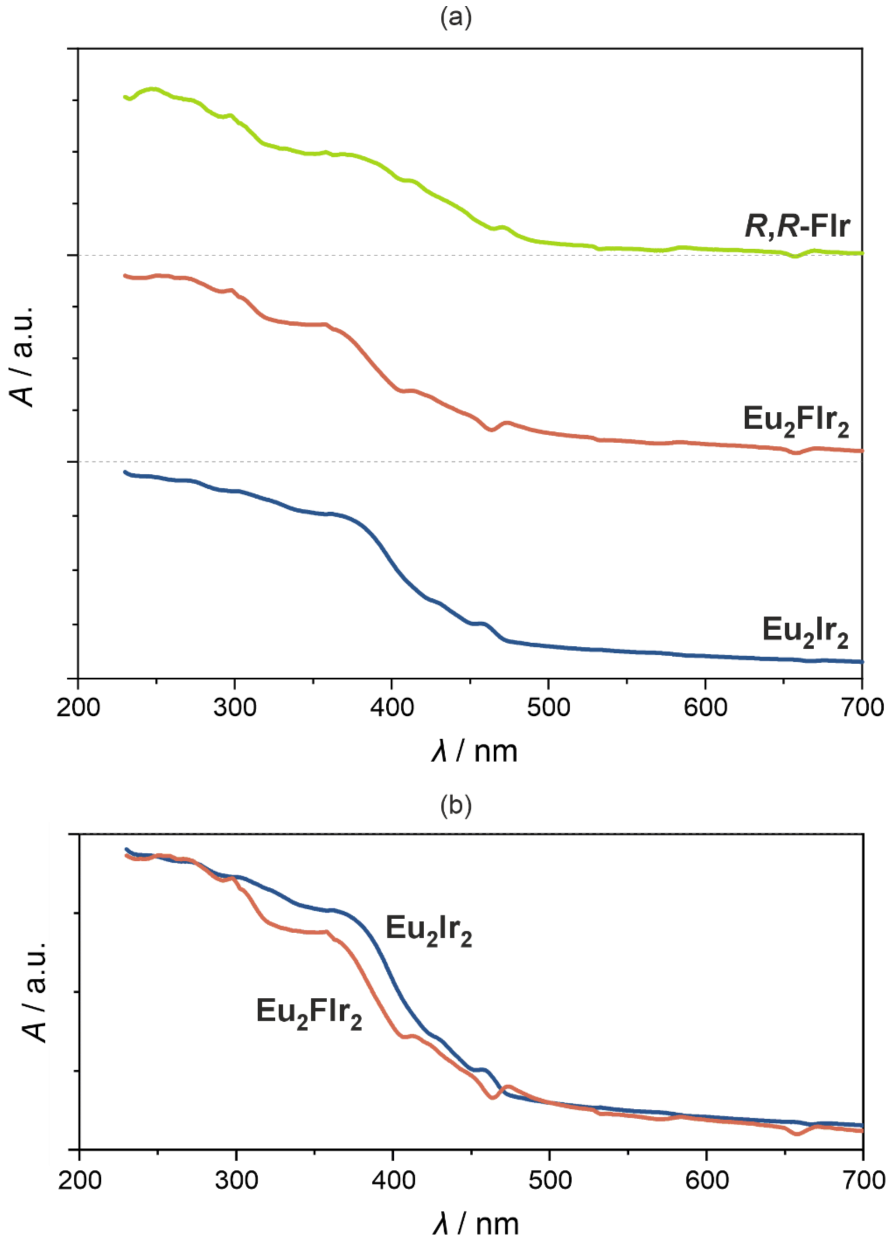

Fig. S8 Solid-state UV-Vis absorption spectra of reported compounds, recorded at room temperature (300K) in the 230–700 nm wavelength range (a), and the additional presentation of the overlapped normalized spectra for two heterometallic compounds, illustrating the blueshift of the absorption bands occurring when going from **Eu_2Ir_2** to its fluorinated analogue of **Eu_2FIr_2** (b, see the main text for details).

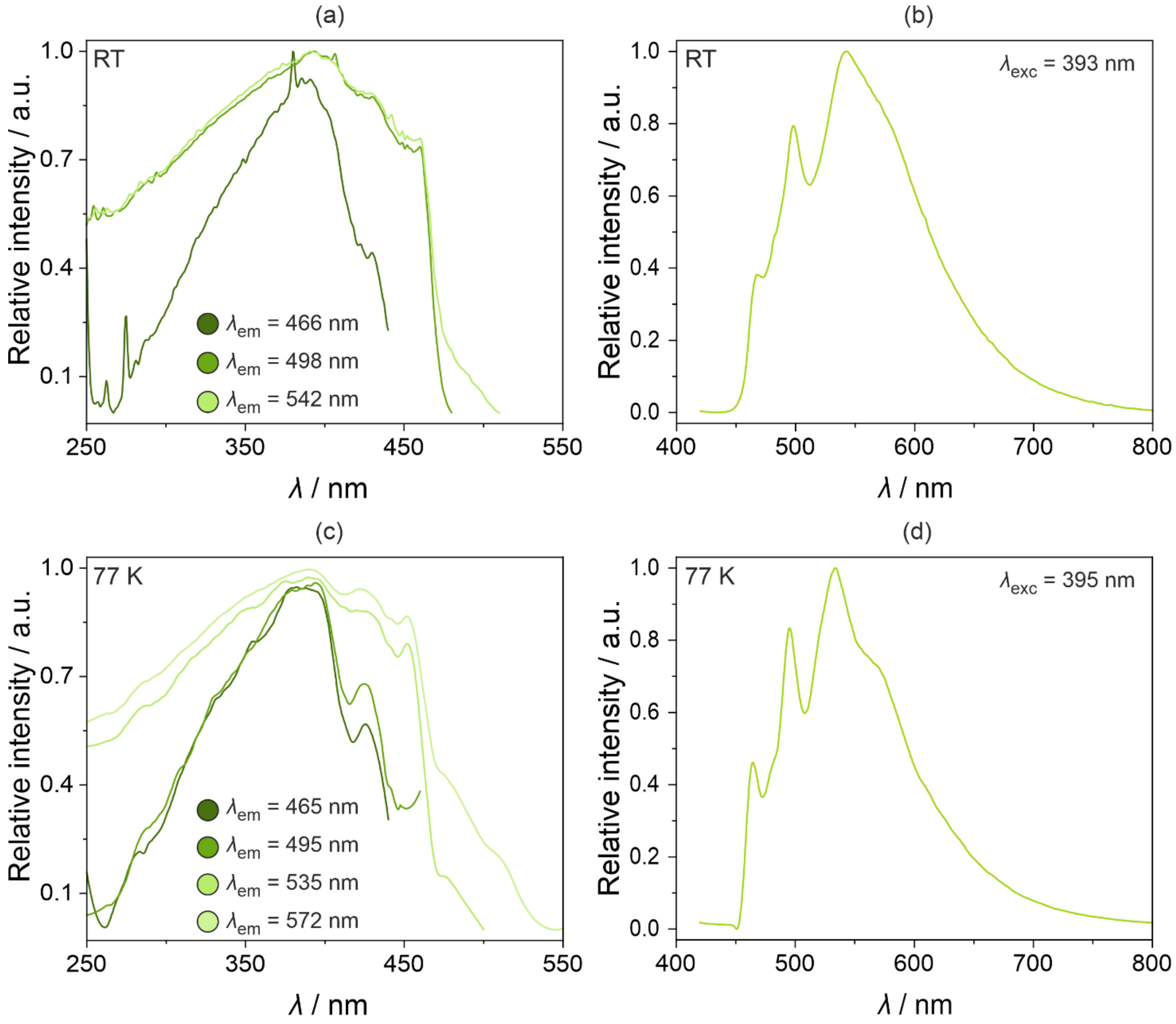

Fig. S9 Representative solid-state photoluminescent characteristics of ***R*,*R*-FIr**, including room-temperature (RT) excitation spectra for the indicated emission maxima (a), the room-temperature emission spectrum for the optimal indicated excitation (b), low-temperature (77 K) excitation spectra for the indicated emission maxima (c), and the low-temperature (77 K) emission spectrum for the optimal indicated excitation (d).

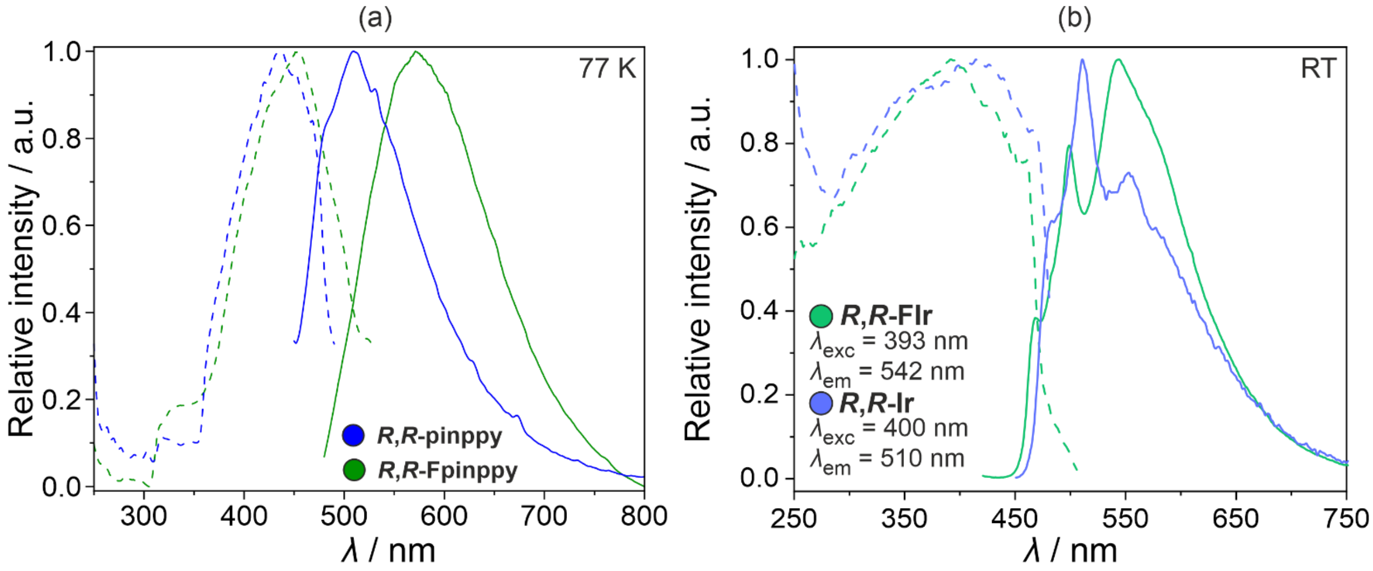

Fig. S10 Comparison of solid-state photoluminescence properties of used organic ligands of *R*,*R*-FpinppyH and *R*,*R*-pinppyH[S1] (a, measured in their free forms, without metal ions), as well as the analogous properties of ***R*,*R*-FIr** and ***R*,*R*-Ir**[S1] (b). Each comparison contains the excitation spectra for the monitored emission maximum and the respective emission spectra for the optimal excitation. As the bands are much more complex for ***R*,*R*-FIr** and ***R*,*R*-Ir**, the detailed wavelength values used are depicted on the graph for their cases. The spectra for the ligands were gathered at a decreased temperature (77 K) as they are not luminescent at room temperature.

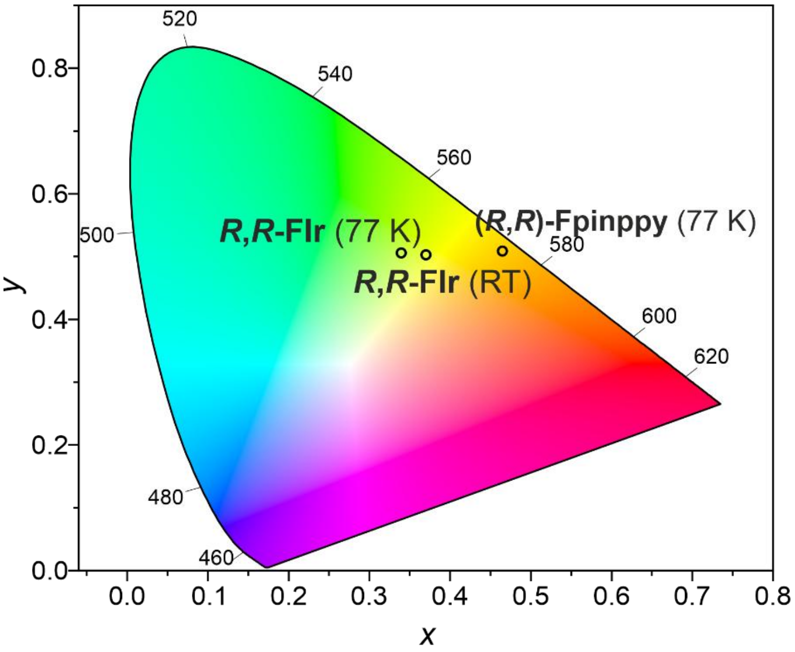

Fig. S11 The emission color of ***R,R*-FpinppyH** (77 K) and ***R,R*-FIr** (77 K and RT) presented on the CIE 1931 chromaticity diagram. Corresponding *x* and *y* parameters were gathered in Table S6.

Table S6 The CIE 1931 chromaticity parameters for the solid-state emission of *R*,*R*-FpinppyH and ***R*,*R*-FIr**.

Compound	Temperature	CIE 1931 chromaticity parameters	
		x	*y*
R,*R*-FpinppyH	77 K	0.465	0.509
***R*,*R*-FIr**	RT	0.340	0.506
***R*,*R*-FIr**	77 K	0.370	0.503

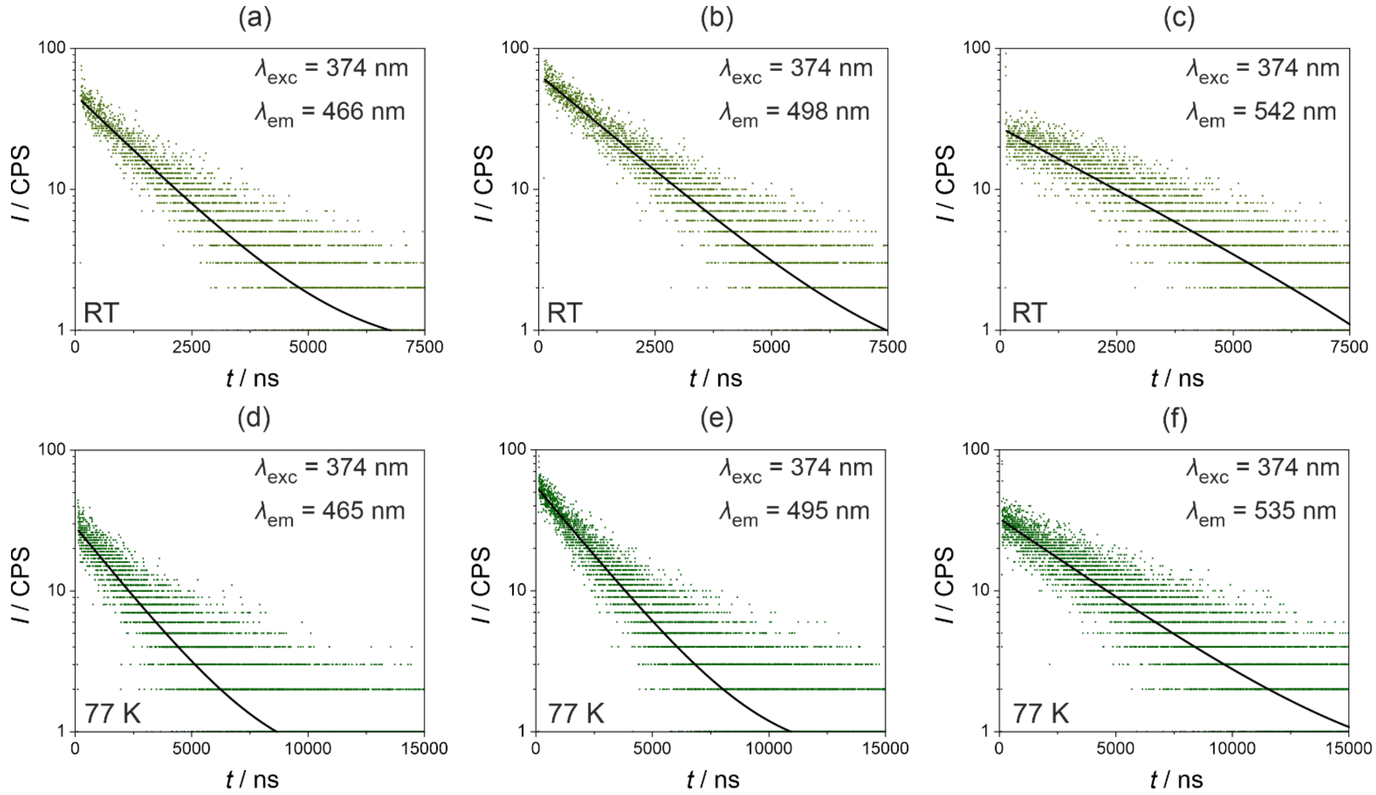

Fig. S12 The set of emission lifetimes gathered for ***R*,*R*-FIr** at room temperature under three different emission maxima (a–c) and low temperature (77 K) under three different emission maxima (d–f). In both cases, the selected emission wavelengths correspond to the distinct maxima detectable on the respective emission pattern (see Fig. S9). The dots represent data gathered to which the exponential decay functions were fitted (solid black lines). The resulting best-fit parameters are presented in Table S7.

Table S7 Best-fit parameters for the emission decay profiles for ***R*,*R*-FIr** to the mono-exponential decay function for data gathered for different emission bands at room temperature and 77 K under the 374 nm picosecond laser diode irradiation.

	RT			77 K	
Emission wavelength /nm	**τ(±τ) / µs**	**X^2**	**Emission wavelength /nm**	**τ (±τ) / µs**	**X^2**
466	1.353(±0.018)	1.0006	465	2.117(±0.032)	1.0387
498	1.567(±0.016)	1.0053	495	2.174(±0.018)	1.0123
542	2.491(±0.041)	1.0077	535	3.812(±0.038)	1.0440

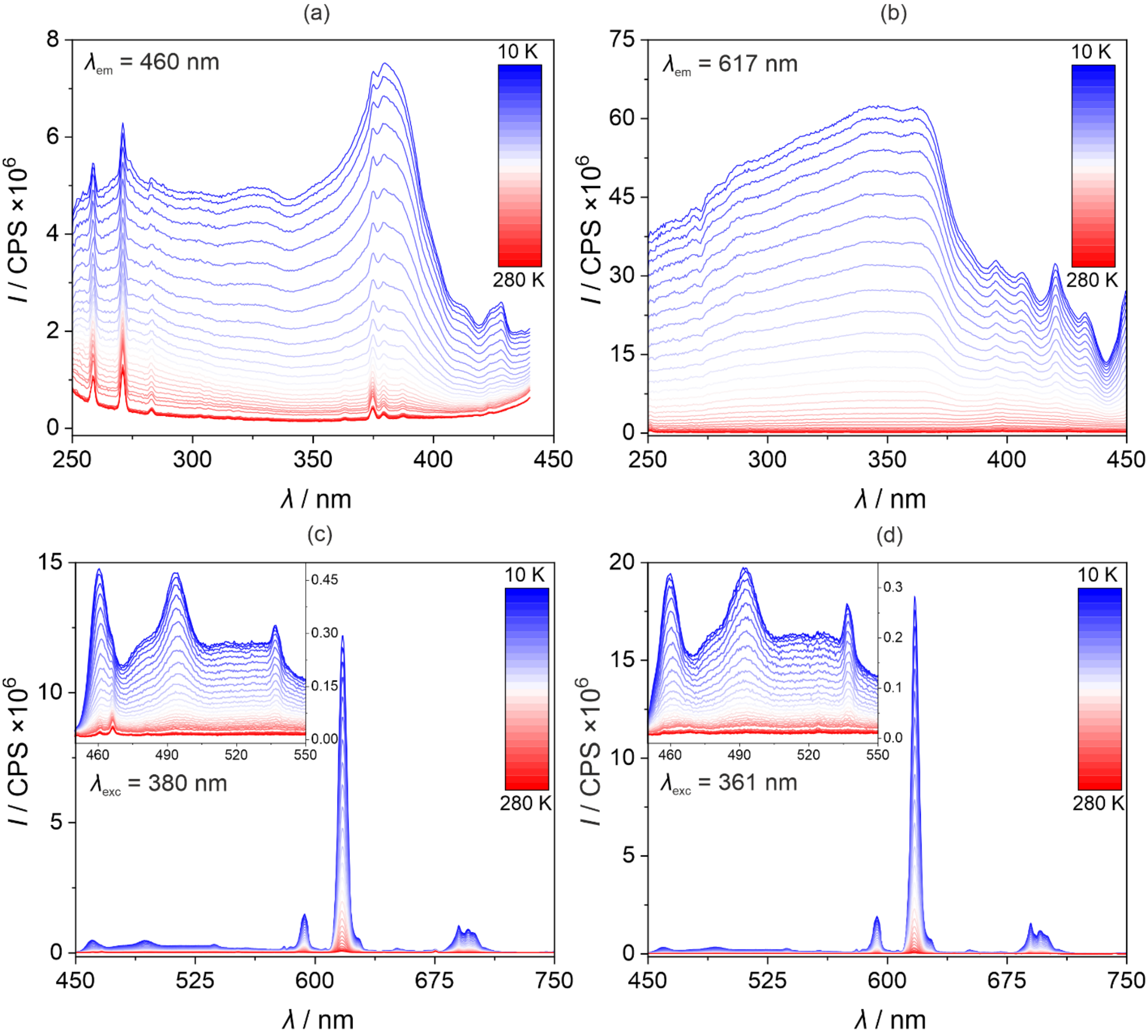

Fig. S13 Temperature-variable photoluminescent characteristics of **Eu$_2$FIr$_2$**, including the excitation spectra for the monitored emission at 460 nm (a), the excitation spectra for the monitored emission at 617 nm (b), the emission spectra under the 380 nm excitation (c), and the emission spectra under the 361 nm excitation (d). In (c) and (d), the inset contains the enlargement of the spectra for the limited wavelength range of 450–550 nm, corresponding to the emission of Ir(III) complexes.

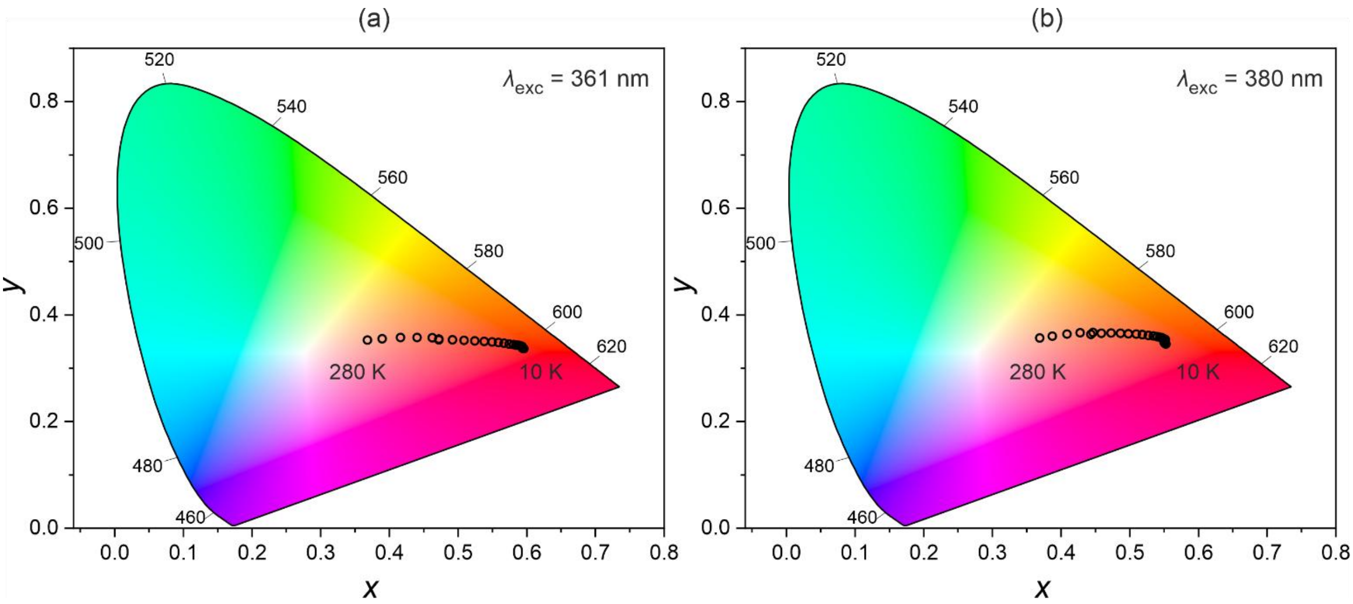

Fig. S14 The emission colors of **Eu_2FIr_2**, presented on the CIE 1931 chromaticity diagram, representing the temperature dependences of the emission under the 361 nm (a) and 380 nm (b) excitation. Corresponding *x* and *y* parameters were gathered in Table S8.

Table S8 The CIE 1931 chromaticity parameters of temperature-variable emission of **Eu_2FIr_2** for two indicated excitation wavelengths.

Temperature / K	**CIE 1931 chromaticity parameters**			
	λ_{exc} = 361 nm		λ_{exc} = 380 nm	
	x	***y***	***x***	***y***
10	0.596	0.336	0.553	0.345
20	0.595	0.337	0.552	0.346
30	0.594	0.338	0.551	0.348
40	0.594	0.338	0.550	0.349
50	0.594	0.339	0.550	0.350
60	0.594	0.340	0.550	0.351
70	0.594	0.340	0.552	0.352
80	0.594	0.340	0.552	0.353
90	0.593	0.341	0.551	0.354
100	0.591	0.342	0.550	0.355
110	0.588	0.343	0.549	0.356
120	0.585	0.343	0.547	0.357
130	0.581	0.344	0.544	0.358
140	0.575	0.345	0.540	0.359
150	0.567	0.347	0.534	0.360
160	0.559	0.348	0.527	0.361
170	0.550	0.349	0.519	0.363
180	0.538	0.350	0.510	0.364
190	0.524	0.351	0.498	0.364
200	0.509	0.352	0.487	0.365
210	0.492	0.353	0.473	0.366
220	0.472	0.353	0.459	0.365
230	0.472	0.355	0.444	0.363
240	0.462	0.357	0.446	0.367
250	0.440	0.358	0.428	0.366
260	0.416	0.357	0.409	0.364
270	0.390	0.355	0.387	0.360
280	0.368	0.352	0.369	0.356

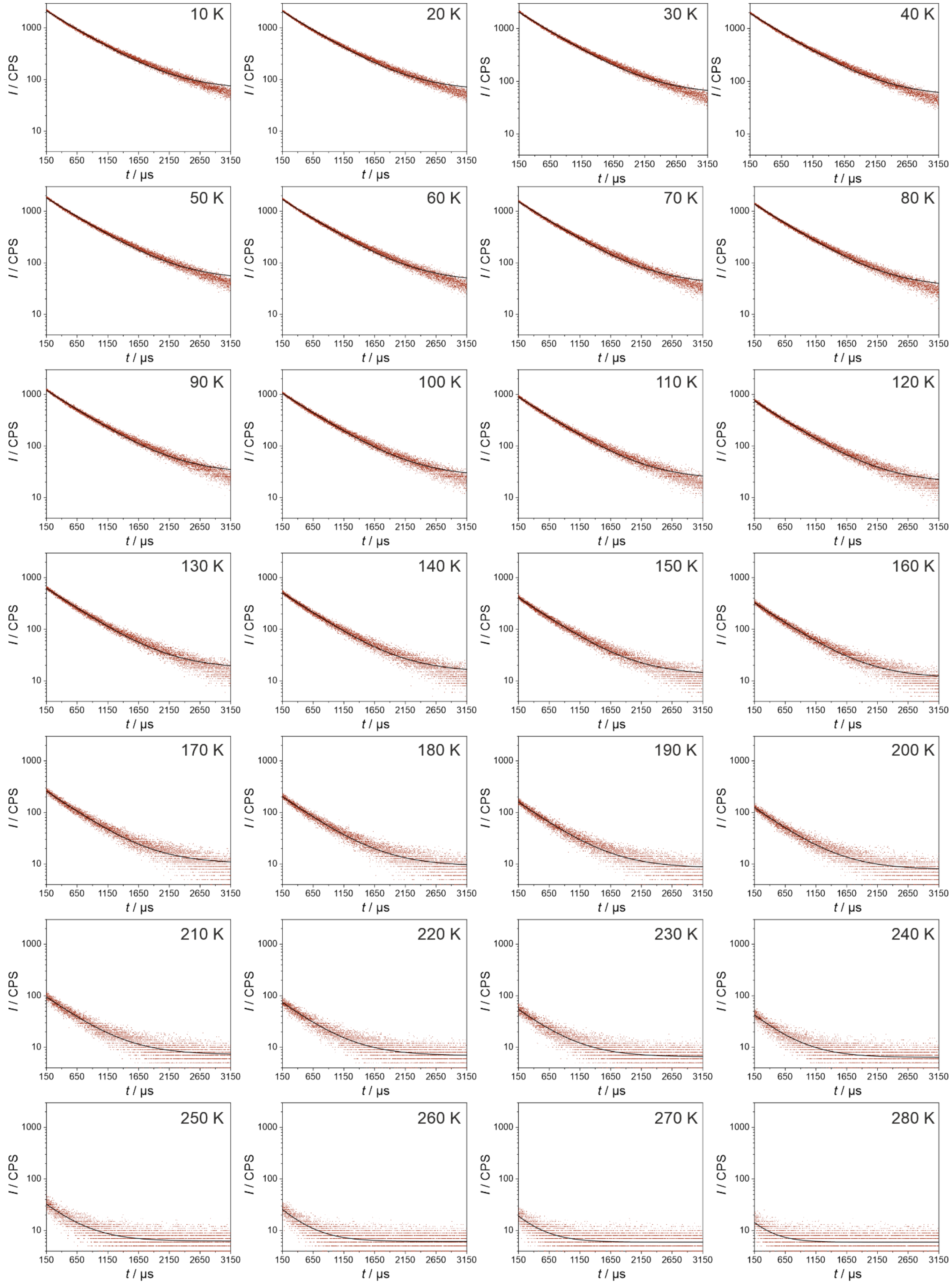

Fig. S15 Emission decay profiles for **Eu_2FIr_2** under the 361 nm excitation and the monitored 617 nm emission at variable indicated temperatures. Dots represent experimental data while solid lines show the best fits to the mono-exponential decay function (see Table S9 and the related comment).

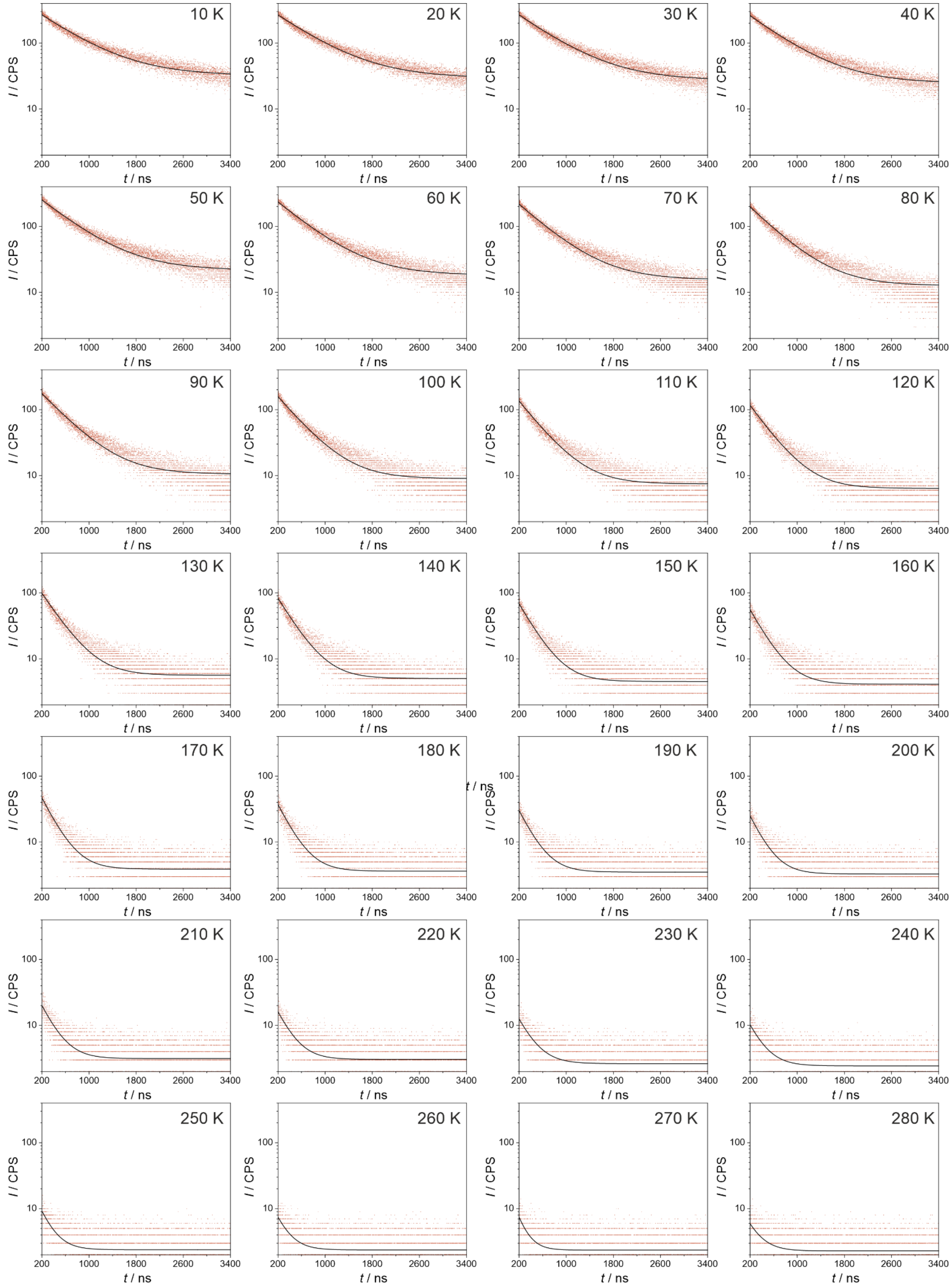

Fig. S16 Emission decay profiles for **Eu_2FIr_2** under the 374 nm excitation and the monitored 460 nm emission at variable indicated temperatures. Dots represent experimental data while solid lines show the best fits to the mono-exponential decay function (see Table S10 and the related comment).

Table S9 The best-fit parameters for emission decay profiles of **Eu_2FIr_2** for the emission at 617 nm under the excitation at 361 nm (see Fig. S15 and the comment below).

Temperature / K	τ(±τ) / µs	X^2	Temperature / K	τ (±τ) / µs	X^2
10	582.140(±0.919)	0.999	**150**	533.384(±1.510)	0.999
20	578.439(±0.899)	0.999	**160**	534.248(±1.709)	0.999
30	578.541(±0.927)	0.999	**170**	523.089(±1.916)	0.999
40	576.748(±0.910)	0.999	**180**	520.116(±2.135)	0.999
50	576.375(±0.920)	0.999	**190**	512.613(±2.409)	0.999
60	571.334(±0.924)	0.999	**200**	500.287(±2.621)	0.999
70	570.439(±0.951)	0.999	**210**	496.662(±3.132)	0.999
80	568.400(±0.985)	0.999	**220**	482.006(±3.606)	0.999
90	564.109(±1.001)	0.999	**230**	465.123(±4.416)	0.999
100	561.170(±1.058)	0.999	**240**	430.070(±4.853)	0.999
110	554.819(±1.114)	0.999	**250**	423.200(±6.205)	0.999
120	552.894(±1.195)	0.999	**260**	357.340(±6.628)	0.999
130	544.373(±1.305)	0.999	**270**	337.652(±8.863)	0.999
140	541.127(±1.408)	0.999	**280**	285.709(±11.877)	0.999

Table S10 The best-fit parameters for emission decay profiles of **Eu_2FIr_2** for the emission at 460 nm under the excitation at 374 nm (see Fig. S16 and the comment below).

Temperature / K	τ(±τ) / ns	X^2	Temperature / K	τ(±τ) / ns	X^2
10	668.977(±3.343)	0.999	**150**	270.489(±1.969)	0.999
20	670.470(±3.203)	0.999	**160**	261.789(±2.226)	0.999
30	651.779(±3.006)	0.999	**170**	236.886(±2.222)	0.999
40	629.741(±2.878)	0.999	**180**	231.620(±2.574)	0.999
50	592.487(±2.679)	0.999	**190**	226.177(±2.918)	0.999
60	565.758(±2.554)	0.999	**200**	218.366(±3.363)	0.999
70	529.262(±2.423)	0.999	**210**	220.906(±4.080)	0.999
80	491.804(±2.223)	0.999	**220**	216.022(±4.910)	0.999
90	454.981(±2.120)	0.999	**230**	222.297(±5.999)	0.999
100	410.043(±1.984)	0.999	**240**	212.199(±7.082)	0.999
110	378.795(±1.966)	0.999	**250**	188.024(±7.092)	0.999
120	345.113(±1.901)	0.999	**260**	188.443(±9.319)	0.999
130	315.884(±1.904)	0.999	**270**	148.560(±8.058)	0.999
140	288.284(±1.899)	0.999	**280**	198.891(±13.077)	0.999

Comment on the determination of emission lifetimes in Eu_2FIr_2 (Tables S9 and S10) and Eu_2Ir_2 (Tables S12 and S13): Fitting of the mono-exponential decay function was performed in the Origin software. The fitting function was as follows:

$$I = I_0 + Ae^{\frac{-t}{\tau}}$$

where:
I – intensity, I_0 – intensity offset (background), *A* – constant, *t* – time, *τ* – luminescence lifetime.
Application of the term connected with the background allowed all data to be fitted in the same range of time, and allowed for obtaining good fitting parameters.

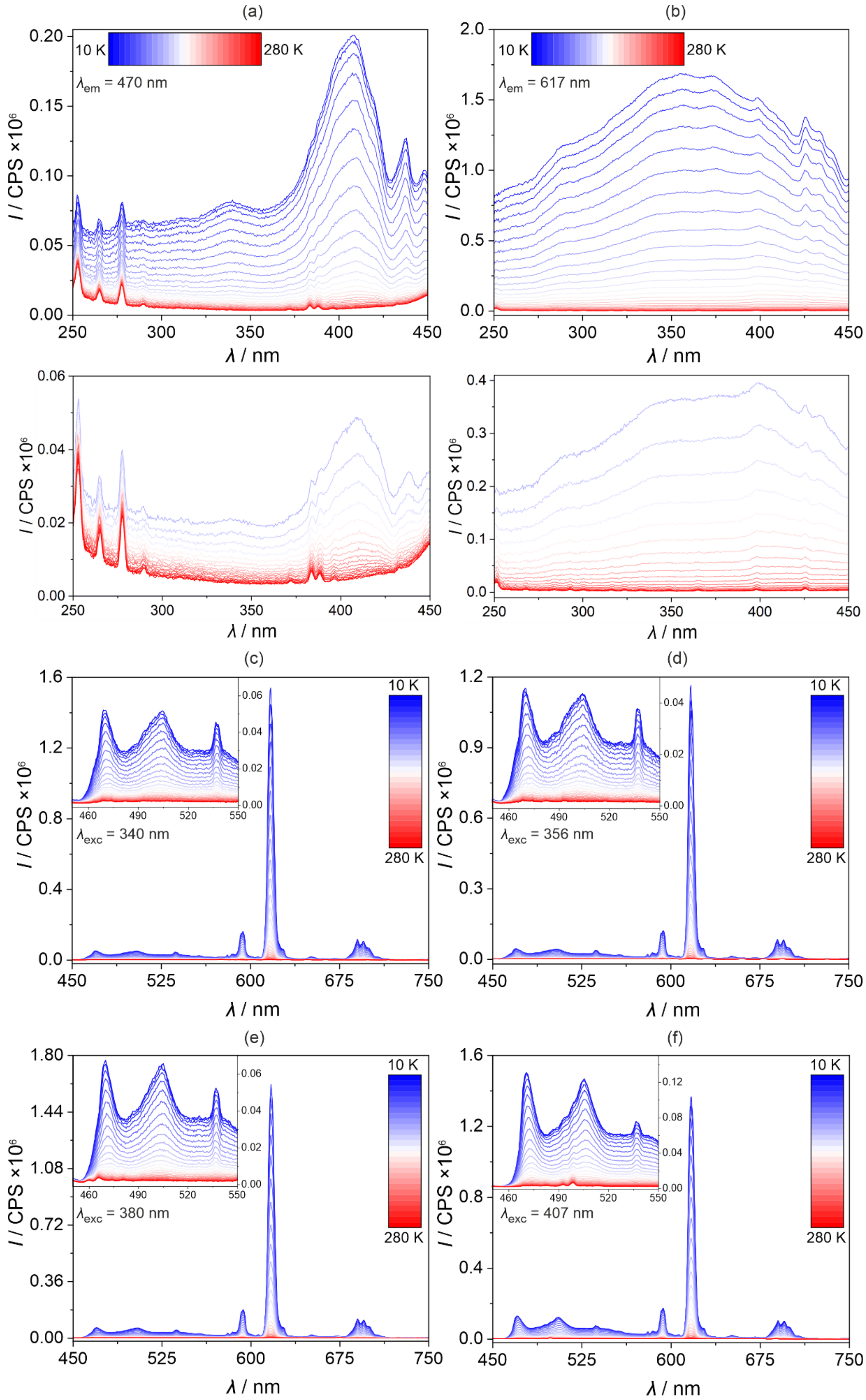

Fig. S17 Temperature-variable photoluminescent characteristics of **Eu_2Ir_2**, including the excitation spectra for the monitored emission at 470 nm (a, the bottom part shows the limited 120–280 K range), the excitation spectra for the monitored emission at 617 nm (b, the bottom part shows the limited 120–280 K range), the emission spectra under the 340 nm excitation (c), the emission spectra under the 356 nm excitation (d), the emission spectra under the 380 nm excitation (e), and the emission spectra under the 407 nm excitation (f). In (c), (d), (e), and (f), the inset contains the enlargement of the spectra for the limited wavelength range of 450–550 nm, corresponding to the emission of Ir(III) complexes.

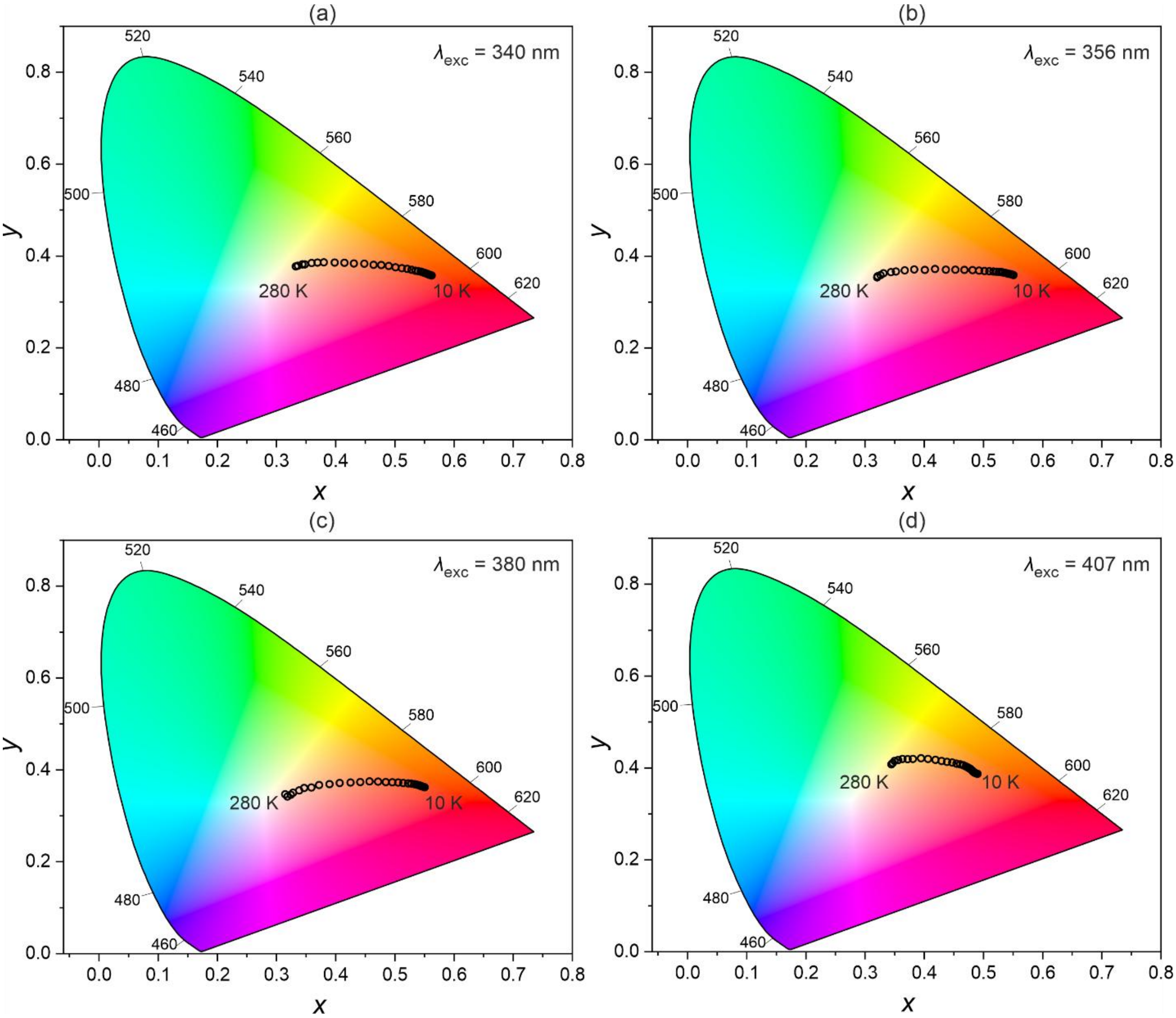

Fig. S18 The emission colors of **Eu_2Ir_2**, presented on the CIE 1931 chromaticity diagram, representing the temperature dependences of the emission under the 340 nm (a), 356 nm (b), 380 nm (c), and 407 nm (d) excitation. Corresponding *x* and *y* parameters were gathered in Table S11.

Table S11 The CIE 1931 chromaticity parameters of temperature-variable emission of **Eu$_2$Ir$_2$** for four indicated excitation wavelengths.

Temperature / K	CIE 1931 chromaticity parameters							
	λ_{exc} = 340 nm		λ_{exc} = 356 nm		λ_{exc} = 380 nm		λ_{exc} = 407 nm	
	x	y	x	y	x	y	x	y
10	0.563	0.358	0.551	0.359	0.315	0.347	0.490	0.387
20	0.560	0.359	0.548	0.360	0.551	0.362	0.487	0.388
30	0.557	0.360	0.546	0.361	0.549	0.363	0.485	0.389
40	0.555	0.361	0.543	0.362	0.546	0.364	0.484	0.390
50	0.553	0.362	0.539	0.363	0.544	0.365	0.483	0.392
60	0.550	0.363	0.536	0.364	0.542	0.366	0.482	0.393
70	0.547	0.365	0.533	0.364	0.540	0.367	0.480	0.395
80	0.544	0.366	0.530	0.365	0.536	0.368	0.479	0.396
90	0.539	0.367	0.526	0.365	0.533	0.369	0.478	0.398
100	0.535	0.368	0.522	0.366	0.528	0.370	0.476	0.399
110	0.528	0.370	0.517	0.366	0.523	0.370	0.473	0.401
120	0.521	0.372	0.510	0.367	0.514	0.371	0.470	0.404
130	0.512	0.373	0.502	0.367	0.506	0.372	0.466	0.406
140	0.501	0.375	0.493	0.368	0.496	0.373	0.461	0.408
150	0.490	0.378	0.482	0.369	0.485	0.373	0.455	0.409
160	0.477	0.380	0.468	0.370	0.472	0.374	0.447	0.412
170	0.464	0.381	0.453	0.370	0.457	0.375	0.439	0.413
180	0.448	0.383	0.437	0.370	0.441	0.373	0.429	0.415
190	0.431	0.384	0.418	0.372	0.425	0.372	0.419	0.417
200	0.415	0.385	0.401	0.370	0.407	0.371	0.406	0.419
210	0.398	0.385	0.383	0.371	0.390	0.369	0.395	0.421
220	0.380	0.386	0.367	0.369	0.372	0.367	0.381	0.420
230	0.370	0.386	0.352	0.366	0.359	0.361	0.372	0.419
240	0.359	0.385	0.344	0.365	0.347	0.360	0.363	0.420
250	0.348	0.382	0.331	0.362	0.339	0.355	0.356	0.417
260	0.344	0.382	0.326	0.359	0.328	0.350	0.350	0.415
270	0.336	0.379	0.321	0.356	0.324	0.346	0.347	0.411
280	0.333	0.377	0.321	0.353	0.319	0.342	0.344	0.408

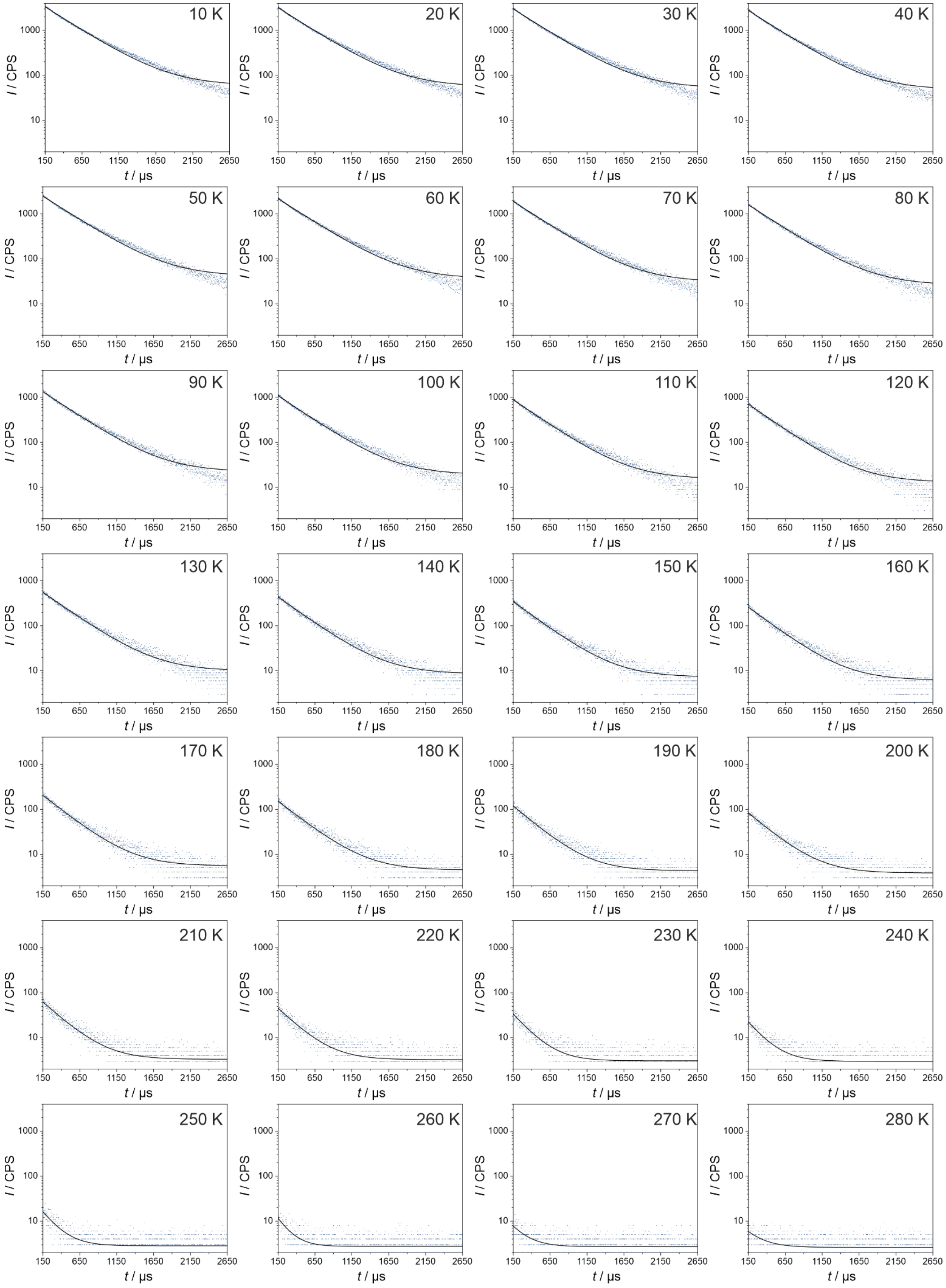

Fig. S19 Emission decay profiles for **Eu_2Ir_2** under the 356 nm excitation and the monitored 617 nm emission at variable indicated temperatures. Dots represent experimental data while solid lines show the best fits to the mono-exponential decay function (see Table S12).

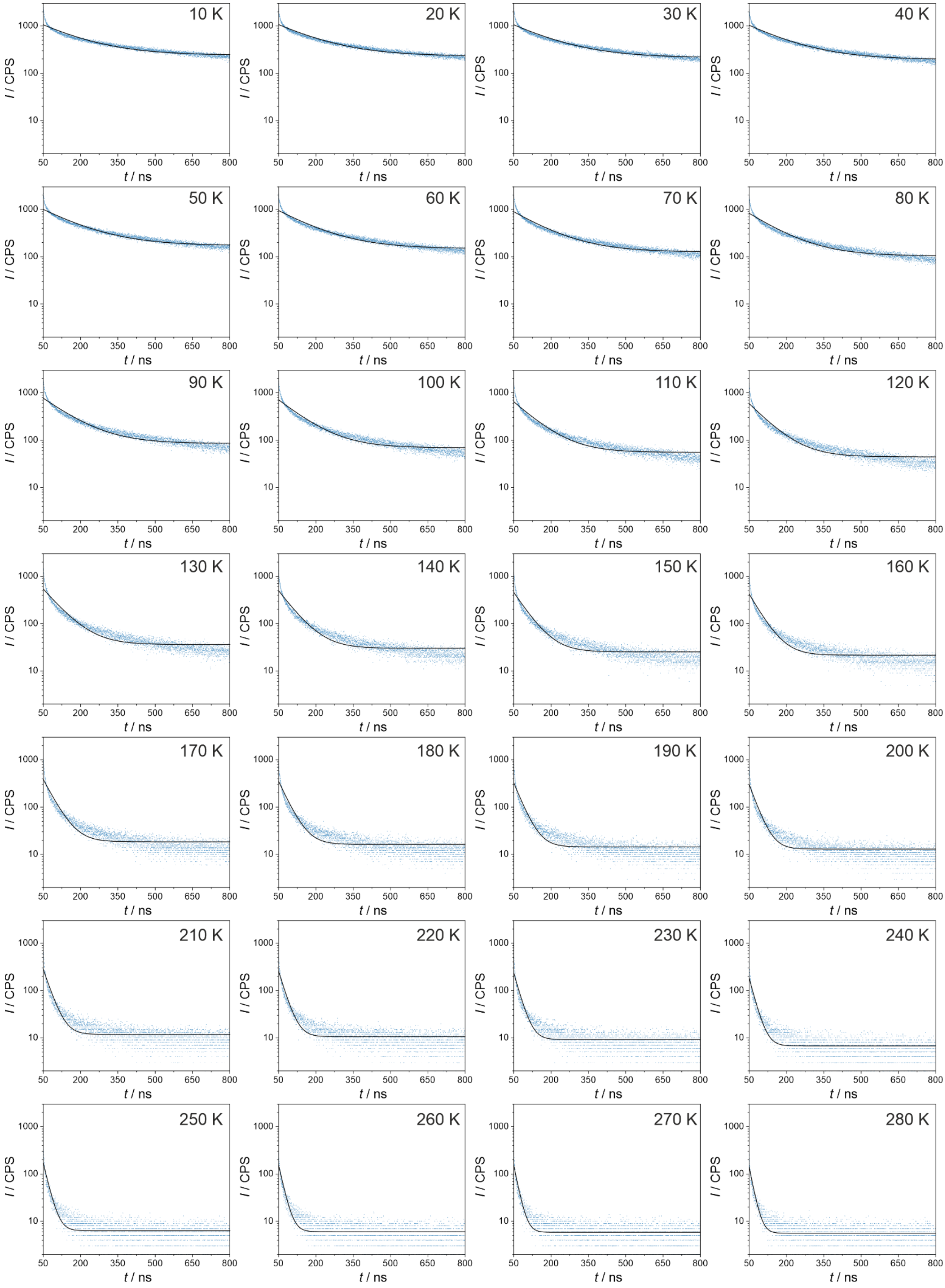

Fig. S20 Emission decay profiles for **Eu_2Ir_2** under the 374 nm excitation and the monitored 470 nm emission at variable indicated temperatures. Dots represent experimental data while solid lines show the best fits to the mono-exponential decay function (see Table S13).

Table S12 The best-fit parameters for emission decay profiles of **Eu$_2$Ir$_2$** for the emission at 617 nm under the excitation at 356 nm (see Fig. S19 and the comment placed below Table S10).

Temperature / K	τ(±τ) / μs	X^2	Temperature / K	τ(±τ) / μs	X^2
10	412.633(±1.230)	0.999	**150**	355.214(±2.145)	0.999
20	409.920(±1.228)	0.999	**160**	351.579(±2.475)	0.999
30	410.540(±1.177)	0.999	**170**	332.431(±2.537)	0.999
40	407.313(±1.260)	0.999	**180**	336.015(±2.984)	0.999
50	410.168(±1.280)	0.999	**190**	307.862(±3.448)	0.999
60	407.540(±1.294)	0.999	**200**	308.599(±3.799)	0.999
70	405.559(±1.293)	0.999	**210**	286.961(±4.153)	0.999
80	401.399(±1.329)	0.999	**220**	268.030(±5.273)	0.999
90	394.430(±1.492)	0.999	**230**	227.890(±5.196)	0.999
100	388.149(±1.531)	0.999	**240**	211.437(±6.793)	0.999
110	385.506(±1.587)	0.999	**250**	192.326(±8.980)	0.999
120	377.681(±1.703)	0.999	**260**	156.187(±10.868)	0.999
130	377.844(±1.825)	0.999	**270**	189.392(±20.279)	0.999
140	366.785(±2.029)	0.999	**280**	206.265(±32.178)	0.999

Table S13 The best-fit parameters for emission decay profiles of **Eu$_2$Ir$_2$** for the emission at 470 nm under the excitation at 374 nm (see Fig. S20 and the comment placed below Table S10).

Temperature / K	τ(±τ) / ns	X^2	Temperature / K	τ(±τ) / ns	X^2
10	156.537(±1.383)	0.999	**150**	53.962(±0.507)	0.999
20	157.354(±1.311)	0.999	**160**	46.815(±0.455)	0.999
30	157.936(±1.308)	0.999	**170**	42.259(±0.426)	0.999
40	153.837(±1.232)	0.999	**180**	37.314(±0.398)	0.999
50	147.062(±1.137)	0.999	**190**	32.959(±0.369)	0.999
60	139.369(±1.074)	0.999	**200**	29.582(±0.340)	0.999
70	129.621(±0.996)	0.999	**210**	27.451(±0.327)	0.999
80	121.352(±0.939)	0.999	**220**	24.637(±0.298)	0.999
90	109.421(±0.856)	0.999	**230**	22.726(±0.288)	0.999
100	99.851(±0.788)	0.999	**240**	21.427(±0.272)	0.999
110	88.882(±0.717)	0.999	**250**	19.372(±0.257)	0.999
120	79.164(±0.660)	0.999	**260**	18.055(±0.255)	0.999
130	70.012(±0.609)	0.999	**270**	16.316(±0.249)	0.999
140	61.363(±0.546)	0.999	**280**	15.941(±0.240)	0.999

Comment on ratiometric optical thermometry studies

Compounds **Eu_2FIr_2** and **Eu_2Ir_2** exhibit temperature-dependent photoluminescence in the temperature range from 10 to 280 K. During the analysis of the related data, a few different approaches toward ratiometric optical thermometry were tested. The first approach was based on the ratios between emission/excitation intensities at two specific wavelengths at which maxima were present at 10 K (e.g., $I_{617.0}/I_{470.0}$). In this manner, most of the thermometric parameters were established; it is worth mentioning that this approach was used both for excitation and emission spectra. The second approach was based on the ratio between areas under the signal and was performed only for emission spectra due to the good separation of the emission bands. The acronyms of the signal are: A_{Ir} – emission integrated in the region of 440–540 nm for **Eu_2FIr_2** and 450-550 nm for **Eu_2Ir_2**, A_{590} – emission integrated in the 582–604 nm range, A_{617} - emission integrated in the 610–630 nm range, A_{690} - emission integrated in the 680–715 nm range. Emission lifetime is independent of such parameters as the amount of the sample, size of the crystals, and experimental setup, thus the thermal dependency of emission lifetime can be used directly as a thermometric parameter. Moreover, the ratio of emission lifetimes for two different metal centers was also considered as a thermometric parameter. For all of the temperature-dependent thermometric parameters Δ constructed based on emission intensities, a classical Mott-Seitz model was applied, under the assumption of the existence of one or two nonradiative channels of emission quenching:

$$\Delta(T) = \frac{\Delta_0}{1 + \alpha\ exp\left(\frac{-\Delta E}{k_B T}\right)}\ or\ \Delta(T) = \frac{\Delta_0}{1 + \alpha_1\ exp\left(\frac{-\Delta E_1}{k_B T}\right) + \alpha_2\ exp\left(\frac{-\Delta E_2}{k_B T}\right)}$$

where:
Δ_0 = thermometric parameter at 0 K,
$\alpha_x = \frac{W_0}{W_R}$ the ratio of non-radiative (W_0 at 0 K) and radiative (W_R) rates of decay,
ΔE_x = activation energy of non-radiative channel.
All parameters obtained from the fitting following the above-presented equation to the gathered experimental points are presented in Tables S14–S23. To compare the performance of different thermometer parameters, a relative thermal sensitivity (S_r), derived from fitted curves, was used:

$$S_r = \frac{\left|\frac{\partial \Delta}{\partial T}\right|}{\Delta}$$

Then, temperature uncertainty was calculated, for the ratios of intensities, by the following equation:

$$\delta T = \left(\frac{\delta\Delta}{\Delta}\right)\left(\frac{1}{Sr}\right) = \left(\sqrt{\left(\frac{\delta_{DET}}{I_1}\right)^2 + \left(\frac{\delta_{DET}}{I_2}\right)^2}\right)\left(\frac{1}{Sr}\right)$$

However, for the temperature uncertainty of thermometric parameters derived from the areas under the curve, a different function was applied:

$$\delta T = \left(\frac{\delta\Delta}{\Delta}\right)\left(\frac{1}{Sr}\right) = \left(\sqrt{\left(\frac{\delta_{DET}\sqrt{0.5\ nm \times \lambda_{range\ 1}}}{A_1}\right)^2 + \left(\frac{\delta_{DET}\sqrt{0.5\ nm \times \lambda_{range\ 2}}}{A_2}\right)^2}\right)\left(\frac{1}{Sr}\right)$$

where:
$\frac{\delta\Delta}{\Delta}$ is the uncertainty of the thermometric parameter, S_r is the relative thermal sensitivity, δ_{DET} in the uncertainty of the detector equal to 100 CPS (value determined based on the standard deviation of the noise related to the accessible detector), I_1 and I_2 are the values of the intensity at specific points in a non-normalized, non-smoothed emission spectrum, A_1 and A_2 are areas under different emission bands, 0.5 nm is related to the wavelength increment and $\lambda_{range\ 1}$ and $\lambda_{range\ 2}$ are the range of integration for selected bands. Despite excellent fitting parameters, some parameters of the Mott-Seitz model were found with high uncertainty and should be considered with great caution.[S16]

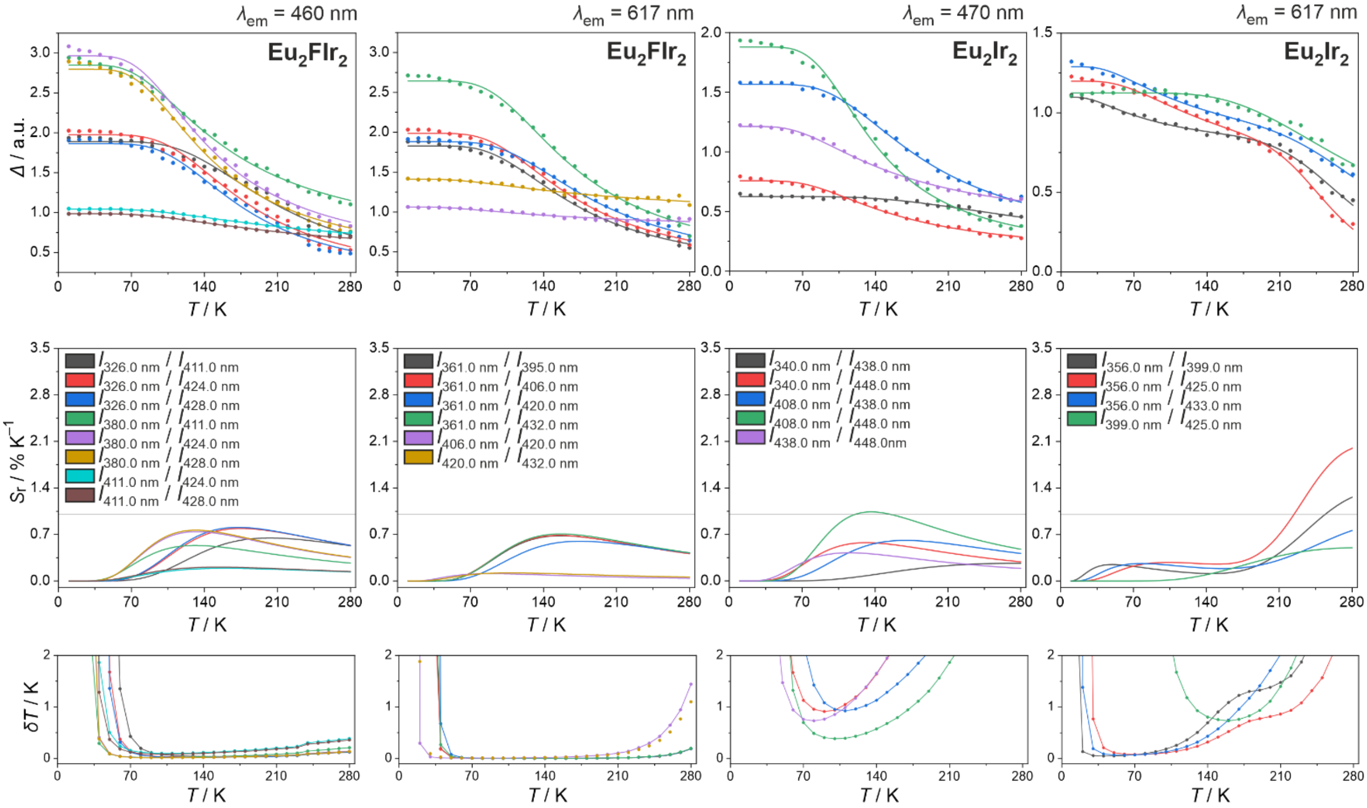

Fig. S21 The full set of the characteristics of ratiometric optical thermometry based on temperature-variable excitation spectra of **Eu$_2$FIr$_2$** (left side, based on the spectra presented in Fig. S13) and **Eu$_2$Ir$_2$** (right side, based on the spectra presented in Fig. S17), including the temperature dependences of thermometric parameters defined as depicted in the figures, based on the excitation spectra for the indicated monitored emission maxima (top part), the resulting temperature dependences of relative thermal sensitivity (middle part), and the related temperature uncertainties (bottom part). The experimental data in the top part (colored points) were fitted to the Mott-Seitz model (see the Comment on ratiometric optical thermometry studies above). The best-fit curves are shown as colored solid lines, while the resulting best-fit parameters are gathered in Table S14. The relative thermal sensitivity and temperature uncertainties were calculated based on the corresponding $\Delta(T)$ dependences (see the Comment on ratiometric optical thermometry studies above).

Table S14 Best-fit parameters to the Mott-Seitz model for the ratiometric luminescent thermometry based on the excitation spectra of **Eu$_2$FIr$_2$** and **Eu$_2$Ir$_2$** (see Fig. S21 for the related optical characteristics).

Δ	**Parameters of the Mott-Seitz model**					X^2
	Δ_0	α_1	α_2	ΔE_1 / kJ mol^{-1}	ΔE_2 / kJ mol^{-1}	
λ_{em} = 460 nm	Compound **Eu$_2$FIr$_2$**					
$\frac{I_{326.0\ nm}}{I_{411.0\ nm}}$	1.890 (±0.018)	17.976 (±3.297)	0	5.578 (±0.337)	0	0.999
$\frac{I_{326.0\ nm}}{I_{424.0\ nm}}$	1.975 (±0.020)	20.375 (±3.055)	0	4.922 (±0.254)	0	0.999
$\frac{I_{326.0\ nm}}{I_{428.0\ nm}}$	1.864 (±0.019)	20.602 (±2.932)	0	4.855 (±0.239)	0	0.999
$\frac{I_{380.0\ nm}}{I_{411.0\ nm}}$	2.850 (±0.020)	5.224 (±0.329)	0	2.944 (±0.106)	0	0.999
$\frac{I_{380.0\ nm}}{I_{424.0nm}}$	2.965 (±0.022)	9.710 (±0.670)	0	3.286 (±0.108)	0	0.999
$\frac{I_{380.0\ nm}}{I_{428.0\ nm}}$	2.798 (±0.021)	10.193 (±0.701)	0	3.296 (±0.107)	0	0.999
$\frac{I_{411.0\ nm}}{I_{424.0\ nm}}$	1.044 (±0.003)	1.526 (±0.074)	0	3.061 (±0.096)	0	0.999
$\frac{I_{411.0\ nm}}{I_{428.0\ nm}}$	0.986 (±0.003)	1.623 (±0.075)	0	2.956 (±0.090)	0	0.999
λ_{em} = 617 nm	Compound **Eu$_2$FIr$_2$**					
$\frac{I_{361.0\ nm}}{I_{395.0\ nm}}$	1.829 (±0.012)	11.504 (±0.895)	0	4.004 (±0.130)	0	0.999
$\frac{I_{361.0\ nm}}{I_{406.0\ nm}}$	1.987 (±0.012)	11.418 (±0.805)	0	3.957 (±0.118)	0	0.999
$\frac{I_{361.0\ nm}}{I_{420.0\ nm}}$	1.883 (±0.011)	11.035 (±0.939)	0	4.436 (±0.151)	0	0.999
$\frac{I_{361.0\ nm}}{I_{432.0\ nm}}$	2.644 (±0.018)	12.367 (±0.977)	0	4.041 (±0.131)	0	0.999
$\frac{I_{406.0\ nm}}{I_{420.0\ nm}}$	1.062 (±0.007)	0.405 (±0.039)	0	1.562 (±0.191)	0	0.999
$\frac{I_{320.0\ nm}}{I_{432.0\ nm}}$	1.411 (±0.009)	0.566 (±0.056)	0	1.933 (±0.198)	0	0.999
λ_{em} = 470 nm	Compound **Eu$_2$Ir$_2$**					
$\frac{I_{340.0\ nm}}{I_{438.0\ nm}}$	0.625 (±0.004)	5.641 (±1.818)	0	6.265 (±0.670)	0	0.999
$\frac{I_{340.0\ nm}}{I_{448.0\ nm}}$	0.758 (±0.006)	5.975 (±0.429)	0	3.020 (±0.119)	0	0.999
$\frac{I_{408.0\ nm}}{I_{438.0\ nm}}$	1.567 (±0.007)	10.714 (±0.663)	0	4.266 (±0.108)	0	0.999
$\frac{I_{408.0\ nm}}{I_{448.0\ nm}}$	1.880 (±0.013)	21.569 (±1.551)	0	3.869 (±0.103)	0	0.999
$\frac{I_{438.0\ nm}}{I_{448.0\ nm}}$	1.213 (±0.006)	2.943 (±0.124)	0	2.384 (±0.073)	0	0.999
λ_{em} = 617 nm	Compound **Eu$_2$Ir$_2$**					
$\frac{I_{356.0\ nm}}{I_{399.0\ nm}}$	1.097 (±0.011)	1704.610 (±1035.538)	0.518 (±0.048)	16.774 (±1.348)	0.878 (±0.113)	0.999
$\frac{I_{356.0\ nm}}{I_{425.0\ nm}}$	1.198 (±0.009)	15152.961 (±11219.332)	1.438 (±0.225)	19.979 (±1.623)	1.973 (±0.198)	0.999
$\frac{I_{356.0\ nm}}{I_{433.0\ nm}}$	1.289 (±0.011)	447.212 (±463.448)	0.928 (±0.115)	15.177 (±2.392)	1.425 (±0.149)	0.999
$\frac{I_{399.0\ nm}}{I_{425.0\ nm}}$	1.124 (±0.007)	22.585 (±6.657)	0	8.224 (±0.611)	0	0.999

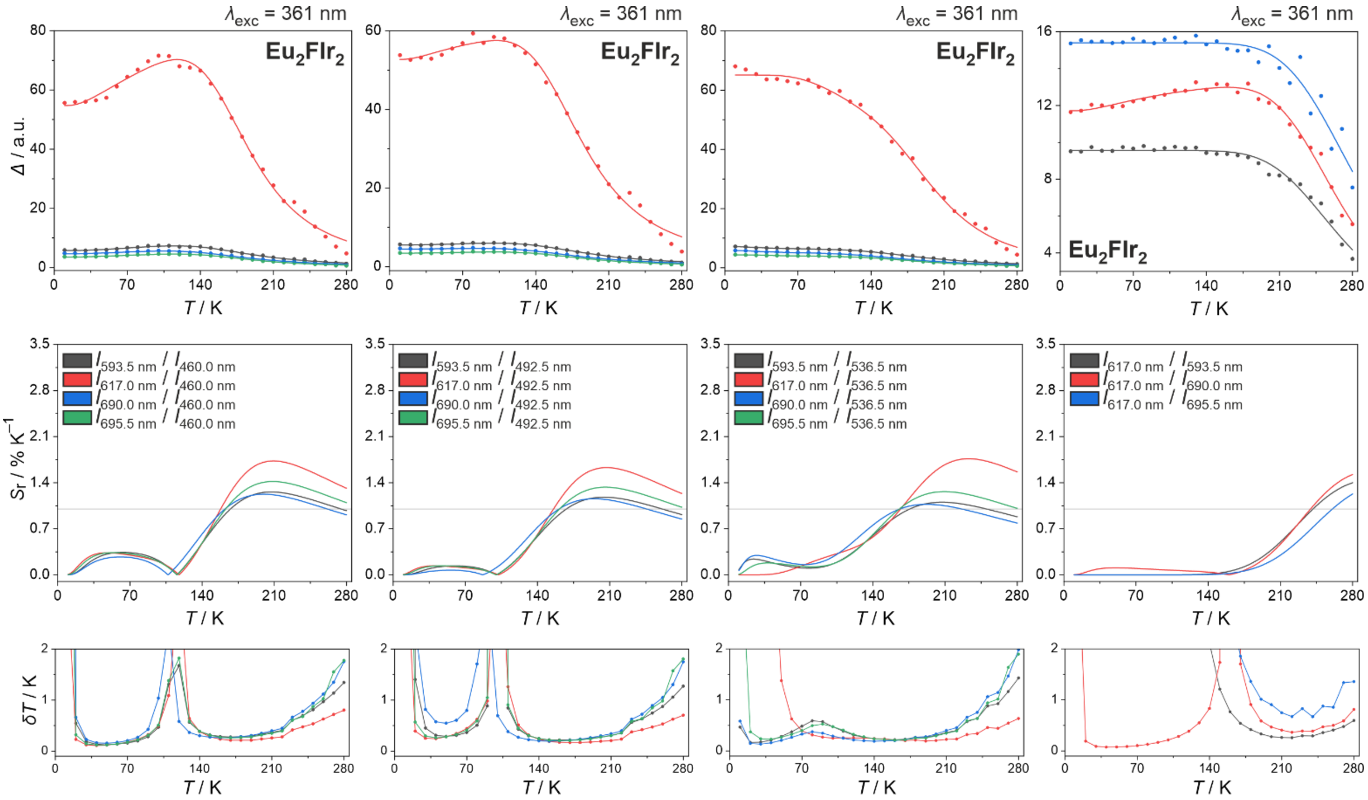

Fig. S22 The full set of the characteristics of ratiometric optical thermometry based on temperature-variable emission spectra of **Eu_2FIr_2** (the 361 nm excitation, based on the spectra presented in Fig. S13), divided into four parts (columns) representing different types of applied intensity ratios. In each case, the set of data includes the temperature dependences of thermometric parameters defined as depicted in the figures (top part), the resulting temperature dependences of relative thermal sensitivity (middle part), and the related temperature uncertainties (bottom part). The experimental data in the top part (colored points) were fitted to the Mott-Seitz model (see the Comment on ratiometric optical thermometry studies above). The best-fit curves are shown as colored solid lines, while the resulting best-fit parameters are gathered in Table S15. The relative thermal sensitivity and temperature uncertainties were calculated based on the corresponding $\Delta(T)$ dependences (see the Comment on ratiometric optical thermometry studies above).

Table S15 Best-fit parameters to the Mott-Seitz model for the ratiometric luminescent thermometry based on the emission spectra of **Eu_2FIr_2** under the 361 nm excitation (see Fig. S22 for the related optical characteristics).

Δ	Parameters of the Mott-Seitz model					X^2
	Δ_0	α_1	α_2	ΔE_1 / kJ mol^{-1}	ΔE_2 / kJ mol^{-1}	
$\frac{I_{593.5\,\mathrm{nm}}}{I_{460.0\,\mathrm{nm}}}$	5.767 (±0.108)	-0.660 (±0.154)	83.920 (±18.348)	0.961 (±0.217)	7.604 (±0.457)	0.999
$\frac{I_{617.0\,\mathrm{nm}}}{I_{460.0\,\mathrm{nm}}}$	54.731 (±1.344)	337.632 (±101.933)	-0.504 (±0.094)	9.614 (±0.559)	0.729 (±0.193)	0.999
$\frac{I_{690.0\,\mathrm{nm}}}{I_{460.0\,\mathrm{nm}}}$	4.685 (±0.090)	74.676 (±17.001)	-0.538 (±0.184)	7.131 (±0.473)	0.957 (±0.300)	0.999
$\frac{I_{695.5\,\mathrm{nm}}}{I_{460.0\,\mathrm{nm}}}$	3.555 (±0.084)	139.027 (±36.598)	-0.560 (±0.122)	8.360 (±0.517)	0.812 (±0.214)	0.999
$\frac{I_{593.5\,\mathrm{nm}}}{I_{492.5\,\mathrm{nm}}}$	5.533 (±0.084)	84.276 (±18.040)	-0.293 (±0.168)	7.377 (±0.446)	120.123 (±60.373)	0.999
$\frac{I_{617.0\,\mathrm{nm}}}{I_{492.5\,\mathrm{nm}}}$	52.734 (±1.231)	315.815 (±92.858)	-0.193 (±0.085)	9.193 (±0.535)	77.939 (±51.645)	0.999
$\frac{I_{690.0\,\mathrm{nm}}}{I_{492.5\,\mathrm{nm}}}$	4.494 (±0.082)	-0.153 (±0.225)	72.956 (±18.122)	0.977 (±1.202)	821.534 (±61.702)	0.999
$\frac{I_{695.5\,\mathrm{nm}}}{I_{492.5\,\mathrm{nm}}}$	3.419 (±0.074)	134.847 (±35.632)	-0.224 (±0.117)	8.033 (±0.510)	90.518 (±57.892)	0.999
$\frac{I_{593.5\,\mathrm{nm}}}{I_{536.5\,\mathrm{nm}}}$	7.147 (±0.114)	97.975 (±14.879)	0.230 (±0.036)	7.434 (±0.286)	0.415 (±0.132)	0.999
$\frac{I_{617.0\,\mathrm{nm}}}{I_{536.5\,\mathrm{nm}}}$	65.126 (±0.656)	1556.637 (±1127.311)	3.401 (±2.539)	12.420 (±1.554)	3.059 (±0.760)	0.999
$\frac{I_{690.0\,\mathrm{nm}}}{I_{536.5\,\mathrm{nm}}}$	5.816 (±0.091)	74.261 (±11.282)	0.325 (±0.052)	6.579 (±0.283)	0.474 (±0.125)	0.999
$\frac{I_{695.5\,\mathrm{nm}}}{I_{536.5\,\mathrm{nm}}}$	4.362 (±0.071)	164.156 (±37.192)	0.272 (±0.080)	8.173 (±0.429)	0.653 (±0.256)	0.999
$\frac{I_{617.0\,\mathrm{nm}}}{I_{593.5\,\mathrm{nm}}}$	9.557 (±0.063)	1342.351 (±731.998)	0	16.168 (±1.154)	0	0.999
$\frac{I_{617.0\,\mathrm{nm}}}{I_{690.0\,\mathrm{nm}}}$	11.715 (±0.184)	1915.383 (±1083.864)	-0.188 (±0.043)	17.153 (±1.251)	0.811 (±0.326)	0.999
$\frac{I_{617.0\,\mathrm{nm}}}{I_{695.5\,\mathrm{nm}}}$	15.398 (±0.139)	1631.744 (±1720.830)	0	17.654 (±2.287)	0	0.999

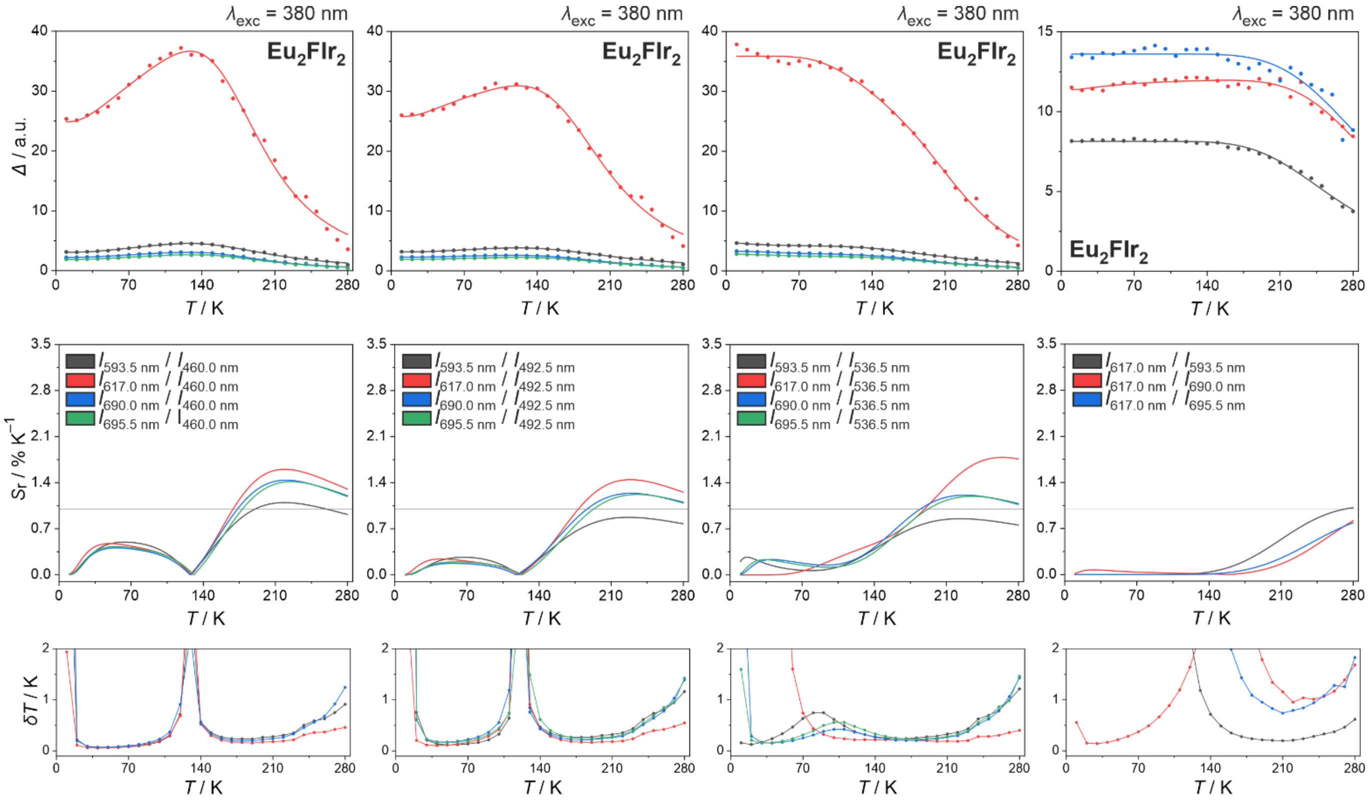

Fig. S23 The full set of the characteristics of ratiometric optical thermometry based on temperature-variable emission spectra of **Eu_2FIr_2** (the 380 nm excitation, based on the spectra presented in Fig. S13), divided into four parts (columns) representing different types of applied intensity ratios. In each case, the set of data includes the temperature dependences of thermometric parameters defined as depicted in the figures (top part), the resulting temperature dependences of relative thermal sensitivity (middle part), and the related temperature uncertainties (bottom part). The experimental data in the top part (colored points) were fitted to the Mott-Seitz model (see the Comment on ratiometric optical thermometry studies above). The best-fit curves are shown as colored solid lines, while the resulting best-fit parameters are gathered in Table S16. The relative thermal sensitivity and temperature uncertainties were calculated based on the corresponding $\Delta(T)$ dependences (see the Comment on ratiometric optical thermometry studies above).

Table S16 Best-fit parameters to the Mott-Seitz model for the ratiometric luminescent thermometry based on the emission spectra of **Eu_2FIr_2** under the 380 nm excitation (see Fig. S23 for the related optical characteristics).

Δ	Parameters of the Mott-Seitz model					X^2
	Δ_0	α_1	α_2	ΔE_1 / kJ mol^{-1}	ΔE_2 / kJ mol^{-1}	
$\frac{I_{593.5\,\mathrm{nm}}}{I_{460.0\,\mathrm{nm}}}$	3.066 (±0.072)	49.841 (±11.564)	-0.863 (±0.140)	7.466 (±0.521)	0.903 (±0.161)	0.999
$\frac{I_{617.0\,\mathrm{nm}}}{I_{460.0\,\mathrm{nm}}}$	24.845 (±0.711)	-0.685 (±0.088)	238.925 (±72.241)	0.724 (±0.145)	9.758 (±0.588)	0.999
$\frac{I_{690.0\,\mathrm{nm}}}{I_{460.0\,\mathrm{nm}}}$	2.193 (±0.056)	-0.671 (±0.111)	162.873 (±47.628)	0.821 (±0.178)	9.179 (±0.589)	0.999
$\frac{I_{695.5\,\mathrm{nm}}}{I_{460.0\,\mathrm{nm}}}$	1.855 (±0.049)	-0.694 (±0.105)	160.914 (±48.244)	0.813 (±0.167)	9.399 (±0.612)	0.999
$\frac{I_{593.5\,\mathrm{nm}}}{I_{492.5\,\mathrm{nm}}}$	3.175 (±0.059)	36.917 (±9.755)	-0.584 (±0.198)	7.133 (±0.635)	1.066 (±0.314)	0.999
$\frac{I_{617.0\,\mathrm{nm}}}{I_{492.5\,\mathrm{nm}}}$	25.771 (±0.554)	-0.364 (±0.073)	251.774 (±71.098)	0.713 (±0.219)	9.968 (±0.559)	0.999
$\frac{I_{690.0\,\mathrm{nm}}}{I_{492.5\,\mathrm{nm}}}$	2.273 (±0.047)	-0.337 (±0.130)	143.678 (±45.433)	0.904 (±0.393)	9.104 (±0.657)	0.999
$\frac{I_{695.5\,\mathrm{nm}}}{I_{492.5\,\mathrm{nm}}}$	1.925 (±0.034)	144.582 (±40.842)	-0.386 (±0.111)	9.380 (±0.597)	0.931 (±0.301)	0.999
$\frac{I_{593.5\,\mathrm{nm}}}{I_{536.5\,\mathrm{nm}}}$	4.666 (±0.114)	0.172 (±0.028)	54.756 (±9.395)	0.280 (±0.135)	7.315 (±0.344)	0.999
$\frac{I_{617.0\,\mathrm{nm}}}{I_{536.5\,\mathrm{nm}}}$	35.858 (±0.305)	4083.998 (±4566.399)	7.295 (±4.799)	15.706 (±2.548)	4.167 (±0.766)	0.999
$\frac{I_{690.0\,\mathrm{nm}}}{I_{536.5\,\mathrm{nm}}}$	3.270 (±0.051)	205.334 (±55.889)	0.386 (±0.082)	9.147 (±0.538)	0.711 (±0.195)	0.999
$\frac{I_{695.5\,\mathrm{nm}}}{I_{536.5\,\mathrm{nm}}}$	2.786 (±0.052)	210.431 (±62.690)	0.312 (±0.064)	9.461 (±0.590)	0.585 (±0.195)	0.999
$\frac{I_{617.0\,\mathrm{nm}}}{I_{593.5\,\mathrm{nm}}}$	8.141 (±0.032)	245.157 (±60.207)	0	12.552 (±0.513)	0	0.999
$\frac{I_{617.0\,\mathrm{nm}}}{I_{690.0\,\mathrm{nm}}}$	11.369 (±0.248)	-0.073 (±0.025)	728.734 (±823.373)	0.458 (±0.453)	17.364 (±2.559)	0.999
$\frac{I_{617.0\,\mathrm{nm}}}{I_{695.5\,\mathrm{nm}}}$	13.613 (±0.117)	286.166 (±290.687)	0	14.590 (±2.207)	0	0.999

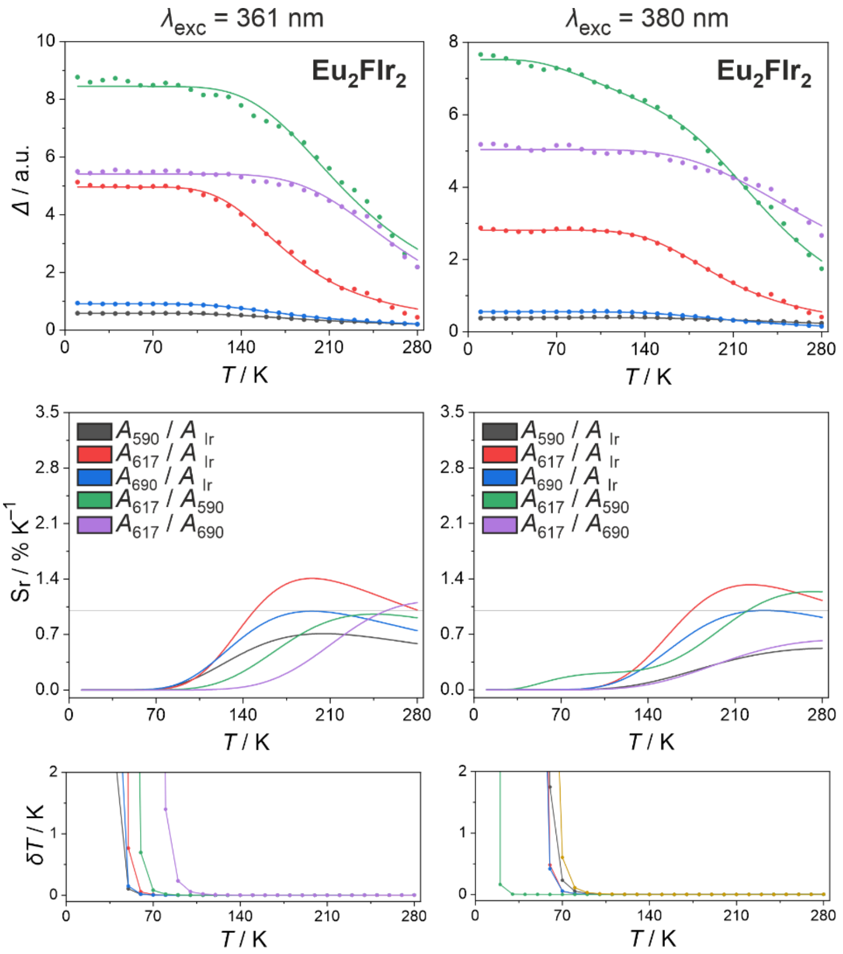

Fig. S24 The full set of the characteristics of ratiometric optical thermometry based on temperature-variable emission spectra of **Eu_2FIr_2** using the ratios between the integrated areas of the indicated emission peaks (the maxima are indicated for the case of Eu(III)-based emission while the "Ir" stands for the broadband emission of Ir(III) complexes, the respective emission spectra are shown in Fig. S13) instead of the ratios between the intensities for the selected emission maxima (as was used in optical thermometry presented in Fig. S22 and S23). The set of characteristics for the 361 nm excitation is presented on the left side, while those for the 380 nm excitation are on the right side. In each case, the set of data includes the temperature dependences of thermometric parameters defined as depicted in the figures (top part), the resulting temperature dependences of relative thermal sensitivity (middle part), and the related temperature uncertainties (bottom part). The experimental data in the top part (colored points) were fitted to the Mott-Seitz model (see the Comment on ratiometric optical thermometry studies above). The best-fit curves are shown as colored solid lines, while the resulting best-fit parameters are gathered in Table S17. The relative thermal sensitivity and temperature uncertainties were calculated based on the corresponding *Δ*(*T*) dependences (see the Comment on ratiometric optical thermometry studies above).

Table S17 Best-fit parameters to the Mott-Seitz model for the ratiometric luminescent thermometry based on the emission spectra of **Eu_2FIr_2** under the 361 and 380 nm excitation using the ratios between the integrated areas of the indicated emission peaks (the maxima are indicated for the case of Eu(III)-based emission while the “Ir” stands for the broadband emission of Ir(III) complexes, see Fig. S24 for the related optical characteristics).

Δ	**Parameters of the Mott-Seitz Model**					**X^2**
	Δ_0	**α_1**	**α_2**	**ΔE_1 / kJ mol^{-1}**	**ΔE_2 / kJ mol^{-1}**	
λ_{em} = 361 nm						
$\frac{A_{590}}{A_{\mathrm{Ir}}}$	0.585 (±0.003)	22.874 (±2.472)	0	5.865 (±0.197)	0	0.999
$\frac{A_{617}}{A_{\mathrm{Ir}}}$	4.960 (±0.034)	158.683 (±25.114)	0	7.712 (±0.257)	0	0.999
$\frac{A_{690}}{A_{\mathrm{Ir}}}$	0.910 (±0.004)	49.889 (±3.849)	0	6.399 (±0.132)	0	0.999
$\frac{A_{617}}{A_{590}}$	8.447 (±0.076)	90.972 (±26.333)	0	8.879 (±0.556)	0	0.999
$\frac{A_{617}}{A_{690}}$	5.412 (±0.036)	329.016 (±137.559)	0	13.015 (±0.871)	0	0.999
λ_{em} = 380 nm						
$\frac{A_{590}}{A_{\mathrm{Ir}}}$	0.392 (±0.004)	25.702 (±13.130)	0	8.489 (±1.060)	0	0.999
$\frac{A_{617}}{A_{\mathrm{Ir}}}$	2.809 (±0.015)	207.149 (±32.543)	0	9.144 (±0.279)	0	0.999
$\frac{A_{690}}{A_{\mathrm{Ir}}}$	0.555 (±0.003)	89.573 (±12.544)	0	8.430 (±0.262)	0	0.999
$\frac{A_{617}}{A_{590}}$	7.525 (±0.051)	524.042 (±222.642)	1.125 (±0.347)	12.552 (±0.966)	2.127 (±0.339)	0.999
$\frac{A_{617}}{A_{690}}$	5.038 (±0.033)	45.718 (±17.408)	0	9.673 (±0.796)	0	0.999

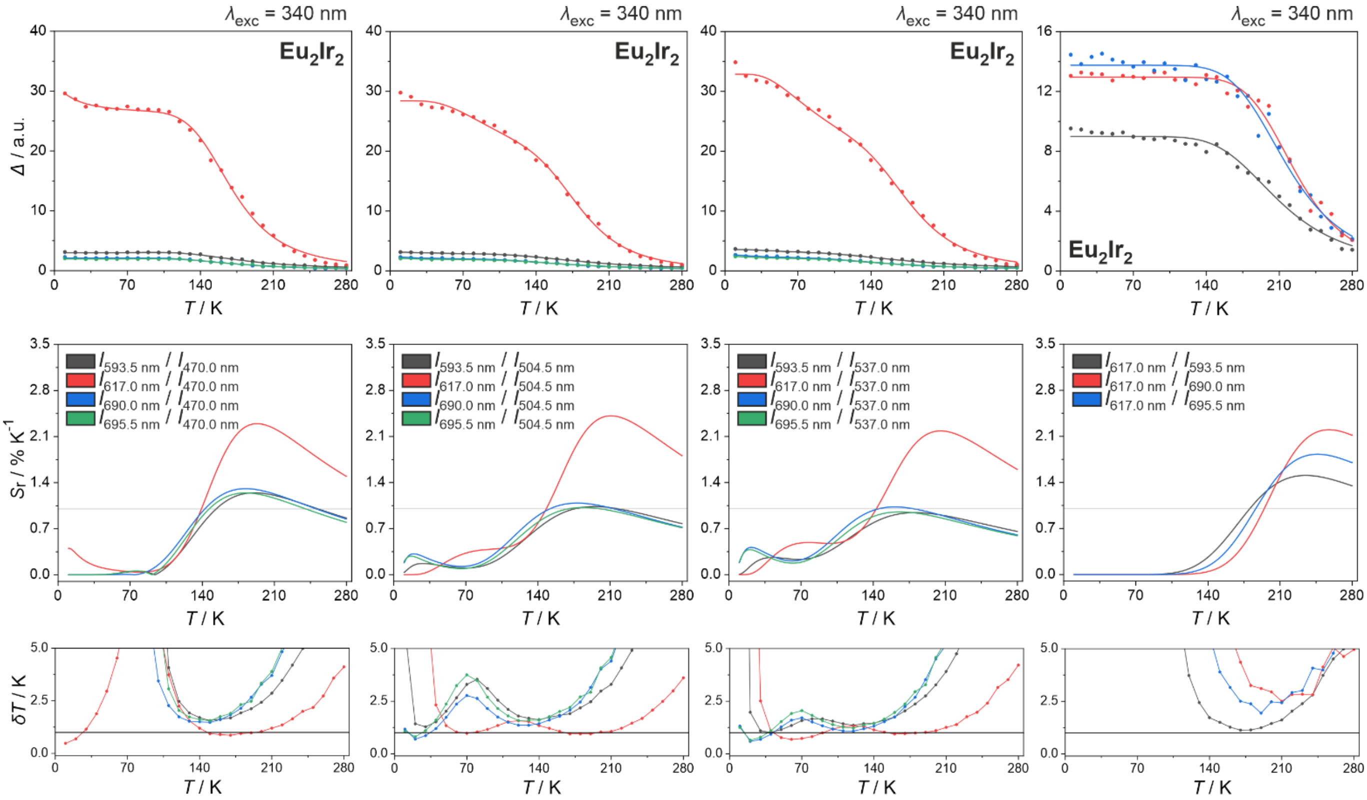

Fig. S25 The full set of the characteristics of ratiometric optical thermometry based on temperature-variable emission spectra of **Eu₂Ir₂** (the 340 nm excitation, based on the spectra presented in Fig. S17), divided into four parts (columns) representing different types of applied intensity ratios. In each case, the set of data includes the temperature dependences of thermometric parameters defined as depicted in the figures (top part), the resulting temperature dependences of relative thermal sensitivity (middle part), and the related temperature uncertainties (bottom part). The experimental data in the top part (colored points) were fitted to the Mott-Seitz model (see the Comment on ratiometric optical thermometry studies above). The best-fit curves are shown as colored solid lines, while the resulting best-fit parameters are gathered in Table S18. The relative thermal sensitivity and temperature uncertainties were calculated based on the corresponding $\Delta(T)$ dependences (see the Comment on ratiometric optical thermometry studies above).

Table S18 Best-fit parameters to the Mott-Seitz model for the ratiometric luminescent thermometry based on the emission spectra of **Eu_2Ir_2** under the 340 nm excitation (see Fig. S25 for the related optical characteristics).

Δ	**Parameters of the Mott-Seitz model**					***X*²**
	$Δ_0$	***$α_1$***	***$α_2$***	***$ΔE_1$* / kJ mol^{-1}**	***$ΔE_2$* / kJ mol^{-1}**	
$\frac{I_{593.5\ \mathrm{nm}}}{I_{470.0\ \mathrm{nm}}}$	2.998 (±0.037)	79.808 (±20.275)	-5.104 (±47.546)	6.332 (±2.782)	3.778 (±5.893)	0.999
$\frac{I_{617.0\ \mathrm{nm}}}{I_{470.0\ \mathrm{nm}}}$	30.133 (±1.502)	1582.951 (±391.728)	0.165 (±0.045)	10.341 (±0.389)	0.180 (±0.139)	0.999
$\frac{I_{690.0\ \mathrm{nm}}}{I_{470.0\ \mathrm{nm}}}$	2.117 (±0.028)	621.639 (±1711797.643)	-539.575 (±1711852.824)	5.641 (±140.436)	5.543 (±149.836)	0.999
$\frac{I_{695.5\ \mathrm{nm}}}{I_{470.0\ \mathrm{nm}}}$	1.961 (±0.026)	464.655 (±552858.577)	-405.611 (±552892.713	4.990 (±76.008)	4.868 (±79.282)	0.999
$\frac{I_{593.5\ \mathrm{nm}}}{I_{504.5\ \mathrm{nm}}}$	3.111 (±0.048)	63.794 (±9.129)	0.189 (±0.049)	6.561 (±0.272)	0.484 (±0.208)	0.999
$\frac{I_{617.0\ \mathrm{nm}}}{I_{504.5\ \mathrm{nm}}}$	28.404 (±0.283)	5050.374 (±2460.441)	1.933 (±0.586)	12.713 (±0.859)	1.879 (±0.285)	0.999
$\frac{I_{690.0\ \mathrm{nm}}}{I_{504.5\ \mathrm{nm}}}$	2.279 (±0.071)	59.395 (±11.727)	0.243 (±0.059)	5.891 (±0.352)	0.333 (±0.183)	0.999
$\frac{I_{695.5\ \mathrm{nm}}}{I_{504.5\ \mathrm{nm}}}$	2.093 (±0.076)	52.329 (±10.375)	0.185 (±0.050)	5.969 (±0.362)	0.290 (±0.214)	0.999
$\frac{I_{593.5\ \mathrm{nm}}}{I_{537.0\ \mathrm{nm}}}$	3.561 (±0.059)	44.032 (±9.047)	0.454 (±0.159)	5.741 (±0.418)	0.738 (±0.250)	0.999
$\frac{I_{617.0\ \mathrm{nm}}}{I_{537.0\ \mathrm{nm}}}$	32.866 (±0.400)	2695.763 (±1355.260)	2.003 (±0.472)	11.388 (±0.871)	1.509 (±0.206)	0.999
$\frac{I_{690.0\ \mathrm{nm}}}{I_{537.0\ \mathrm{nm}}}$	2.638 (±0.074)	40.875 (±7.431)	0.363 (±0.082)	4.987 (±0.323)	0.376 (±0.151)	0.999
$\frac{I_{695.5\ \mathrm{nm}}}{I_{537.0\ \mathrm{nm}}}$	2.424 (±0.071)	35.297 (±6.325)	0.309 (±0.072)	5.025 (±0.327)	0.351 (±0.160)	0.999
$\frac{I_{617.0\ \mathrm{nm}}}{I_{593.5\ \mathrm{nm}}}$	8.986 (±0.093)	449.707 (±163.474)	0	10.815 (±0.662)	0	0.999
$\frac{I_{617.0\ \mathrm{nm}}}{I_{690.0\ \mathrm{nm}}}$	12.960 (±0.118)	6045.303 (±3234.875)	0	16.413 (±1.026)	0	0.999
$\frac{I_{617.0\ \mathrm{nm}}}{I_{695.5\ \mathrm{nm}}}$	13.752 (±0.155)	1504.578 (±765.160)	0	13.326 (±0.947)	0	0.999

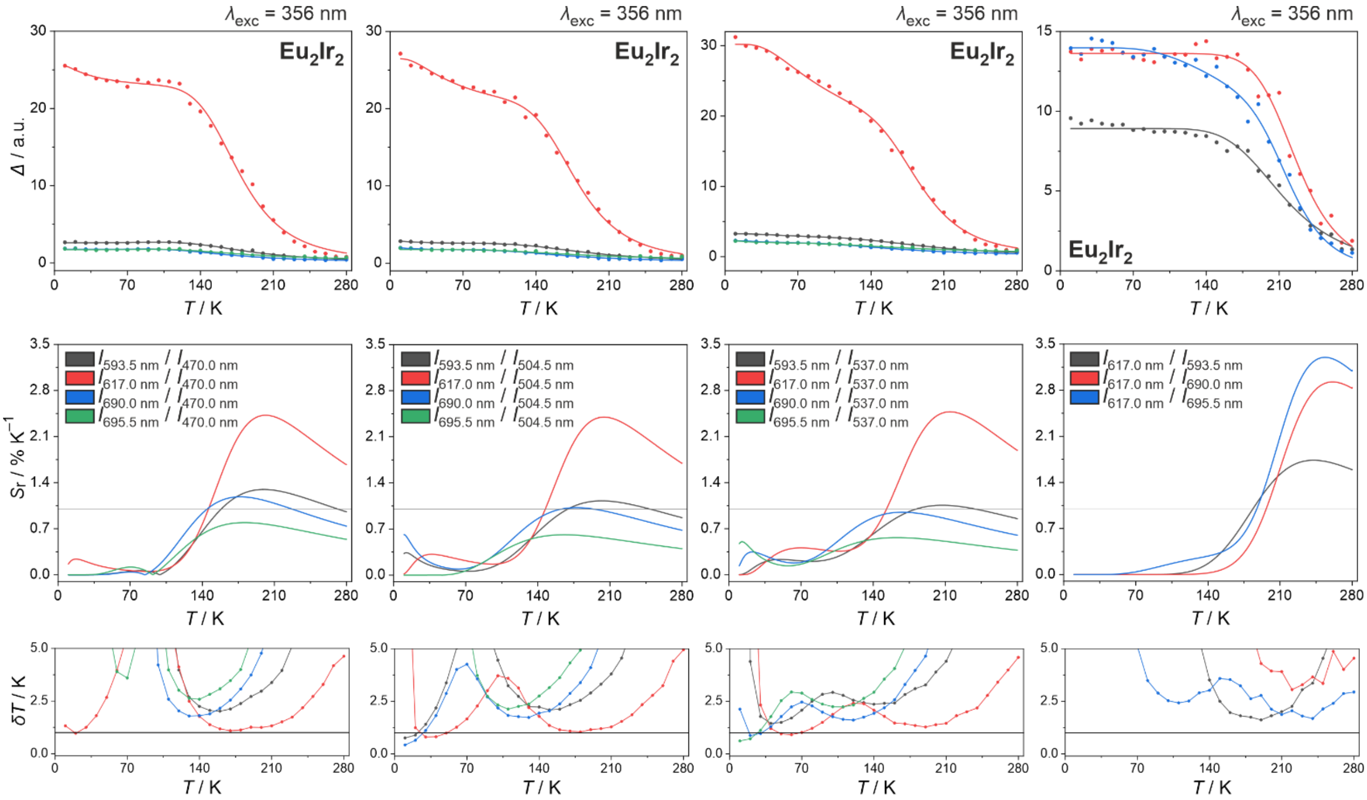

Fig. S26 The full set of the characteristics of ratiometric optical thermometry based on temperature-variable emission spectra of **Eu_2Ir_2** (the 356 nm excitation, based on the spectra presented in Fig. S17), divided into four parts (columns) representing different types of applied intensity ratios. In each case, the set of data includes the temperature dependences of thermometric parameters defined as depicted in the figures (top part), the resulting temperature dependences of relative thermal sensitivity (middle part), and the related temperature uncertainties (bottom part). The experimental data in the top part (colored points) were fitted to the Mott-Seitz model (see the Comment on ratiometric optical thermometry studies above). The best-fit curves are shown as colored solid lines, while the resulting best-fit parameters are gathered in Table S19. The relative thermal sensitivity and temperature uncertainties were calculated based on the corresponding $\Delta(T)$ dependences (see the Comment on ratiometric optical thermometry studies above).

Table S19 Best-fit parameters to the Mott-Seitz model for the ratiometric luminescent thermometry based on the emission spectra of **Eu_2Ir_2** under the 356 nm excitation (see Fig. S26 for the related optical characteristics).

Δ	**Parameters of the Mott-Seitz model**					***X*²**
	$Δ_0$	***$α_1$***	***$α_2$***	***$ΔE_1$* / kJ mol^{-1}**	***$ΔE_2$* / kJ mol^{-1}**	
$\frac{I_{593.5\ \mathrm{nm}}}{I_{470.0\ \mathrm{nm}}}$	2.619 (±0.034)	107.671 (±47.303)	-1.372 (±6.689)	7.288 (±1.454)	2.969 (±3.854)	0.999
$\frac{I_{617.0\ \mathrm{nm}}}{I_{470.0\ \mathrm{nm}}}$	25.652 (±0.884)	2701.136 (±996.581)	0.161 (±0.041)	11.543 (±0.591)	0.296 (±0.215)	0.999
$\frac{I_{690.0\ \mathrm{nm}}}{I_{470.0\ \mathrm{nm}}}$	1.768 (±0.031)	473.794 (±1117368.576)	-425.002 (±1117399.687)	4.731 (±109.600)	4.641 (±113.551)	0.999
$\frac{I_{695.5\ \mathrm{nm}}}{I_{470.0\ \mathrm{nm}}}$	1.713 (±0.039)	225.439 (±377905.433)	-209.372 (±377910.395)	3.652 (±62.072)	3.580 (±62.977)	0.999
$\frac{I_{593.5\ \mathrm{nm}}}{I_{504.5\ \mathrm{nm}}}$	2.880 (±0.157)	93.652 (±21.291)	0.162 (±0.050)	7.206 (±0.419)	0.209 (±0.204)	0.999
$\frac{I_{617.0\ \mathrm{nm}}}{I_{504.5\ \mathrm{nm}}}$	26.458 (±0.421)	3224.793 (±1103.008)	0.483 (±0.074)	11.776 (±0.561)	0.650 (±0.139)	0.999
$\frac{I_{690.0\ \mathrm{nm}}}{I_{504.5\ \mathrm{nm}}}$	2.048 (±0.224)	50.042 (±12.975)	0.240 (±0.100)	5.660 (±0.463)	0.170 (±0.207)	0.999
$\frac{I_{695.5\ \mathrm{nm}}}{I_{504.5\ \mathrm{nm}}}$	1.763 (±0.049)	63.523 (±390470.312)	-53.681 (±390479.530)	3.643 (±235.303)	3.569 (±259.647)	0.999
$\frac{I_{593.5\ \mathrm{nm}}}{I_{537.0\ \mathrm{nm}}}$	3.248 (±0.042)	92.597 (±20.836)	0.481 (±0.136)	7.380 (±0.456)	0.876 (±0.233)	0.999
$\frac{I_{617.0\ \mathrm{nm}}}{I_{537.0\ \mathrm{nm}}}$	30.197 (±0.335)	6631.072 (±3049.704)	1.404 (±0.249)	13.242 (±0.796)	1.327 (±0.166)	0.999
$\frac{I_{690.0\ \mathrm{nm}}}{I_{537.0\ \mathrm{nm}}}$	2.295 (±0.068)	36.255 (±7.354)	0.314 (±0.087)	5.132 (±0.375)	0.391 (±0.191)	0.999
$\frac{I_{695.5\ \mathrm{nm}}}{I_{537.0\ \mathrm{nm}}}$	2.294 (±0.181)	10.402 (±2.586)	0.253 (±0.081)	4.044 (±0.525)	0.219 (±0.232)	0.999
$\frac{I_{617.0\ \mathrm{nm}}}{I_{593.5\ \mathrm{nm}}}$	8.916 (±0.090)	1049.507 (±444.735)	0	12.523 (±0.782)	0	0.999
$\frac{I_{617.0\ \mathrm{nm}}}{I_{690.0\ \mathrm{nm}}}$	13.619 (±0.164)	74074.049 (±616837.494)	379.493 (±30065.134)	21.575 (±29.506)	14.234 (±94.415)	0.999
$\frac{I_{617.0\ \mathrm{nm}}}{I_{695.5\ \mathrm{nm}}}$	13.970 (±0.176	207419.808 (±297312.832)	3.614 (±3.583)	22.183 (±2.891)	3.909 (±1.263)	0.999

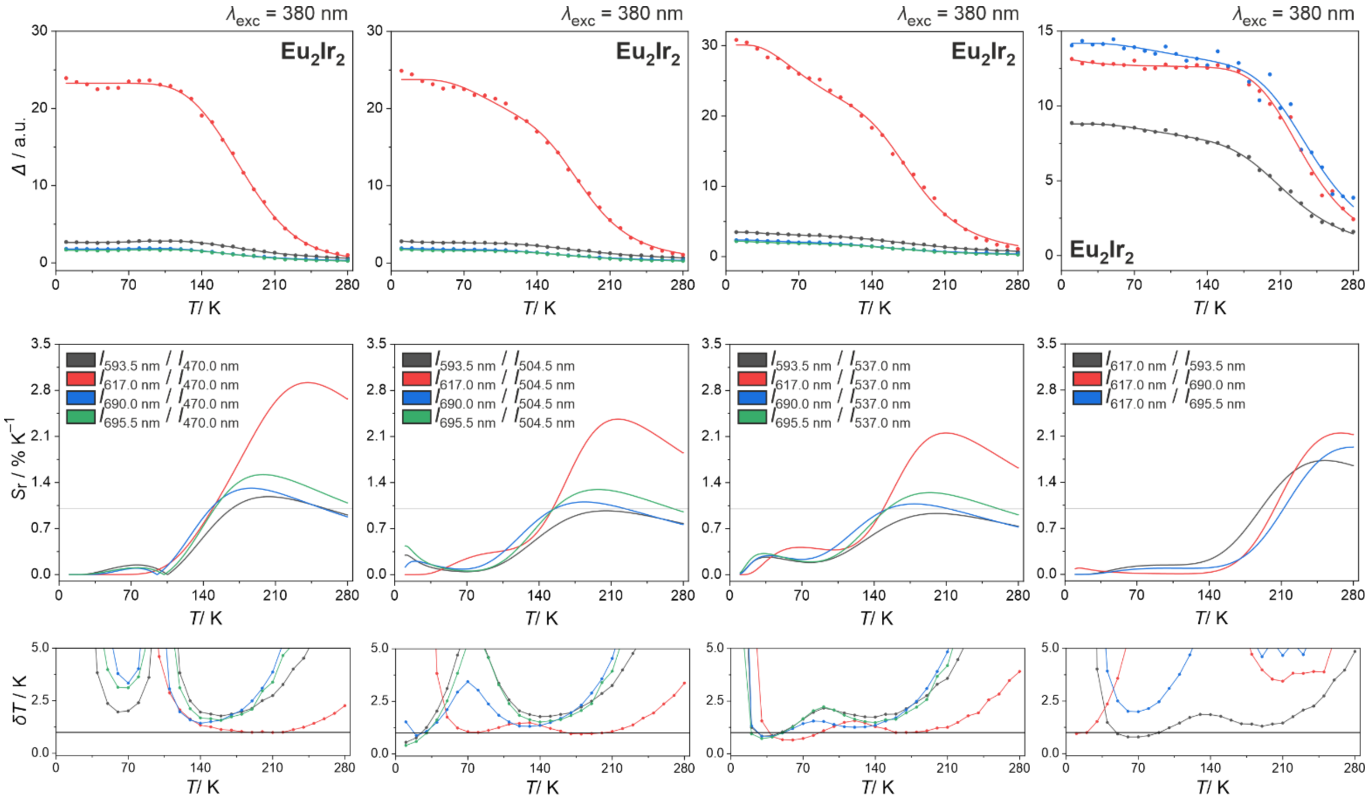

Fig. S27 The full set of the characteristics of ratiometric optical thermometry based on temperature-variable emission spectra of **Eu$_2$Ir$_2$** (the 380 nm excitation, based on the spectra presented in Fig. S17), divided into four parts (columns) representing different types of applied intensity ratios. In each case, the set of data includes the temperature dependences of thermometric parameters defined as depicted in the figures (top part), the resulting temperature dependences of relative thermal sensitivity (middle part), and the related temperature uncertainties (bottom part). The experimental data in the top part (colored points) were fitted to the Mott-Seitz model (see the Comment on ratiometric optical thermometry studies above). The best-fit curves are shown as colored solid lines, while the resulting best-fit parameters are gathered in Table S20. The relative thermal sensitivity and temperature uncertainties were calculated based on the corresponding $\Delta(T)$ dependences (see the Comment on ratiometric optical thermometry studies above).

Table S20 Best-fit parameters to the Mott-Seitz model for the ratiometric luminescent thermometry based on the emission spectra of **Eu_2Ir_2** under the 380 nm excitation (see Fig. S27 for the related optical characteristics).

Δ	**Parameters of the Mott-Seitz model**					***X*²**
	Δ_0	***α_1***	***α_2***	***ΔE_1* / kJ mol^{-1}**	***ΔE_2* / kJ mol^{-1}**	
$\frac{I_{593.5\ \mathrm{nm}}}{I_{470.0\ \mathrm{nm}}}$	2.631 (±0.028)	78.592 (±17.250)	-0.653 (±0.568)	7.160 (±0.533)	1.716 (±0.729)	0.999
$\frac{I_{617.0\ \mathrm{nm}}}{I_{470.0\ \mathrm{nm}}}$	23.254 (±0.119)	153117.710 (±273641.032)	191.355 (±150.326)	20.649 (±3.880)	8.143 (±0.941)	0.999
$\frac{I_{690.0\ \mathrm{nm}}}{I_{470.0\ \mathrm{nm}}}$	1.790 (±0.021)	-1.504 (±4.521)	85.156 (±25.993)	2.601 (±2.213)	6.522 (±1.014)	0.999
$\frac{I_{695.5\ \mathrm{nm}}}{I_{470.0\ \mathrm{nm}}}$	1.630 (±0.025)	-0.524 (±0.921)	190.846 (±68.364)	1.821 (±1.511)	8.074 (±0.767)	0.999
$\frac{I_{593.5\ \mathrm{nm}}}{I_{504.5\ \mathrm{nm}}}$	2.856 (±0.105)	60.027 (±7.483)	0.126 (±0.032)	6.823 (±0.238)	0.187 (±0.145)	0.999
$\frac{I_{617.0\ \mathrm{nm}}}{I_{504.5\ \mathrm{nm}}}$	23.765 (±0.225)	5114.209 (±2590.357)	2.073 (±0.798)	13.151 (±0.928)	2.192 (±0.377)	0.999
$\frac{I_{690.0\ \mathrm{nm}}}{I_{504.5\ \mathrm{nm}}}$	1.911 (±0.049)	64.646 (±10.701)	0.156 (±0.045)	6.208 (±0.298)	0.335 (±0.226)	0.999
$\frac{I_{695.5\ \mathrm{nm}}}{I_{504.5\ \mathrm{nm}}}$	1.808 (±0.117)	141.950 (±31.408)	0.181 (±0.059)	7.506 (±0.392)	0.182 (±0.173)	0.999
$\frac{I_{593.5\ \mathrm{nm}}}{I_{537.0\ \mathrm{nm}}}$	3.480 (±0.044)	57.107 (±9.279)	0.398 (±0.073)	6.613 (±0.326)	6.613 (±0.326)	0.999
$\frac{I_{617.0\ \mathrm{nm}}}{I_{537.0\ \mathrm{nm}}}$	30.097 (±0.328)	2542.574 (±992.214)	1.396 (±0.257)	11.591 (±0.681)	11.591 (±0.681)	0.999
$\frac{I_{690.0\ \mathrm{nm}}}{I_{537.0\ \mathrm{nm}}}$	2.364 (±0.038)	63.061 (±12.017)	0.459 (±0.126)	5.998 (±0.363)	5.998 (±0.363)	0.999
$\frac{I_{695.5\ \mathrm{nm}}}{I_{537.0\ \mathrm{nm}}}$	2.177 (±0.041)	131.869 (±30.743)	0.436 (±0.091)	7.255 (±0.424)	7.255 (±0.424)	0.999
$\frac{I_{617.0\ \mathrm{nm}}}{I_{593.5\ \mathrm{nm}}}$	8.798 (±0.068)	1588.237 (±510.715)	0.557 (±0.192)	13.507 (±0.666)	1.670 (±0.380)	0.999
$\frac{I_{617.0\ \mathrm{nm}}}{I_{690.0\ \mathrm{nm}}}$	13.132 (±0.531)	0.050 (±0.036)	6985.147 (±3202.734)	0.233 (±0.488)	17.260 (±0.925)	0.999
$\frac{I_{617.0\ \mathrm{nm}}}{I_{695.5\ \mathrm{nm}}}$	14.196 (±0.276)	0.370 (±0.364)	5084.506 (±5409.476)	1.708 (±1.232)	17.190 (±2.289)	0.999

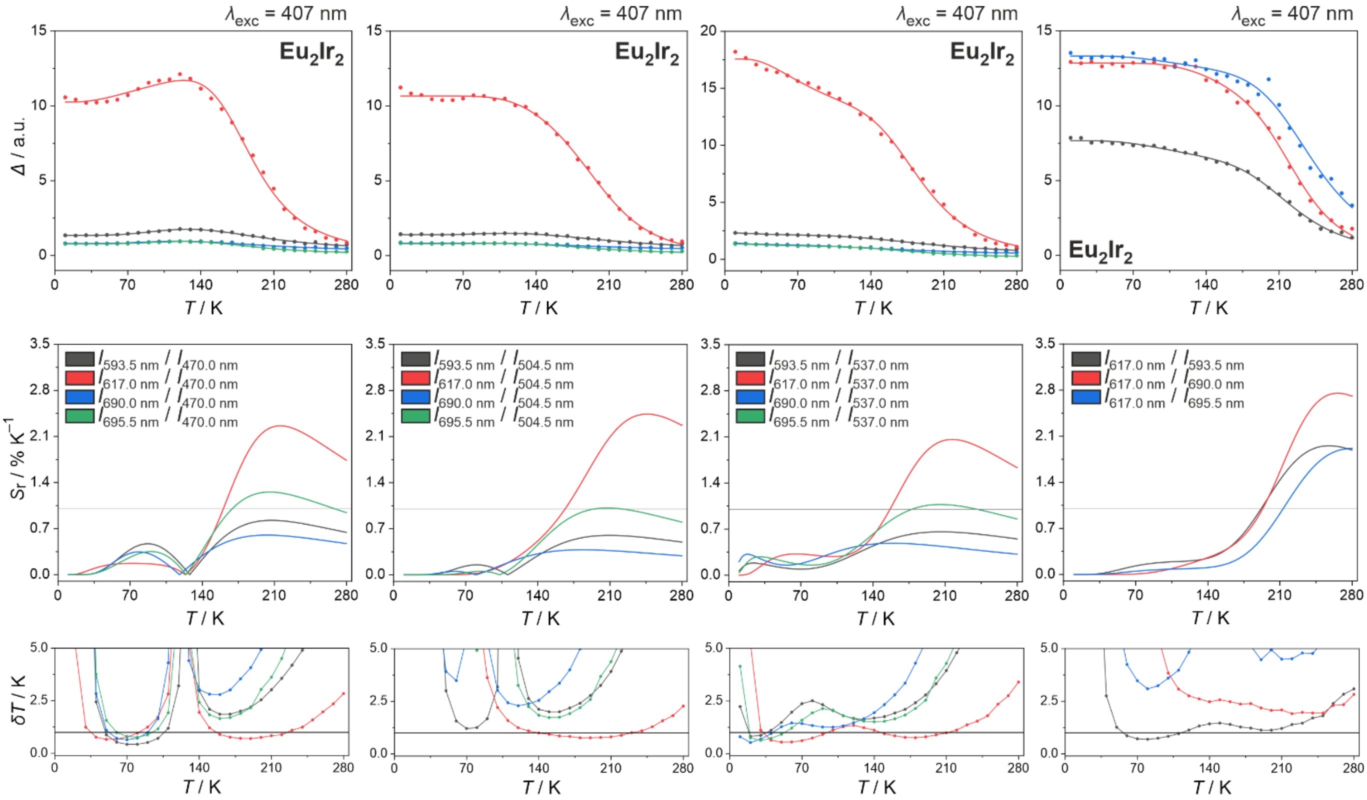

Fig. S28 The full set of the characteristics of ratiometric optical thermometry based on temperature-variable emission spectra of **Eu_2Ir_2** (the 407 nm excitation, based on the spectra presented in Fig. S17), divided into four parts (columns) representing different types of applied intensity ratios. In each case, the set of data includes the temperature dependences of thermometric parameters defined as depicted in the figures (top part), the resulting temperature dependences of relative thermal sensitivity (middle part), and the related temperature uncertainties (bottom part). The experimental data in the top part (colored points) were fitted to the Mott-Seitz model (see the Comment on ratiometric optical thermometry studies above). The best-fit curves are shown as colored solid lines, while the resulting best-fit parameters are gathered in Table S21. The relative thermal sensitivity and temperature uncertainties were calculated based on the corresponding $\Delta(T)$ dependences (see the Comment on ratiometric optical thermometry studies above).

Table S21 Best-fit parameters to the Mott-Seitz model for the ratiometric luminescent thermometry based on the emission spectra of **Eu_2Ir_2** under the 407 nm excitation (see Fig. S28 for the related optical characteristics).

Δ	**Parameters of the Mott-Seitz model**					***X^2***
	$Δ_0$	***$α_1$***	***$α_2$***	**$ΔE_1$ / kJ mol^{-1}**	**$ΔE_2$ / kJ mol^{-1}**	
$\frac{I_{593.5\ \mathrm{nm}}}{I_{470.0\ \mathrm{nm}}}$	1.348 (±0.022)	22.428 (±16.083)	-7.370 (±19.940)	4.384 (±1.709)	2.678 (±1.386)	0.999
$\frac{I_{617.0\ \mathrm{nm}}}{I_{470.0\ \mathrm{nm}}}$	10.261 (±0.161)	1858.638 (±624.546)	-0.408 (±0.146)	12.220 (±0.608)	1.128 (±0.379)	0.999
$\frac{I_{690.0\ \mathrm{nm}}}{I_{470.0\ \mathrm{nm}}}$	0.797 (±0.018)	168.663 (±103022.521)	-160.606 (±103023.456)	3.119 (±22.061)	3.048 (±21.998)	0.999
$\frac{I_{695.5\ \mathrm{nm}}}{I_{470.0\ \mathrm{nm}}}$	0.775 (±0.011)	-2.576 (±2.320)	69.136 (±19.826)	2.347 (±0.734)	6.848 (±0.904)	0.999
$\frac{I_{593.5\ \mathrm{nm}}}{I_{504.5\ \mathrm{nm}}}$	1.394 (±0.019)	-118.233 (±94118.225)	129.289 (±94113.789)	3.670 (±41.783)	3.780 (±41.647)	0.999
$\frac{I_{617.0\ \mathrm{nm}}}{I_{504.5\ \mathrm{nm}}}$	10.661 (±0.063)	23357.230 (±29260.433)	40.809 (±42.762)	17.879 (±2.860)	6.703 (±1.239)	0.999
$\frac{I_{690.0\ \mathrm{nm}}}{I_{504.5\ \mathrm{nm}}}$	0.828 (±0.017)	62.853 (±126767.491)	-58.492 (±126768.810)	2.971 (±64.053)	2.909 (±65.221)	0.999
$\frac{I_{695.5\ \mathrm{nm}}}{I_{504.5\ \mathrm{nm}}}$	0.800 (±0.010)	478.064 (±676079.729)	-430.522 (±676104.110)	5.437 (±78.377)	5.331 (±80.375)	0.999
$\frac{I_{593.5\ \mathrm{nm}}}{I_{537.0\ \mathrm{nm}}}$	2.311 (±0.052)	21.983 (±4.288)	0.170 (±0.052)	5.808 (±0.412)	0.407 (±0.247)	0.999
$\frac{I_{617.0\ \mathrm{nm}}}{I_{537.0\ \mathrm{nm}}}$	17.567 (±0.192)	2147.502 (±749.888)	0.954 (±0.184)	11.835 (±0.626)	1.197 (±0.180)	0.999
$\frac{I_{690.0\ \mathrm{nm}}}{I_{537.0\ \mathrm{nm}}}$	1.417 (±0.059)	7.233 (±1.552)	0.226 (±0.087)	3.778 (±0.489)	0.312 (±0.260)	0.999
$\frac{I_{695.5\ \mathrm{nm}}}{I_{537.0\ \mathrm{nm}}}$	1.348 (±0.025)	91.889 (±20.139)	0.342 (±0.070)	7.258 (±0.419)	0.528 (±0.168)	0.999
$\frac{I_{617.0\ \mathrm{nm}}}{I_{593.5\ \mathrm{nm}}}$	7.661 (±0.058)	3945.404 (±1729.221)	1.059 (±0.371)	15.299 (±0.916)	2.183 (±0.403)	0.999
$\frac{I_{617.0\ \mathrm{nm}}}{I_{690.0\ \mathrm{nm}}}$	12.858 (±0.089)	10.662 (±11.050)	72582.659 (±83637.435)	5.772 (±1.362)	21.292 (±2.551)	0.999
$\frac{I_{617.0\ \mathrm{nm}}}{I_{695.5\ \mathrm{nm}}}$	13.332 (±0.178)	4896.490 (±4488.315)	0.482 (±0.588)	17.221 (±2.018)	2.346 (±1.540)	0.999

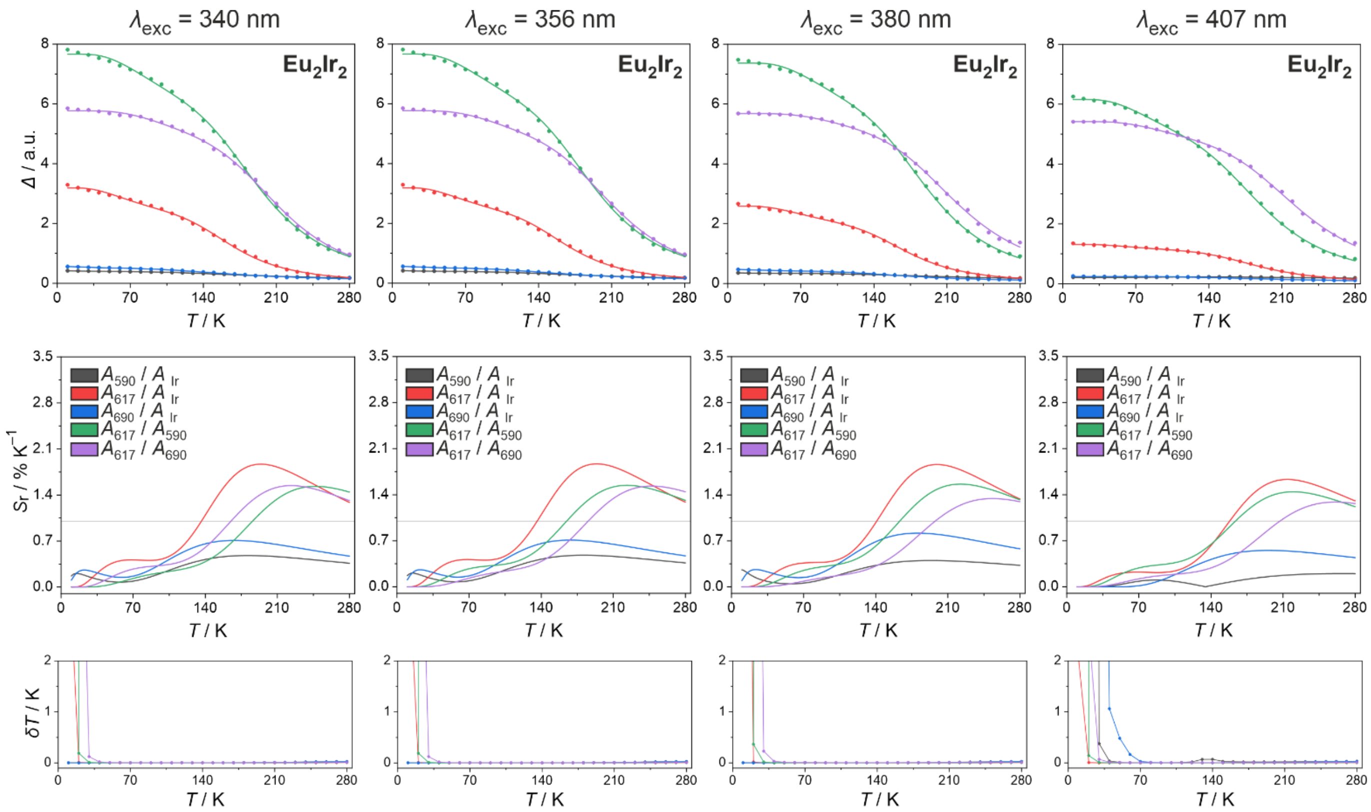

Fig. S29 The full set of the characteristics of ratiometric optical thermometry based on temperature-variable emission spectra of **Eu_2Ir_2** using the ratios between the integrated areas of the indicated emission peaks (the maxima are indicated for the case of Eu(III)-based emission while the "Ir" stands for the broadband emission of Ir(III) complexes, the respective emission spectra are shown in Fig. S17) instead of the ratios between the intensities for the selected emission maxima (as was used in optical thermometry presented in Fig. S25–S28). The set of characteristics for four different indicated excitation wavelengths are presented. In each case, the set of data includes the temperature dependences of thermometric parameters defined as depicted in the figures (top part), the resulting temperature dependences of relative thermal sensitivity (middle part), and the related temperature uncertainties (bottom part). The experimental data in the top part (colored points) were fitted to the Mott-Seitz model (see the Comment on ratiometric optical thermometry studies above). The best-fit curves are shown as colored solid lines, while the resulting best-fit parameters are gathered in Table S22. The relative thermal sensitivity and temperature uncertainties were calculated based on the corresponding $\Delta(T)$ dependences (see the Comment on ratiometric optical thermometry studies above).

Table S22 Best-fit parameters to the Mott-Seitz model for the ratiometric luminescent thermometry based on the emission spectra of **Eu$_2$Ir$_2$** under the 340, 356, 308, and 407 nm excitation using the ratios between the integrated areas of the indicated emission peaks (the maxima are indicated for the case of Eu(III)-based emission while the "Ir" stands for the broadband emission of Ir(III) complexes, see Fig. S29 for the related optical characteristics).

Δ	Parameter of the Mott-Seitz model					X^2
	Δ_0	α_1	α_2	ΔE_1 / kJ mol^{-1}	ΔE_2 / kJ mol^{-1}	
λ_{em} = 340 nm						
$\frac{A_{590}}{A_{Ir}}$	0.424 (±0.007)	8.442 (±0.614)	0.121 (±0.019)	4.379 (±0.161)	0.258 (±0.120)	0.999
$\frac{A_{617}}{A_{Ir}}$	3.191 (±0.027)	809.894 (±201.861)	1.351 (±0.242)	9.333 (±0.432)	1.271 (±0.146)	0.999
$\frac{A_{690}}{A_{Ir}}$	0.564 (±0.010)	17.015 (±1.850)	0.228 (±0.049)	4.555 (±0.223)	0.385 (±0.146)	0.999
$\frac{A_{617}}{A_{590}}$	7.663 (±0.037)	618.916 (±117.415)	1.479 (±0.250)	10.477 (±0.384)	1.815 (±0.158)	0.999
$\frac{A_{617}}{A_{690}}$	5.769 (±0.023)	901.791 (±209.325)	1.627 (±0.405)	12.284 (±0.509)	2.511 (±0.262)	0.999
λ_{em} = 356nm						
$\frac{A_{590}}{A_{Ir}}$	0.424 (±0.007)	8.442 (±0.614)	0.121 (±0.019)	4.379 (±0.161)	0.258 (±0.120)	0.999
$\frac{A_{617}}{A_{Ir}}$	3.191 (±0.027)	809.894 (±201.861)	1.351 (±0.242)	9.333 (±0.432)	1.271 (±0.146)	0.999
$\frac{A_{690}}{A_{Ir}}$	0.564 (±0.010)	17.015 (±1.850)	0.228 (±0.049)	4.555 (±0.223)	0.385 (±0.146)	0.999
$\frac{A_{617}}{A_{590}}$	7.663 (±0.037)	618.916 (±117.415)	1.479 (±0.250)	10.477 (±0.384)	1.815 (±0.158)	0.999
$\frac{A_{617}}{A_{690}}$	5.769 (±0.023)	901.791 (±209.325)	1.627 (±0.405)	12.284 (±0.509)	2.511 (±0.262)	0.999
λ_{em} = 380 nm						
$\frac{A_{590}}{A_{Ir}}$	0.362 (±0.010)	6.746 (±0.466)	0.095 (±0.022)	4.496 (±0.158)	0.163 (±0.117)	0.999
$\frac{A_{617}}{A_{Ir}}$	2.587 (±0.020)	876.023 (±211.509)	1.344 (±0.266)	9.744 (±0.431)	1.432 (±0.168)	0.999
$\frac{A_{690}}{A_{Ir}}$	0.469 (±0.006)	28.268 (±2.589)	0.243 (±0.035)	5.305 (±0.180)	0.403 (±0.104)	0.999
$\frac{A_{617}}{A_{590}}$	7.371 (±0.028)	639.621 (±103.940)	1.605 (±0.258)	10.509 (±0.332)	1.969 (±0.151)	0.999
$\frac{A_{617}}{A_{690}}$	5.679 (±0.024)	506.152 (±131.583)	1.262 (±0.497)	11.741 (±0.602)	2.642 (±0.417)	0.999
λ_{em} = 407 nm						
$\frac{A_{590}}{A_{Ir}}$	0.210 (±0.001)	48.747 (±29298.661)	-46.268 (±29299.172)	3.441 (±27.031)	3.354 (±26.756)	0.999
$\frac{A_{617}}{A_{Ir}}$	1.313 (±0.008)	562.531 (±88.575)	0.644 (±0.109)	9.946 (±0.297)	1.209 (±0.153)	0.999
$\frac{A_{690}}{A_{Ir}}$	0.236 (±0.003)	85.474 (±249594.059)	-74.206 (±249598.552)	4.417 (±109.040)	4.344 (±117.940)	0.999
$\frac{A_{617}}{A_{590}}$	6.159 (±0.024)	437.770 (±65.853)	1.517 (±0.215)	9.855 (±0.308)	1.795 (±0.129)	0.999
$\frac{A_{617}}{A_{690}}$	5.419 (±0.019)	487.155 (±96.152)	1.052 (±0.224)	11.955 (±0.448)	2.239 (±0.228)	0.999

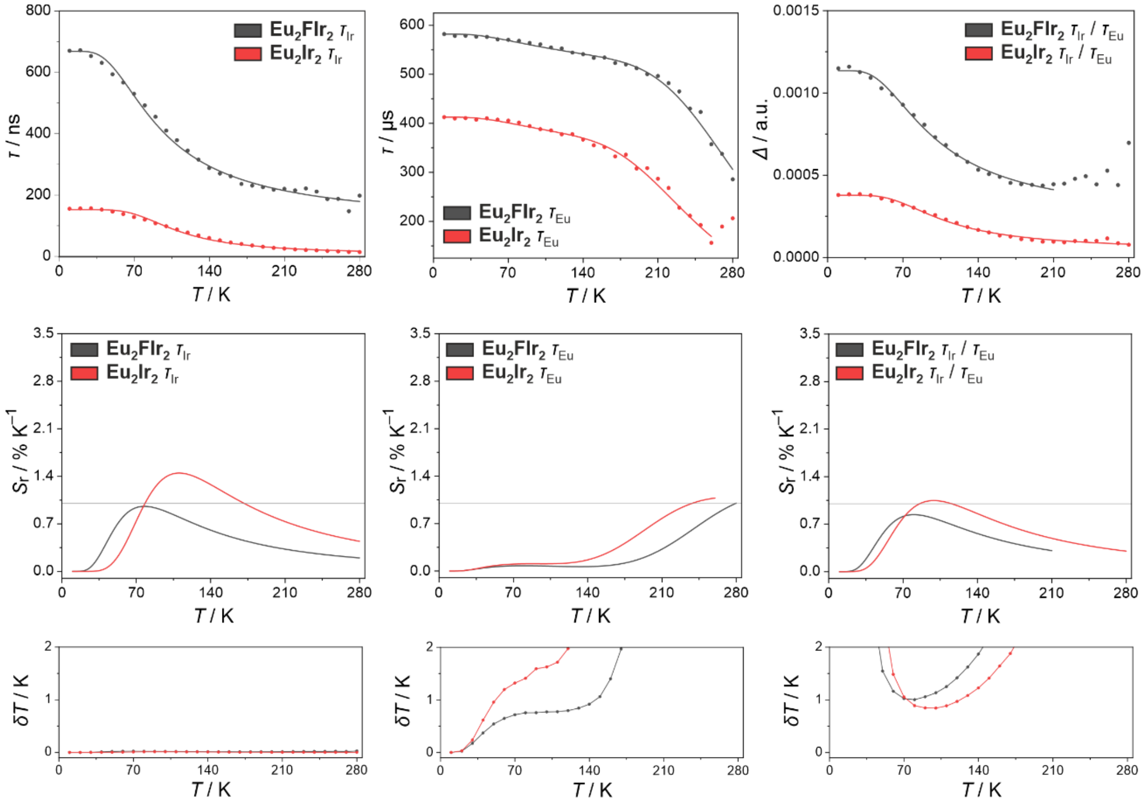

Fig. S30 The full set of the characteristics of optical thermometry based on temperature-variable emission lifetimes in **Eu_2FIr_2** and **Eu_2Ir_2**, including the emission lifetime for the Ir(III)-based emission (left column; the 374 nm excitation and the 460 nm emission, as shown in Fig. S16 for **Eu_2FIr_2**; the 374 nm excitation and the 470 nm emission, as shown in Fig. S20 for **Eu_2Ir_2**), the emission lifetime for the Eu(III)-based emission (middle column; the 361 nm excitation and the 617 nm emission, as shown in Fig. S15 for **Eu_2FIr_2**; the 356 nm excitation and the 617 nm emission, as shown in Fig. S19 for **Eu_2Ir_2**), and the ratio between the mentioned emission lifetimes (right column). In each case, the set of data includes the temperature dependences of thermometric parameters defined as depicted in the figures (top part), the resulting temperature dependences of relative thermal sensitivity (middle part), and the related temperature uncertainties (bottom part). The experimental data in the top part (colored points) were fitted to the Mott-Seitz model (see the Comment on ratiometric optical thermometry studies above). The best-fit curves are shown as colored solid lines, while the resulting best-fit parameters are gathered in Table S23. The relative thermal sensitivity and temperature uncertainties were calculated based on the corresponding $\Delta(T)$ dependences (see the Comment on ratiometric optical thermometry studies above).

Table S23 Best-fit parameters to the Mott-Seitz model for the luminescent thermometry based on the emission lifetimes of **Eu_2FIr_2** and **Eu_2Ir_2**, including the emission lifetime of the Ir(III)-based emission (τ_{Ir}), the emission lifetime of the Eu(III)-based emission (τ_{Eu}), and their ratio (see Fig. S30 for the related optical characteristics).

Compound and *Δ*	**Parameters of the Mott-Seitz model**					**X^2**
	Δ_0	**α_1**	**α_2**	**ΔE_1 / kJ mol^{-1}**	**ΔE_2 / kJ mol^{-1}**	
Eu_2FIr_2 τ_{Ir}	667.222 (±6.531) [ns]	5.802 (±0.389)	0	1.775 (±0.107)	0	0.997
Eu_2Ir_2 τ_{Ir}	153.470 (±1.514) [ns]	29.175 (±2.946)	0	3.301 (±0.128)	0	0.999
Eu_2FIr_2 τ_{Eu}	582.139 (±0.009) [ms]	711.277 (±635.956)	0.239 (±0.034)	15.896 (±1.882)	1.359 (±0.132)	0.999
Eu_2Ir_2 τ_{Eu}	412.632 (±0.009) [ms]	261.021 (±181.313)	0.361 (±0.086)	11.537 (±1.360)	1.462 (±0.186)	0.990
Eu_2FIr_2 $\frac{\tau_{Ir}}{\tau_{Eu}}$	0.00113 (±0.000009)	4.875 (±0.269)	0	1.782 (±0.065)	0	0.999
Eu_2Ir_2 $\frac{\tau_{Ir}}{\tau_{Eu}}$	0.000378 (±0.000005)	10.781 (±0.867)	0	2.497 (±0.104)	0	0.999

Computational details

In this work, the theoretical calculations were performed for the $[\mathrm{Ir^{III}(CN)_2}(R,R\text{-Fpinppy})_2]^-$ complexes that are present in the crystal structures of ***R*,*R*-FIr** and **Eu$_2$FIr$_2$** while the analogous theoretical studies for the $[\mathrm{Ir^{III}(CN)_2}(R,R\text{-Fpinppy})_2]^-$ complexes, which are present in the crystal structures of ***R*,*R*-Ir** and **Eu$_2$Ir$_2$**, were performed and discussed within the previously published article on relative materials.[S1] The calculations discussed here were performed using the ORCA 5.0.3 quantum chemistry software package,[S17] while their results were visualized in VESTA software.[S18] Initially, the geometry of this anionic metal complex, comprising an Ir(III) center along with the surrounding of *R*,*R*-Fpinppy and cyanido ligands, obtained from the SC-XRD experiment, was optimized using a DFT method employing the B3LYP hybrid exchange-correlation functional as it has demonstrated reasonable performance in our previous study on the mentioned analogs.[S1] In our computational approach, we entirely excluded the counterions present in the crystal structure as well as solvent molecules. We used the def2-TZVP basis set in conjunction with the charge-dependent atom-pairwise dispersion correction based on the D4(EEQ)-ATM model.[S19,S20] For the calculations, the LR-CPCM solvation model was employed using water as the solvent.[S21] A comparison between the geometry of the investigated Ir(III) complex obtained from the SC-XRD studies and its optimized geometry for the ground electronic state is shown in Fig. S31, while selected parameters for these two geometries are compared in Table S24. The optimized geometry displays overall good agreement with the experimental one, with deviations of approximately 0.02 Å for bond lengths, but, unfortunately, differences in the angles are more pronounced and reach a maximum of 4.8 degrees. They mainly result from the gas-phase optimization, which, as opposed to including the whole crystal structure, imposes certain constraints on the geometry. This might result in some inconsistencies between the computed results of optical properties and the experimental spectroscopic data.

The restricted Kohn-Sham determinant of the ground state was then used as the reference for the subsequent SOC TD-DFT calculations. To simulate the UV-vis absorption spectra, singlet excited states were optimized using TD-DFT and subsequently mixed with calculated triplet excited states, based on the optimized ground-state geometry from the previous step. Scalar relativistic effects were incorporated using the zeroth-order regular approximation (ZORA),[S22,S23] along with a compatible segmented all-electron relativistically contracted basis set SARC-ZORA-TZVP, employing the SARC/J general-purpose Coulomb fitting.[S24,S25] To speed up the computation of two-electron integrals, the chain-of-spheres algorithm for the exchange part (COSX) was employed alongside the resolution-of-identity approximation for the Coulomb part (RIJ).[S26,S27] Spin-orbit integrals were computed using the RI-SOMF(1X) approximation, which involves using a mean-field potential with the inclusion of one-electron terms, the Coulomb term calculated using the RI approximation, and exchange terms evaluated via one-center exact integrals, including spin-other-orbit interactions, while omitting DFT local correlation terms.[S28] The maximum number of centers included in the integrals was limited to four. The lowest-energy states obtained at the TD-DFT stage for the ground state geometry are gathered in Table S25. Moreover, the list of the first 30 excited singlet states (based on the ground-state geometry optimized in the previous step) is provided in Table S26, along with the SOC states obtained by mixing singlets and triplets using the calculated spin-orbit coupling. The theoretical UV-vis absorption spectra, shown in Fig. S34, were simulated using the orca_mapspc tool, applying a broadening of 1800 $\mathrm{cm^{-1}}$ for both singlets only (TD-DFT) and spin-orbit-corrected states (SOC), and compared with the experimental spectrum. The pertinent molecular orbitals contributing most significantly to the first five singlet and triplet states (Table S25) are depicted in Fig. S32. To gain a better understanding of the light absorption mechanism (and subsequent emission from those levels), difference density maps for the first nine excited spin-orbit states were plotted in Fig. S33. Upon inspection, it is evident that the transitions are predominantly of a metal-to-ligand charge transfer (MLCT) character, with a slight contribution from the cyanido-to-*R*,*R*-Fpinppy (ligand-to-ligand) charge transfer mechanisms.

In the final step, to elucidate the observed luminescence, we performed the geometry optimization of the first excited spin-orbit state, leveraging ORCA's capability to calculate gradients for mixed states. Following optimization, we presented several relevant SOC-corrected states for the new geometry in Tables S27 and S28, along with the related molecular orbitals in Fig. S36, while the optimized geometry for the excited state is visualized in Fig. S31b. From the calculated density electron difference maps, it can be inferred that the primary mechanism of the observed phosphorescence is from the MLCT-type excited state, where the related CT transition involves the *R*,*R*-Fpinppy ligands and Ir(III) centers, with a slight contribution from cyanido units and the admixture of intra-ligand (*R*,*R*-Fpinppy) electronic transitions (Fig. S36). The energies obtained for the spin-orbit states were compared with the emission spectra of ***R*,*R*-FIr** (Fig. S37, comparison with the previously reported experimental and computational data for ***R*,*R*-Ir** was also shown). We did not present relative intensities or lifetimes of the simulated emission bands based on calculated dipole transition moments, due to the significant impact of vibronic coupling and intersystem crossing rates, the simulation of which is beyond the scope of this work, but the height of the bars represents the number of close-lying in energy SOC states.

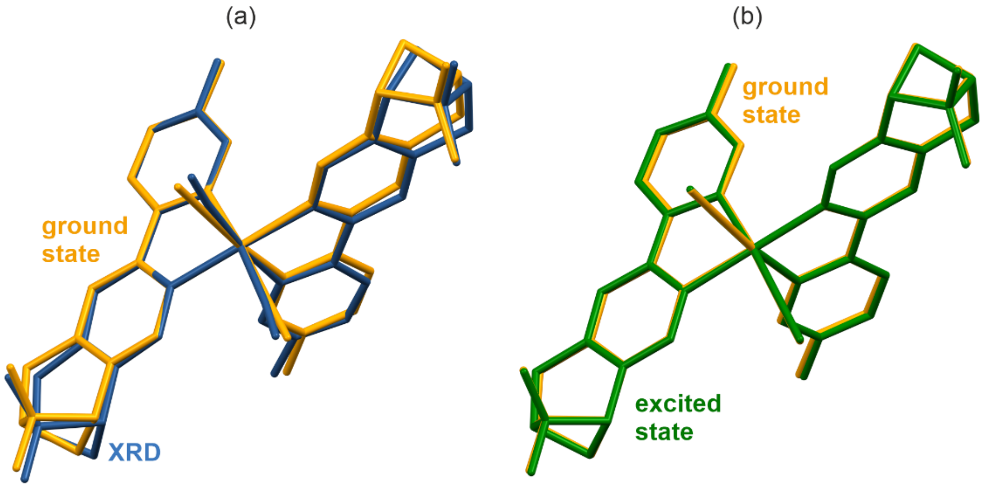

Fig. S31 Visual comparison of the experimental geometry of the $[\mathrm{Ir^{III}(CN)_2}(R,R\text{-Fpinppy})_2]^-$ complex obtained from the SC-XRD experiment for ***R*,*R*-FIr** with the optimized geometry for the ground electronic state (a) and the first excited spin-orbit state (Table S26) (b).

Table S24 The set of representative structural parameters for the $[\mathrm{Ir^{III}(CN)_2}(R,R\text{-Fpinppy})_2]^-$ complex from the experimental SC-XRD data (compound ***R*,*R*-FIr**, Fig. S4) and for DFT-optimized geometry for its ground electronic state and first excited SO-state (Table S26).

	SC-XRD model	**Optimized ground state**	**Optimized excited state**
Selected bond lengths *cis*-$[\mathrm{Ir^{III}(CN)_2}(R,R\text{-Fpinppy})_2]^-$ complexes / Å			
Ir1–C1	2.052(6)	2.056	2.069
Ir1–C2	2.057(6)	2.057	2.073
Ir1–C3	2.047(5)	2.056	2.065
Ir1–C21	2.048(6)	2.056	2.058
Ir1–N3	2.059(5)	2.070	2.087
Ir1–N4	2.051(5)	2.070	2.047
Selected angles in *cis*-$[\mathrm{Ir^{III}(CN)_2}(R,R\text{-Fpinppy})_2]^-$ complexes / °			
C1–Ir1–C2	87.9(2)	91.1	90.7
C1–Ir1–C3	93.1(2)	90.6	90.6
C1–Ir1–C21	173.5(3)	175.5	176.0
C1–Ir1–N3	91.6(2)	90.1	89.4
C1–Ir1–N4	94.1(2)	96.3	95.1
C2–Ir1–C3	173.7(2)	175.5	175.1
C2–Ir1–C21	90.5(2)	90.7	89.8
C2–Ir1–N3	93.8(2)	96.2	95.8
C2–Ir1–N4	95.3(2)	90.5	90.0
C3–Ir1–C21	89.1(2)	87.9	89.3
C3–Ir1–N3	80.0(2)	79.6	79.5
C3–Ir1–N4	90.8(2)	93.5	94.6
C21–Ir1–N3	94.8(2)	93.7	94.5
C21–Ir1–N4	79.8(2)	79.6	81.0
N3–Ir1–N4	169.4(2)	170.6	172.7
CShM parameter (Table S4)			
HP-6	30.400	29.443	29.602
PPY-6	26.347	27.690	27.514
OC-6	**0.570**	**0.486**	**0.447**
TPR-6	14.050	15.815	15.586
JPPY-6	30.239	31.370	31.174
Geometry	**OC-6**	**OC-6**	**OC-6**

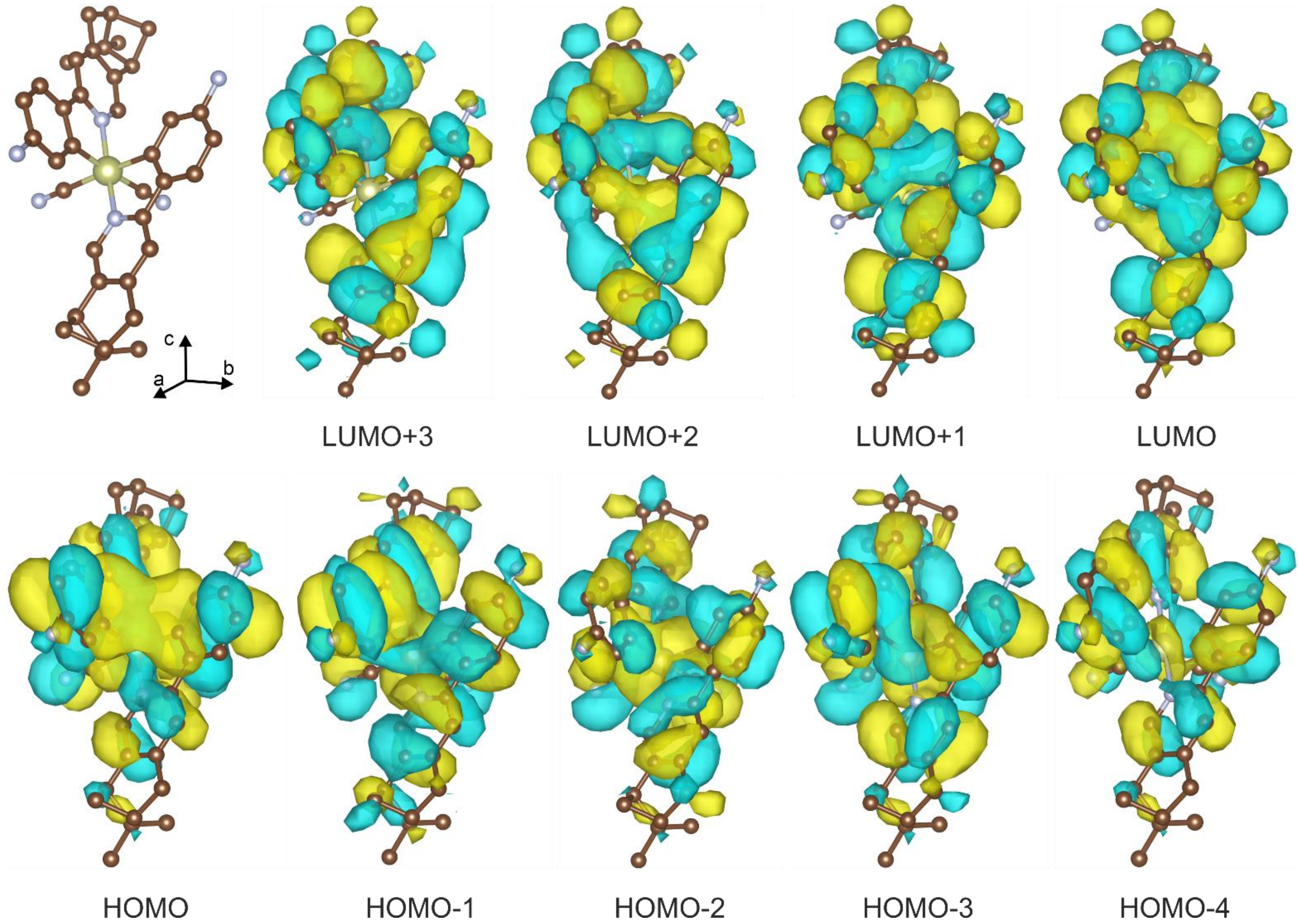

LUMO+3 LUMO+2 LUMO+1 LUMO

HOMO HOMO-1 HOMO-2 HOMO-3 HOMO-4

Fig. S32 Visualization of selected molecular orbitals for the optimized ground state of [Ir^{III}(CN)$_2$(*R*,*R*-Fpinppy)$_2$]$^-$ complexes. Hydrogen atoms were omitted for clarity. The yellow part represents a positive sign of electron density while light blue represents a negative sign. Orbitals are plotted with an isosurface level of 0.01.

Table S25 The computed energies of the five lowest-lying excited singlet and triplet states of $[\mathrm{Ir^{III}(CN)_2}(R,R\text{-Fpinppy})_2]^-$ complexes in their optimized geometry of the ground electronic state, shown together with the weights of molecular orbitals (shown in Fig. S32) that contribute to each excitation from the ground state. Each state factor greater than 0.1 was bolded.

State	Singlets		Triplets	
	Linear combination of molecular orbitals and corresponding weights	**Energy / $\mathrm{cm^{-1}}$**	**Linear combination of molecular orbitals and corresponding weights**	**Energy / $\mathrm{cm^{-1}}$**
1	HOMO-4→LUMO (0.012) **HOMO→LUMO (0.972)**	26930.6	HOMO-4→LUMO (0.063) HOMO-4→LUMO+2 (0.019) HOMO-3→LUMO+1 (0.016) HOMO-3→LUMO+3 (0.021) HOMO-2→LUMO (0.057) HOMO-1→LUMO+1 (0.256) HOMO-1→LUMO+3 (0.014) **HOMO→LUMO (0.461)**	23228.2
2	HOMO-4→LUMO+1 (0.013) **HOMO→LUMO+1 (0.971)**	27379.5	HOMO-4→LUMO+1 (0.047) HOMO-4→LUMO+3 (0.025) HOMO-3→LUMO (0.028) HOMO-3→LUMO+2 (0.018) HOMO-2→LUMO+1 (0.058) **HOMO-1→LUMO (0.333)** **HOMO→LUMO+1 (0.374)** HOMO→LUMO+3 (0.017)	23323.2
3	**HOMO-3→LUMO (0.130)** HOMO-2→LUMO+1 (0.098) **HOMO-1→LUMO (0.746)**	30286.4	HOMO-4→LUMO (0.036) HOMO-4→LUMO+2 (0.023) HOMO-3→LUMO+1 (0.048) HOMO-3→LUMO+3 (0.016) **HOMO-2→LUMO (0.181)** **HOMO-1→LUMO+1 (0.158)** **HOMO→LUMO (0.435)** HOMO→LUMO+2 (0.010)	27115.2
4	**HOMO-3→LUMO+1 (0.108)** **HOMO-2→LUMO (0.253)** **HOMO-1→LUMO+1 (0.609)**	30382.9	HOMO-4→LUMO+1 (0.012) HOMO-4→LUMO+3 (0.024) HOMO-3→LUMO (0.047) HOMO-3→LUMO+2 (0.035) **HOMO-2→LUMO+1 (0.153)** **HOMO-1→LUMO (0.145)** **HOMO→LUMO+1 (0.489)** HOMO→LUMO+3 (0.015)	27131.0
5	HOMO-4→LUMO (0.0100) HOMO-3→LUMO+1 (0.047) **HOMO-2→LUMO (0.140)** HOMO-1→LUMO+1 (0.050) **HOMO→LUMO+2 (0.734)**	30888.5	HOMO-4→LUMO (0.021) HOMO-4→LUMO+2 (0.050) HOMO-3→LUMO (0.013) HOMO-3→LUMO+1 (0.030) HOMO-3→LUMO+3 (0.041) HOMO-2→LUMO (0.067) HOMO-2→LUMO+1 (0.013) HOMO-2→LUMO+2 (0.012) HOMO-1→LUMO+1 (0.040) **HOMO-1→LUMO+3 (0.118)** **HOMO→LUMO+2 (0.509)**	28562.4

Table S26 The computed energies of singlet states and SO-states for the ground geometry of [Ir^{III}(CN)$_2$(*R*,*R*-Fpinppy)$_2$]$^-$ complexes, and the composition of SO-states in terms of singlet and triplet states for the 30 lowest-lying states.

TD-DFT (singlets)		**SOC corrected TD-DFT (mixed)**								
State	**Energy / cm^{-1}**	**State**	**Energy / cm^{-1}**	**Spin**	**State**	**Energy / cm^{-1}**	**State**	**Energy / cm^{-1}**	**State**	**Energy / cm^{-1}**
1	26930.6	1	23779.9	1 (96%)	31	31218.9	61	34368.6	90	36897.9
2	27379.5	2	23793.7	1 (96%)	32	31243.7	62	34829.8	91	37103.7
3	30286.4	3	23799.5	1 (97%)	33	31258.4	63	34897.4	92	37184.3
4	30382.9	4	23888.5	1 (95%)	34	31399.5	64	34943.8	93	37350.8
5	30888.5	5	23901.7	1 (96%)	35	31422.6	65	35182	94	37368.3
6	31221.6	6	23910.5	1 (97%)	36	31980.4	66	35208.1	95	37369.9
7	31747.9	7	26466.1	0 (50%) 1 (41%)	37	32009.2	67	35280.4	96	37474.6
8	32335.3	8	26645.5	0 (41%) 1 (50%)	38	32063.8	68	35599.7	97	37538.8
9	32855.3	9	27206.7	0 (3%) 1 (88%)	39	32197.1	69	35860.7	98	37587
10	33059.2	10	27208.1	0 (3%) 1 (85%)	40	32236.3	70	35937.2	99	37625.3
11	34243.8	11	27252.3	1 (93%)	41	32321.5	71	35945.3	100	37701.3
12	34446.2	12	27255.5	0 (6%) 1 (88%)	42	32363.3	72	35955.2	101	37926.4
13	35088.5	13	27772.9	0 (28%) 1 (66%)	43	32622.8	73	36026.5	102	38237.8
14	35356.1	14	28003.2	0 (29%) 1 (65%)	44	32799.1	74	36144	103	38533
15	35933.5	15	29093.6	0 (5%) 1 (85%)	45	33085.1	75	36184.2	104	38623.6
16	36248.7	16	29098.4	1(90%)	46	33113.4	76	36194.3	105	38757.8
17	36656.1	17	29131.2	0 (4%) 1 (90%)	47	33161.2	77	36212.8	106	38767.1
18	36892.9	18	29200.4	0 (16%) 1 (74%)	48	33185.4	78	36339.9	107	38789.8
19	36940.3	19	29355.7	0 (14%) 1 (81%)	49	33221	79	36399.8	108	38809.7
20	37422.3	20	29407.6	0 (1%) 1 (92%)	50	33243.4	80	36451.9	109	38840.5
21	37907.2	21	29504.2	0 (3%) 1 (90%)	51	33708.6	81	36454.6	110	38862.1
22	37975.4	22	29518.4	0 (9%) 1 (83%)	52	33806.7	82	36600.1	111	39093.1
23	38557.3	23	29550.1	0 (1%) 1 (91%)	53	33847.8	83	36607.4	112	39253
24	39679.3	24	29898.9	0 (2%) 1 (85%)	54	33938.2	84	36653.5	113	39265
25	39796	25	29960.8	0 (2%) 1 (89%)	55	33957.5	85	36668.2	114	39295.6
26	39803.9	26	29993.1	1 (89%)	56	34011.6	86	36766.3	115	39377.8
27	40154.7	27	30619.1	0 (30%) 1 (56%)	57	34022.8	87	36801.7	116	39392.1
28	40324.7	28	30775.7	0 (14%) 1 (75%)	58	34122.4	88	36806.8	117	39401.5
29	40612.1	29	30893	0 (40%) 1 (49%)	59	34130.7	89	36871	118	39499.6
30	40756.6	30	31079.2	1 (85%)	60	34362.1	90	36897.9	119	39508.5

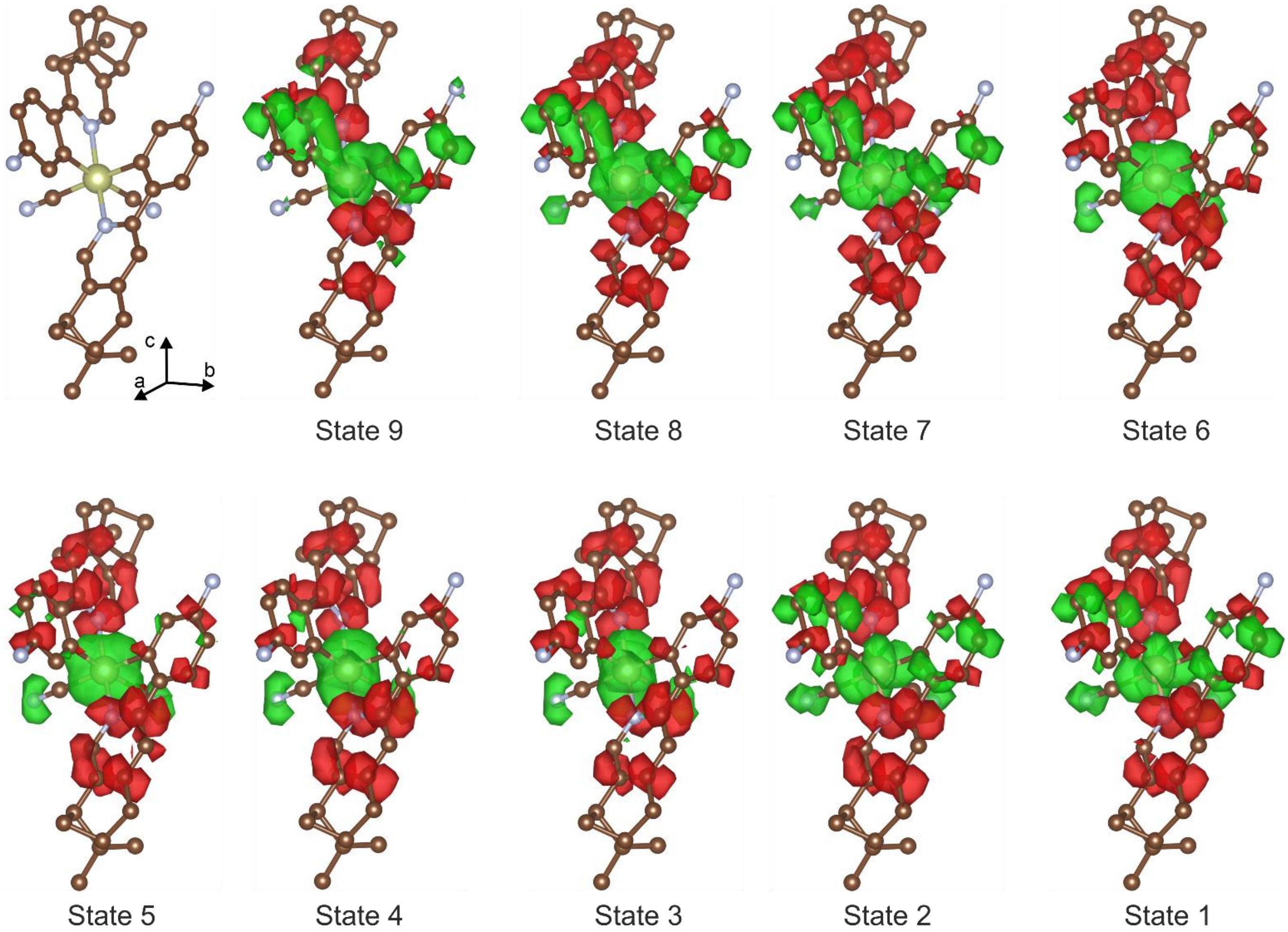

State 9 State 8 State 7 State 6

State 5 State 4 State 3 State 2 State 1

Fig. S33 The difference electron density maps of the nine lowest SO-states for the ground state geometry of $[\mathrm{Ir}^{\mathrm{III}}(\mathrm{CN})_2(R,R\text{-Fpinppy})_2]^-$ complexes. The red color represents the positive (build-up) change in electron density, and the green represents the negative change (outflow) of electron density. Hydrogen atoms were omitted for clarity. The densities were plotted with an isosurface level of 0.00125.

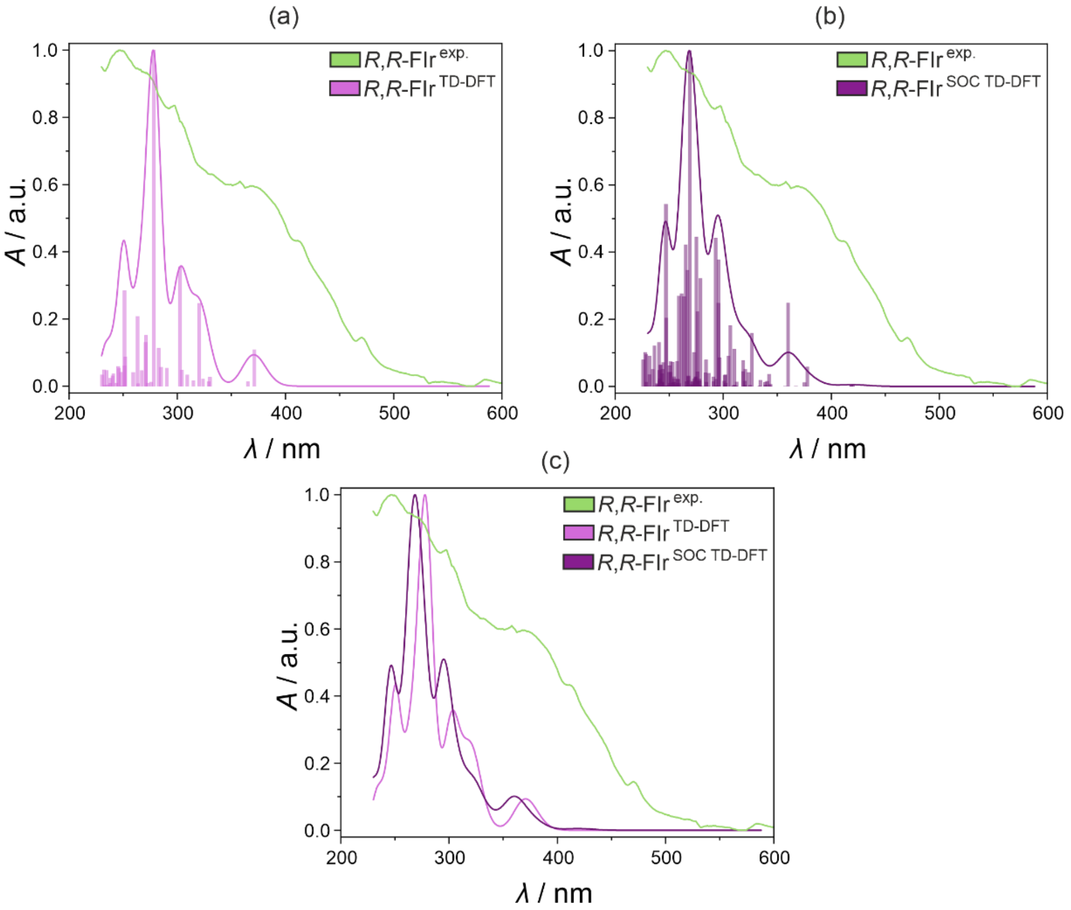

Fig. S34 Comparison of the experimental solid-state UV-vis absorption spectra of ***R*,*R*-FIr**, containing $[\mathrm{Ir^{III}(CN)_2}(R,R\text{-Fpinppy})_2]^-$ ions, with the calculated spectra for these complexes, including the comparison between the experiment and the results from the TD-DFT approach (a), the comparison between the experiment and the results from the TD-DFT with the involved SOC (b), and the comparison between the experiment and both mentioned computational approaches (c). In parts (a) and (b), the colored bars represent individual calculated excited states and the relative intensity of the related transitions from the ground state, while the solid lines represent the calculated spectrum from these transitions. In part (c), only the final calculated spectra are shown.

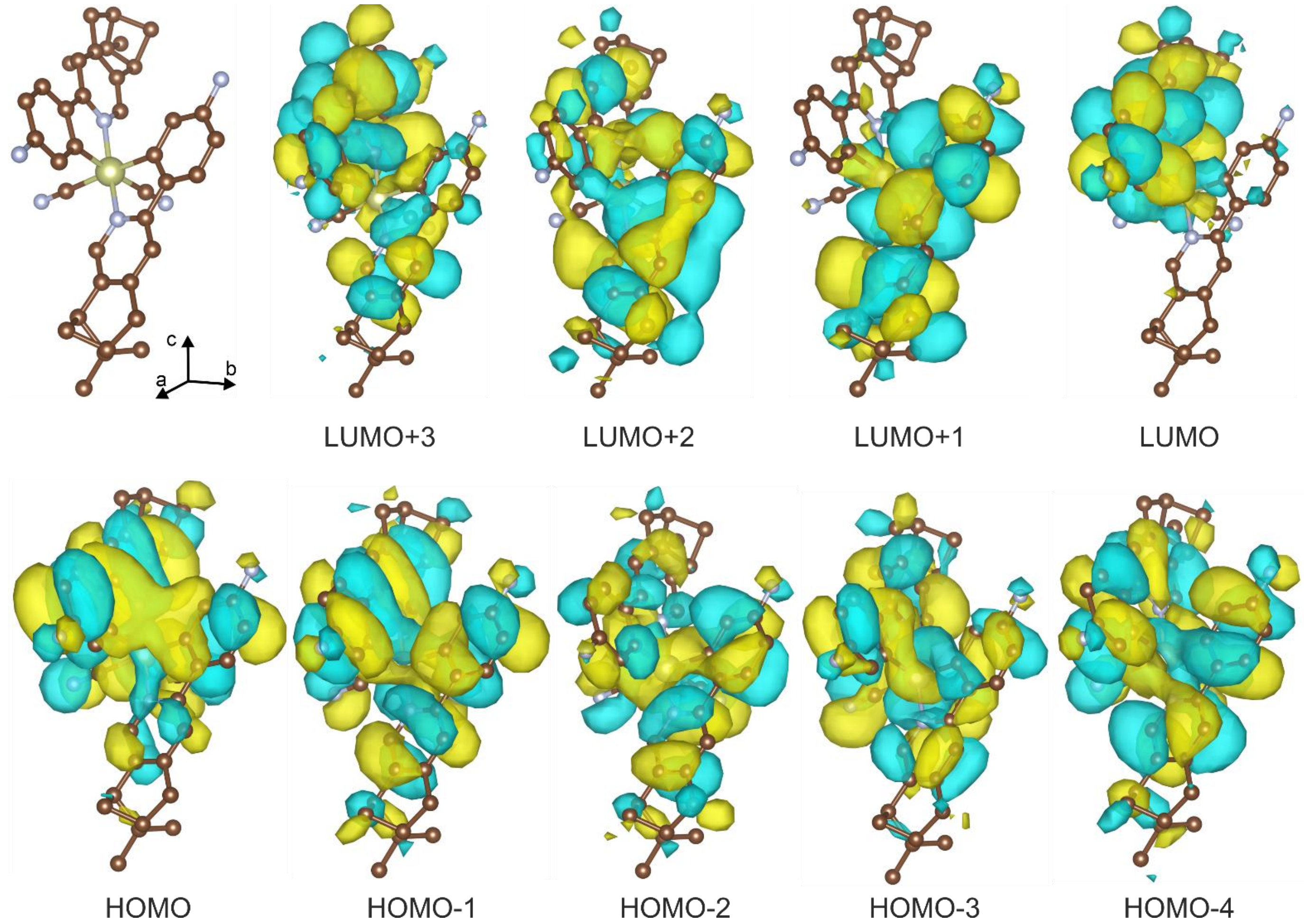

Fig. S35 Visualization of selected molecular orbitals for the optimized excited state (i.e., the first excited SO-state, Table S26) of $[\mathrm{Ir^{III}(CN)_2}(R,R\text{-Fpinppy})_2]^-$ complexes. Hydrogen atoms were omitted for clarity. The yellow part represents a positive sign of electron density, while light blue represents a negative sign. Orbitals are plotted with an isosurface level of 0.01.

Table S27 The computed energies of the five lowest-lying excited singlet and triplet states of $[\mathrm{Ir^{III}(CN)_2}(R,R\text{-Fpinppy})_2]^-$ complexes in their optimized geometry of the first excited electronic state (S0-state, Table S26), shown together with the weights of molecular orbitals (shown in Fig. S35) that contribute to each excitation from the ground state. Each state factor greater than 0.1 was bolded.

State	Singlets Linear combination of molecular orbitals and corresponding weights	Energy / cm^{-1}	Triplets Linear combination of molecular orbitals and corresponding weights	Energy / cm^{-1}
1	HOMO-4→LUMO (0.015) HOMO-1→LUMO (0.012) **HOMO→LUMO (0.959)**	23677.0	HOMO-4 → LUMO (0.017) HOMO-1 → LUMO (0.207) **HOMO → LUMO (0.692)**	17588.9
2	HOMO-1→LUMO+1 (0.034) **HOMO→LUMO+1 (0.934)**	26584.8	HOMO-4 → LUMO+1 (0.066) HOMO-4 → LUMO+2 (0.028) **HOMO-2 → LUMO+1 (0.132)** HOMO-1 → LUMO (0.0206) HOMO-1 → LUMO+1 (0.374) HOMO-1 → LUMO+2 (0.014) **HOMO → LUMO+1 (0.234)**	23070.3
3	HOMO-3→LUMO (0.081) HOMO-2→LUMO (0.045) **HOMO-1→LUMO (0.834)**	27249.7	HOMO-5 → LUMO (0.018) HOMO-4 → LUMO (0.044) HOMO-3 → LUMO (0.034) HOMO-2 → LUMO (0.077) **HOMO-1 → LUMO (0.531)** HOMO-1 → LUMO+1 (0.012) **HOMO → LUMO (0.237)**	24446.3
4	HOMO-4→LUMO (0.039) **HOMO-2→LUMO (0.862)** HOMO-1→LUMO (0.063)	28326.6	HOMO-8 → LUMO (0.024) **HOMO-4 → LUMO (0.108)** **HOMO-3 → LUMO (0.415)** **HOMO-2 → LUMO (0.136)** HOMO-1 → LUMO+2 (0.013) HOMO-1 → LUMO+3 (0.036) HOMO → LUMO (0.0205) HOMO → LUMO+1 (0.023) HOMO → LUMO+2 (0.029) **HOMO → LUMO+3 (0.119)**	26343.9
5	**HOMO-3→LUMO (0.626)** HOMO-1→LUMO (0.048) **HOMO-1→LUMO+1 (0.208)** HOMO→LUMO+2 (0.024) HOMO→LUMO+3 (0.034)	29447.5	HOMO-4 → LUMO (0.010) HOMO-4 → LUMO+1 (0.027) HOMO-4 → LUMO+2 (0.026) HOMO-3 → LUMO (0.017) HOMO-3 → LUMO+1 (0.037) HOMO-3 → LUMO+2 (0.011) **HOMO-2 → LUMO+1 (0.160)** HOMO-1 → LUMO+1 (0.018) HOMO-1 → LUMO+2 (0.010) **HOMO → LUMO+1 (0.599)**	26658.9

Table S28 The computed energies of singlet states and SO-states for the excited-state geometry of $[\text{Ir}^{\text{III}}(\text{CN})_2(R,R\text{-Fpinppy})_2]^-$ complexes (i.e., the optimized geometry for the first excited SO-state, Table S26), and the composition of SO-states in terms of singlet and triplet states for the 30 lowest-lying states.

TD-DFT (singlets)		SOC corrected TD-DFT (mixed)								
State	Energy / cm^{-1}	State	Energy / cm^{-1}	Spin	State	Energy / cm^{-1}	State	Energy / cm^{-1}	State	Energy / cm^{-1}
1	23677.1	1	18242.2	1 (99%)	31	29483.7	61	33598.2	91	36610.6
2	26583.3	2	18243.6	1 (99%)	32	30133.4	62	33678.7	92	36715.1
3	27250.3	3	18248.3	1 (99%)	33	30253.9	63	33916.1	93	36805.2
4	28326.0	4	23456.8	0 (5%) 1 (91%)	34	30352.8	64	33977.7	94	37160.1
5	29446.4	5	23652.6	1 (97%)	35	30394.6	65	34028.9	95	37243.3
6	29487.2	6	23663.1	1 (97%)	36	30456.9	66	34148.2	96	37290.8
7	30721.8	7	23683.1	0 (61%) 1 (31%)	37	30525.1	67	34251	97	37327.7
8	31409.9	8	24429.6	0 (6%) 1 (87%)	38	30562.5	68	34305.8	98	37464.7
9	31703.4	9	24437.3	0 (1%) 1 (95%)	39	30647.6	69	34344	99	37525.3
10	32119.5	10	24925.7	0 (24%) 1 (70%)	40	30937.3	70	34450.3	100	37581
11	32333.4	11	26279.9	0 (51%) 1 (43%)	41	31661.6	71	34509.6	101	37627.2
12	33470.3	12	26577.1	0 (25%) 1 (70%)	42	31884.8	72	34555.6	102	37664.7
13	33826.1	13	26854.1	0 (7%) 1 (85%)	43	31914.9	73	34602.8	103	37679.9
14	34210.4	14	26859.6	1 (94%)	44	31939	74	34795.4	104	37748.6
15	34969.6	15	27088.5	0 (22%) 1 (72%)	45	32205.1	75	35086.3	105	37830.9
16	35201.5	16	27103.2	0 (1%) 1 (94%)	46	32285.9	76	35243.8	106	38084.3
17	35520.4	17	27284.7	0 (9%) 1 (84%)	47	32370.6	77	35266.8	107	38106.1
18	36488.1	18	27922.3	0 (26%) 1 (70%)	48	32433.4	78	35302.8	108	38140.2
19	36857.7	19	28267.4	1 (96%)	49	32573.8	79	35428.5	109	38173.3
20	36978.1	20	28296	0 (5%) 1 (88%)	50	32651.5	80	35440.7	110	38209.3
21	37579.3	21	28439.1	0 (31%) 1 (62%)	51	32657.9	81	35487.7	111	38263.8
22	37754.7	22	28629.5	0 (30%) 1 (64%)	52	32823.4	82	35727.4	112	38410.2
23	38016.3	23	28942	0 (7%) 1 (83%)	53	33029.5	83	35754.8	113	38498.4
24	38249.3	24	28971.5	0 (2%) 1 (88%)	54	33112.5	84	35854.8	114	38801.8
25	38628.0	25	29124	0 (9%) 1 (85%)	55	33125.7	85	36006.4	115	38929.7
26	39005.9	26	29175.8	0 (2%) 1 (91%)	56	33212.7	86	36123.9	116	39030.2
27	39836.7	27	29232.5	0 (9%) 1 (82%)	57	33362.5	87	36210.2	117	39112.6
28	39913.6	28	29288.2	0 (2%) 1 (88%)	58	33375.2	88	36234.4	118	39167.7
29	40451.9	29	29358.5	1 (92%)	59	33451.9	89	36423.5	119	39183.1
30	40621.3	30	29398.1	1 (92%)	60	33545.9	90	36602.8	120	39250.5

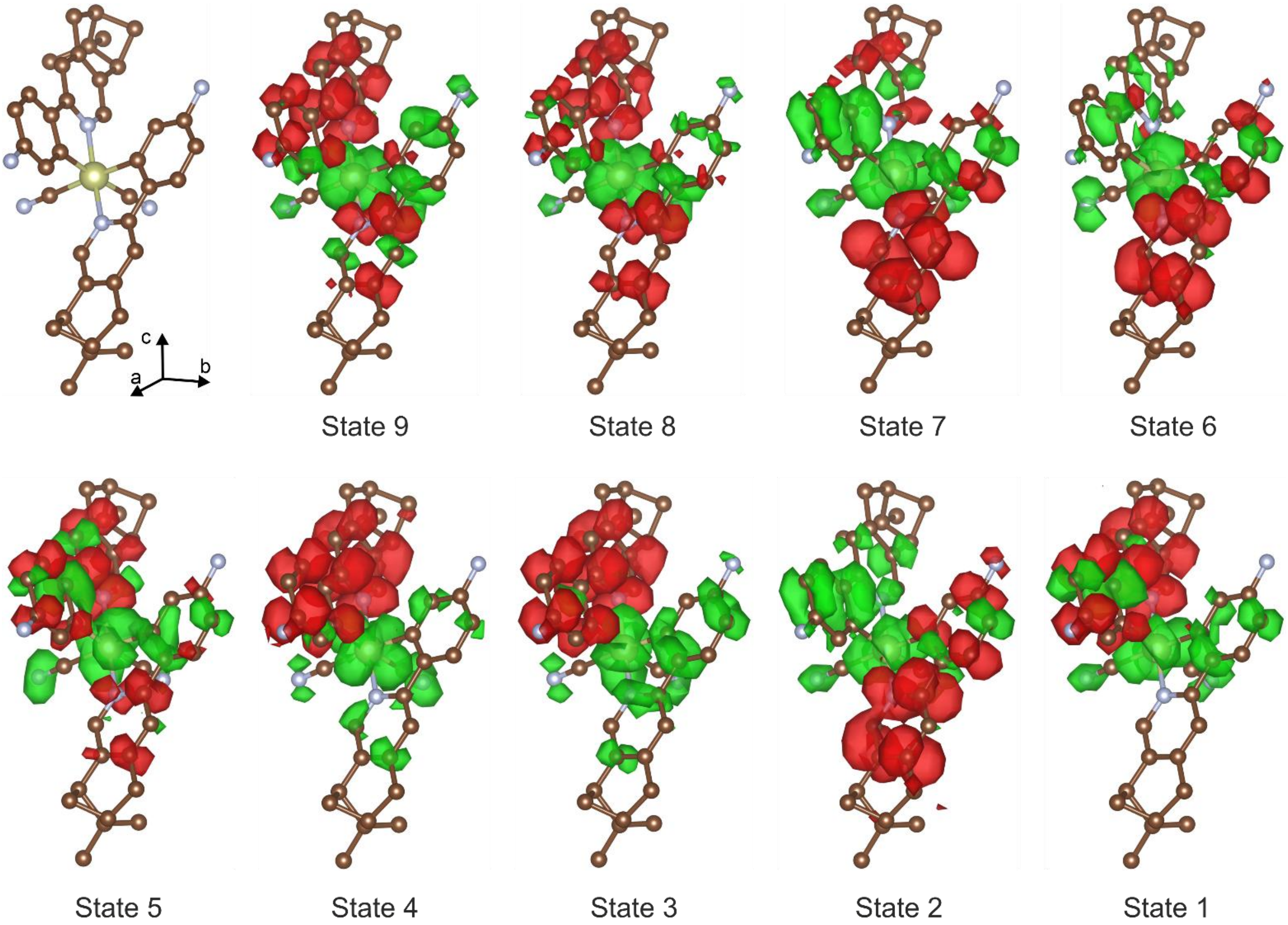

State 9 State 8 State 7 State 6

State 5 State 4 State 3 State 2 State 1

Fig. S36 The difference electron density maps of the nine lowest SO-states for the excited-state geometry of $[\mathrm{Ir}^{\mathrm{III}}(\mathrm{CN})_2(R,R\text{-Fpinppy})_2]^-$ complexes (i.e., the optimized geometry for the first excited SO-state, Table S26). The red color represents the positive (build-up) change in electron density, and the green represents the negative change (outflow) of electron density. Hydrogen atoms were omitted for clarity. The densities were plotted with an isosurface level of 0.0009.

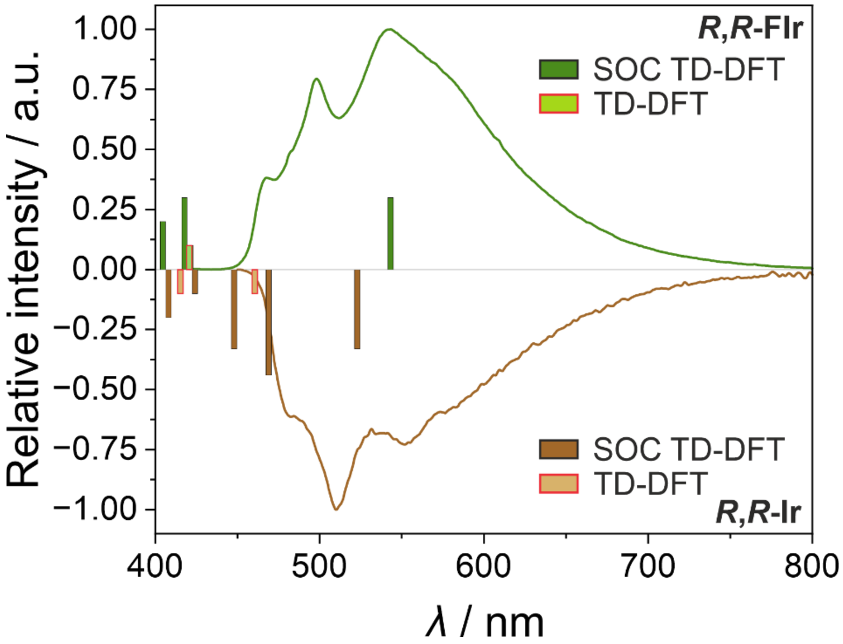

Fig. S37 Comparison of experimental room-temperature emission spectra gathered for ***R*,*R*-FIr** and the previously published ***R*,*R*-Ir**[S1] with the energies of the electronic transitions calculated TD-DFT and SOC-containing TD-DFT approaches for the optimized excited-state geometry of $[\mathrm{Ir^{III}(CN)_2}(R,R\text{-Fpinppy})_2]^-$ (for ***R*,*R*-FIr**) and $[\mathrm{Ir^{III}(CN)_2}(R,R\text{-pinppy})_2]^-$ (for ***R*,*R*-Ir**). The height of the bars is connected with the number of states with similar energy. Results for ***R*,*R*-Ir** were plotted as negative to allow for easier comparison between the compounds.

Table S29 Summary of the representative parameters characterizing luminescent thermometry in **Eu$_2$Ir$_2$** and **Eu$_2$FIr$_2$** materials, including maximal relative thermal sensitivity values ($S_{r,\mathrm{max}}$) and temperature ranges for which the S_r exceeds 1 % K^{-1} (criterion for high optical thermometric performance). The related selected temperature dependences of thermometric parameters (Δ) and subsequent thermal sensitivity are presented in Fig. 4–7 while the whole set of characteristics of optical thermometry in the mentioned materials is presented in Fig. S21–S30.

Eu$_2$Ir$_2$				**Eu$_2$FIr$_2$**			
λ_{exc} / nm	**Δ parameter**	**$S_{r,\mathrm{max}}$ / % K^{-1} (at T / K)**	**T range for S_r > 1 % K^{-1}**	**λ_{exc} / nm**	**Δ parameter**	**$S_{r,\mathrm{max}}$ / % K^{-1} (at T / K)**	**T range for S_r > 1 % K^{-1}**
Thermometry based on the emission intensity ratios							
356	$I_{593.5\,\mathrm{nm}} / I_{470.0\,\mathrm{nm}}$	1.30 (200)	160 – 270	**361**	$I_{593.5\,\mathrm{nm}} / I_{460.0\,\mathrm{nm}}$	1.26 (205)	165 – 275
	$I_{617.0\,\mathrm{nm}} / I_{470.0\,\mathrm{nm}}$	2.42 (200)	145 – 280		$I_{617.0\,\mathrm{nm}} / I_{460.0\,\mathrm{nm}}$	1.73 (210)	160 – 280
	$I_{690.0\,\mathrm{nm}} / I_{470.0\,\mathrm{nm}}$	1.18 (175)	145 – 225		$I_{690.0\,\mathrm{nm}} / I_{460.0\,\mathrm{nm}}$	1.23 (200)	160 – 260
	$I_{695.5\,\mathrm{nm}} / I_{470.0\,\mathrm{nm}}$	0.79 (175)	–		$I_{695.5\,\mathrm{nm}} / I_{460.0\,\mathrm{nm}}$	1.42 (205)	165 – 280
380	$I_{593.5\,\mathrm{nm}} / I_{470.0\,\mathrm{nm}}$	1.18 (205)	170 – 260	**380**	$I_{593.5\,\mathrm{nm}} / I_{460.0\,\mathrm{nm}}$	1.10 (220)	190 – 260
	$I_{617.0\,\mathrm{nm}} / I_{470.0\,\mathrm{nm}}$	2.92 (240)	150 – 290		$I_{617.0\,\mathrm{nm}} / I_{460.0\,\mathrm{nm}}$	1.60 (220)	170 – 280
	$I_{690.0\,\mathrm{nm}} / I_{470.0\,\mathrm{nm}}$	1.31 (185)	150 – 255		$I_{690.0\,\mathrm{nm}} / I_{460.0\,\mathrm{nm}}$	1.44 (220)	175 – 280
	$I_{695.5\,\mathrm{nm}} / I_{470.0\,\mathrm{nm}}$	152 (200)	150 – 280		$I_{695.5\,\mathrm{nm}} / I_{460.0\,\mathrm{nm}}$	1.42 (225)	180 – 280
407	$I_{593.5\,\mathrm{nm}} / I_{470.0\,\mathrm{nm}}$	0.83 (210)	–	-			
	$I_{617.0\,\mathrm{nm}} / I_{470.0\,\mathrm{nm}}$	2.26 (215)	160 – 280				
	$I_{690.0\,\mathrm{nm}} / I_{470.0\,\mathrm{nm}}$	0.60 (205)	–				
	$I_{695.5\,\mathrm{nm}} / I_{470.0\,\mathrm{nm}}$	1.26 (204)	170 – 270				
356	$I_{593.5\,\mathrm{nm}} / I_{504.5\,\mathrm{nm}}$	1.13 (200)	170 – 250	**361**	$I_{593.5\,\mathrm{nm}} / I_{492.5\,\mathrm{nm}}$	1.18 (205)	170 – 260
	$I_{617.0\,\mathrm{nm}} / I_{504.5\,\mathrm{nm}}$	2.40 (205)	150 – 280		$I_{617.0\,\mathrm{nm}} / I_{492.5\,\mathrm{nm}}$	1.63 (205)	155 – 280
	$I_{690.0\,\mathrm{nm}} / I_{504.5\,\mathrm{nm}}$	1.02 (180)	165 – 195		$I_{690.0\,\mathrm{nm}} / I_{492.5\mathrm{nm}}$	1.16 (195)	160 – 245
	$I_{695.5\,\mathrm{nm}} / I_{504.5\,\mathrm{nm}}$	0.61 (160)	–		$I_{695.5\,\mathrm{nm}} / I_{492.5\,\mathrm{nm}}$	1.33 (205)	160 – 280
380	$I_{593.5\,\mathrm{nm}} / I_{504.5\,\mathrm{nm}}$	0.97 (205)	–	**380**	$I_{593.5\,\mathrm{nm}} / I_{492.5\,\mathrm{nm}}$	0.87 (225)	–
	$I_{617.0\,\mathrm{nm}} / I_{504.5\,\mathrm{nm}}$	2.36 (215)	155 – 280		$I_{617.0\,\mathrm{nm}} / I_{492.5\,\mathrm{nm}}$	1.45 (230)	180 – 280
	$I_{690.0\,\mathrm{nm}} / I_{504.5\,\mathrm{nm}}$	1.11 (185)	155 – 225		$I_{690.0\,\mathrm{nm}} / I_{492.5\,\mathrm{nm}}$	1.24 (230)	185 – 280
	$I_{695.5\,\mathrm{nm}} / I_{504.5\,\mathrm{nm}}$	1.30 (200)	155 – 270		$I_{695.5\,\mathrm{nm}} / I_{492.5\,\mathrm{nm}}$	1.22 (235)	195 – 280
407	$I_{593.5\,\mathrm{nm}} / I_{504.5\,\mathrm{nm}}$	0.60 (210)	–	-			
	$I_{617.0\,\mathrm{nm}} / I_{504.5\,\mathrm{nm}}$	2.44 (245)	165 – 280				
	$I_{690.0\,\mathrm{nm}} / I_{504.5\,\mathrm{nm}}$	0.38 (180)	–				
	$I_{695.5\,\mathrm{nm}} / I_{504.5\,\mathrm{nm}}$	1.01 (205)	195 – 225				
Thermometry based on the ratio between integrated areas of emission bands (dependence on the bands)							
380	$A_{590\,\mathrm{nm}} / A_{\mathrm{Ir}}$	0.40 (190)	–	**380**	$A_{590\,\mathrm{nm}} / A_{\mathrm{Ir}}$	0.52 (280)	–
	$A_{617\,\mathrm{nm}} / A_{\mathrm{Ir}}$	1.86 (200)	140 – 280		$A_{617\,\mathrm{nm}} / A_{\mathrm{Ir}}$	1.32 (220)	175 – 280
	$A_{690\,\mathrm{nm}} / A_{\mathrm{Ir}}$	0.82 (180)	–		$A_{690\,\mathrm{nm}} / A_{\mathrm{Ir}}$	1.00 (235)	–
Thermometry based on the ratio between integrated areas of emission bands (dependence on the excitation)							
356	$A_{617\,\mathrm{nm}} / A_{\mathrm{Ir}}$	1.87 (195)	135 – 280	**361**	$A_{617\,\mathrm{nm}} / A_{\mathrm{Ir}}$	1.41 (195)	150 – 280
380	$A_{617\,\mathrm{nm}} / A_{\mathrm{Ir}}$	1.86 (200)	140 – 280	**380**	$A_{617\,\mathrm{nm}} / A_{\mathrm{Ir}}$	1.32 (220)	175 – 280
407	$A_{617\,\mathrm{nm}} / A_{\mathrm{Ir}}$	1.63 (215)	160 – 280				
Thermometry based on emission lifetime							
380	τ_{Ir}	1.45 (110)	78 – 171	**380**	τ_{Ir}	0.95 (80)	–
361	τ_{Eu}	1.08 (260)	238 – 260	**361**	τ_{Eu}	1.00 (280)	–

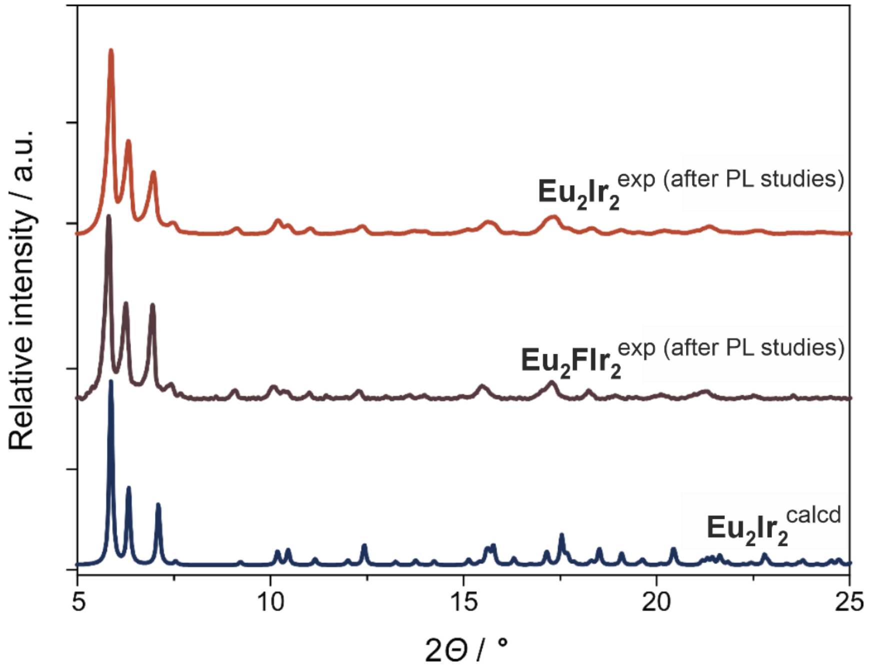

Fig. S38 Comparison of the representative parts of the experimental (exp) P-XRD patterns gathered for the polycrystalline samples of **Eu_2Ir_2** and **Eu_2FIr_2** after performing on them the full set of solid-state temperature-variable photoluminescent (PL) measurements (related to the characterization of presented optical thermometry) with the P-XRD pattern calculated (calcd) for the structural model of **Eu_2Ir_2** obtained within the single-crystal X-ray diffraction experiment.

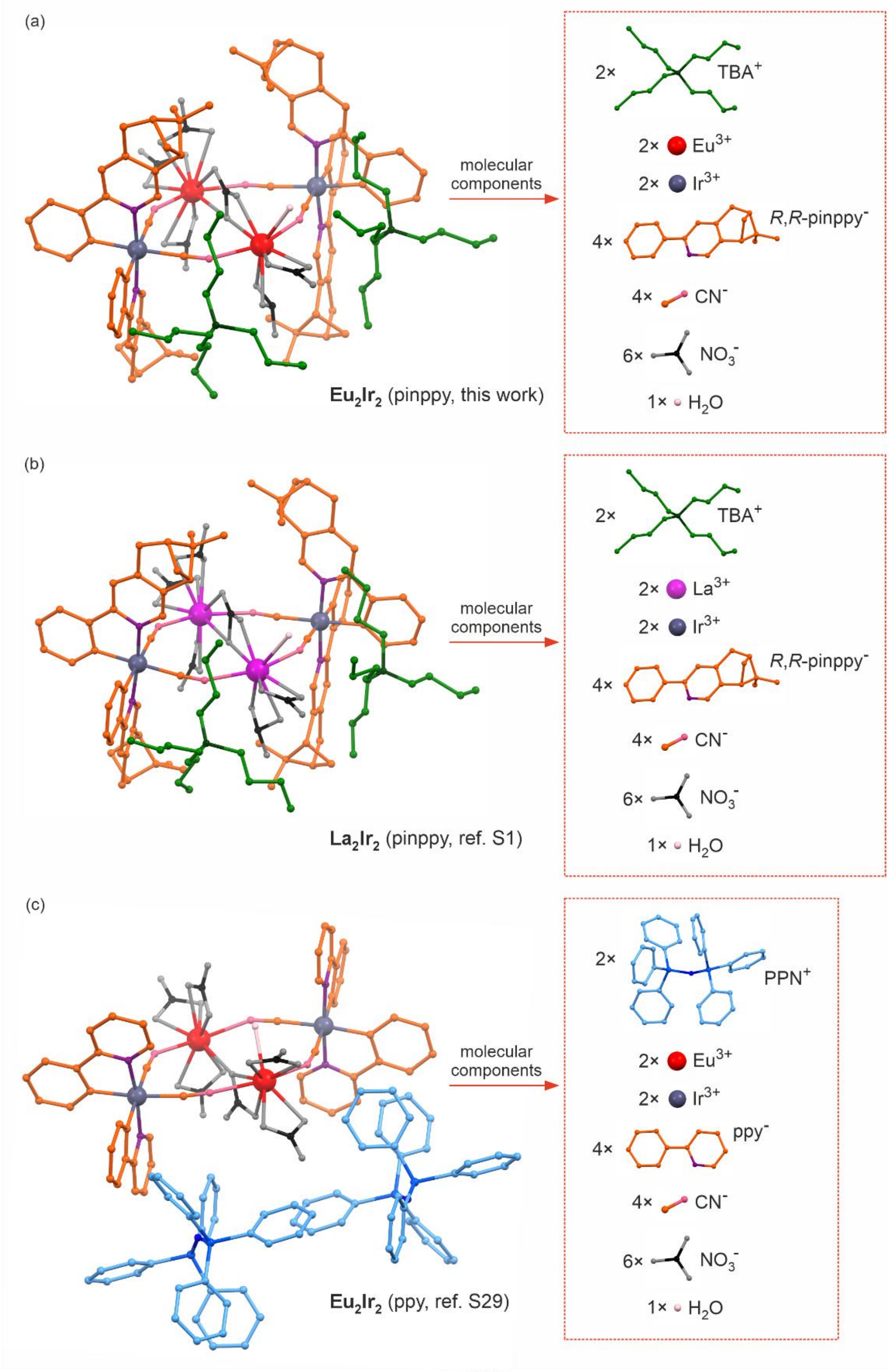

Fig. S39 Comparison of the molecular building units of the reported compound of **Eu_2Ir_2** (a) with those for the previously reported **La_2Ir_2** structural analog (b), and the previously reported closely related **Eu_2Ir_2** compound with ppy ligands used instead of *R*,*R*-pinppy as well as PPN^+ cations used instead of the TBA^+ ones (c).[S1,S29] The full formulas of the presented compounds are as follows: (a) **Eu_2Ir_2** (with pinppy, this work) – $(TBA)_2\{[Eu^{III}(NO_3)_3(H_2O)_{0.5}]_2[Ir^{III}(CN)_2(R,R\text{-pinppy})_2]_2\}\cdot 2H_2O$, (b) **$La_2Ir_2$** (with pinppy, ref. S1) – $(TBA)_2\{[La^{III}(NO_3)_3(H_2O)_{0.5}]_2[Ir^{III}(CN)_2(R,R\text{-pinppy})_2]_2\}$, (c) Eu_2Ir_2 (with ppy, ref. S29) – $(PPN)_2\{[Eu^{III}(NO_3)_3(H_2O)_{0.5}]_2[Ir^{III}(CN)_2(ppy)]_2\}\cdot 5MeCN$ (TBA = tetrabutylammonium, *R*,*R*-pinppy⁻ = a carbanion form (*R*,*R*)-2-phenyl-4,5-pinenopyridine, PPN = bis(triphenylphosphine)iminium, ppy = a carbanion of 2-phenypyridine). For the structures of (a) and (b), two alternative positions of nitrato ligands and coordinated water molecules (with partial occupancies) were found, but, for clarity, only single positions of the atoms are presented. The solvent molecules of crystallization are omitted. On the right side, all molecular components incorporated in the respective molecular building units are shown. All charged components (along with water molecules) were separately listed, and their number in the discussed molecular building unit is presented for each case. The related calculations of the overall charge of each of the illustrated compounds are included in Table S30.

Table S30 Detailed calculations of the combined charges of cationic and anionic components of the molecular building units of the reported compound of **Eu_2Ir_2**, the previously reported **La_2Ir_2** structural analog, and the previously reported closely related **Eu_2Ir_2** compound with ppy ligands used instead of *R*,*R*-pinppy as well as PPN^+ cations used instead of the TBA^+ ones.[S1,S29] The visualization of the related molecular building units is presented in Fig. S39.

Compound	**Eu_2Ir_2** (with pinppy, this work)	**La_2Ir_2** (with pinppy, ref. S1)	**Eu_2Ir_2** (with ppy, ref. S29)
Formula	$(TBA)_2\{[Eu^{III}(NO_3)_3(H_2O)_{0.5}]_2[Ir^{III}(CN)_2(R,R\text{-pinppy})_2]_2\}\cdot 2H_2O$	$(TBA)_2\{[La^{III}(NO_3)_3(H_2O)_{0.5}]_2[Ir^{III}(CN)_2(R,R\text{-pinppy})_2]_2\}$	$(PPN)_2\{[Eu^{III}(NO_3)_3(H_2O)_{0.5}]_2[Ir^{III}(CN)_2(ppy)]_2\}\cdot 5MeCN$
Figure visualizing a molecular building unit	Fig. S39a	Fig. S39b	Fig. S39c
Cationic components of a molecular building unit	2 x TBA^+	2 x TBA^+	2 x PPN^+
	2 x Eu^{3+}	2 x La^{3+}	2 x Eu^{3+}
	2 x Ir^{3+}	2 x Ir^{3+}	2 x Ir^{3+}
Combined charge of cationic components	(14+)	(14+)	(14+)
Anionic components of a molecular building unit	4 x *R*,*R*-$pinppy^-$	4 x *R*,*R*-$pinppy^-$	4 x ppy^-
	4 x CN^-	4 x CN^-	4 x CN^-
	6 x NO_3^-	6 x NO_3^-	6 x NO_3^-
Combined charge of anionic components	(14–)	(14–)	(14–)
Overall charge of a molecular building unit	0	0	0
Charge of a molecular cluster (i.e., combined molecular components of a building unit without TBA^+ counter-ions)	(2–)	(2–)	(2–)

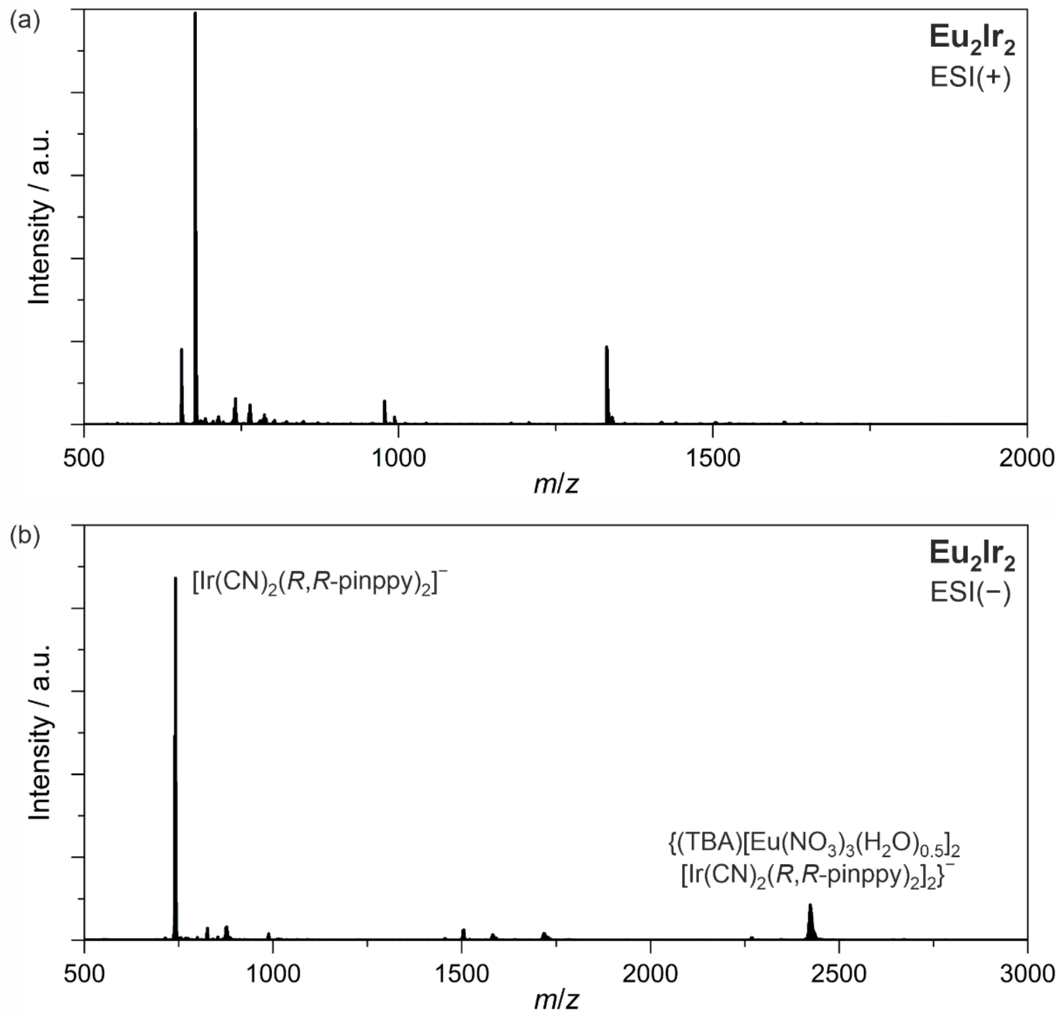

Fig. S40 ESI-TOF mass spectra (MS) for the acetonitrile solution (c = 1 mg·mL^{-1}) of **Eu$_2$Ir$_2$** in the 500–2000 m/z range for the positive ionization (a) and in the 500–3000 m/z range for the negative ionization (b). In (b), the two postulated compositions of species for the indicated m/z values were presented. The other peaks are discussed in the comment placed on the next page.

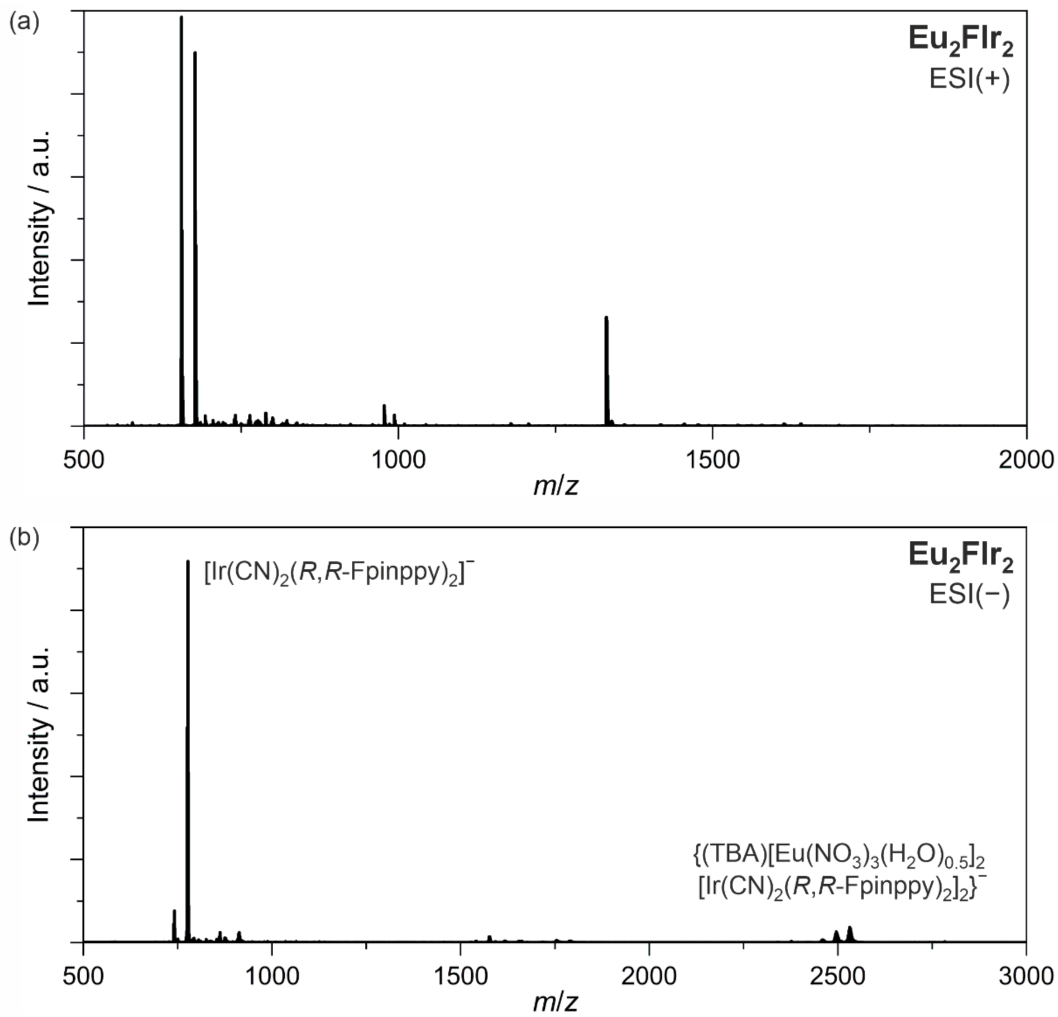

Fig. S41 ESI-TOF mass spectra (MS) for the acetonitrile solution (*c* = 1 mg·mL^{-1}) of **Eu$_2$FIr$_2$** in the 500–2000 *m*/*z* range for the positive ionization (a) and in the 500–3000 *m*/*z* range for the negative ionization (b). In (b), the two postulated compositions of species for the indicated *m*/*z* values were presented. The other peaks are discussed in the comment placed below.

Comment to Fig. S40 and S41: To collect the ESI-TOF mass spectra (MS), the air-stable powder samples of **Eu$_2$Ir$_2$** and **Eu$_2$FIr$_2$** were dissolved in pure acetonitrile (HPLC grade). The spectra were obtained for both positive and negative ionization modes. In positive ionisation, the same set of peaks with slightly amended intensity ratios is observed for both compounds (Fig. S40a and S41a, Table S31). These peaks can be mainly attributed to the presence of polynuclear Eu^{III}-based species with the mixture of nitrate anions and solvent molecules, which can form upon the decomposition of cluster species in the solution and/or during electrospray ionization. The Ir(III)-based complexes do not contribute significantly to the part of the spectra related to the positive ionization, as there are no distinct differences between the positions of the peaks for the two compounds differing in the mass of the pinppy-type ligands coordinated to the d-block metal ion. Conversely, the negative ionization spectra for both analogues (Fig. S40b and S41b, Table S31) confirm that most of the heterometallic coordination clusters undergo decomposition, resulting in the appearance of the main peak related to the free cyclometalated dicyanido-Ir(III) complexes. Much weaker, almost residual, signals related to the whole clusters, associated with one of the tetrabutylammonium cations, can be detected in both samples at high *m*/*z* ranges. Their overall contribution to the mass spectra is minor, indicating decomposition, which presumably does not only occur during ionization but also because of their instability in pure acetonitrile.

Table S31 Comparison of the 15 most intense peaks in the mass spectra (ESI-TOF-MS) of **Eu_2Ir_2** and **Eu_2FIr_2** obtained for the solution of corresponding compounds in acetonitrile, in both the positive and negative ionization (see Fig. S40 and S41, respectively). The comment on the observed peaks is placed on the previous page.

Eu_2Ir_2				**Eu_2FIr_2**			
positive ionization		**negative ionization**		**positive ionization**		**negative ionization**	
m/z	***I***	***m/z***	***I***	***m/z***	***I***	***m/z***	***I***
676.9939	214087	**741.2415**	61067	655.0227	59090	**777.2248**	36714
677.9969	100231	**739.2387**	34434	676.9996	53940	**775.2229**	20705
1331.0169	40323	**742.2449**	26623	656.0251	28254	**778.2282**	16367
655.0169	39083	740.2427	16291	678.0026	26109	776.2258	9992
1332.0204	38834	743.2473	6291	1331.0286	15734	779.2312	3531
678.9996	25408	2423.5282	5951	1332.0326	15204	741.2425	3068
656.0199	19602	2424.5286	5475	1333.0345	7296	739.2401	1770
1333.0242	18351	2425.5282	5429	657.0288	7161	2531.4709	1488
741.059	13440	2422.5275	4838	679.0056	6549	742.2463	1347
977.8349	12161	2421.5259	4680	977.845	2987	2532.4721	1342
764.0429	10187	2426.5285	11709	1334.0369	2387	2533.4725	1335
739.0567	8387	2427.5282	3950	789.0067	1903	2529.4733	1181
1334.0237	6157	2428.5325	2982	789.2549	1865	2530.4753	1166
978.8383	5974	2420.528	2961	993.8355	1626	776.4788	1120
765.0473	5687	2419.5248	2666	741.0668	1601	2534.4753	1106

Comment on the negative charge of *R*,*R*-pinppy and *R*,*R*-Fpinppy ligands within Ir(III) complexes in reported materials and their molecular precursors

It is important to clarify that both in the reported materials of **Eu_2Ir_2** and **Eu_2FIr_2**, as well as in their molecular precursors of ***R*,*R*-Ir** and ***R*,*R*-FIr**, the organic ligands of *R*,*R*-pinppyH and *R*,*R*-FpinppyH exist in the negatively charged (1–) forms, which we abbreviate as *R*,*R*-pinppy and *R*,*R*-Fpinppy, respectively. These ligands are initially obtained in the neutral forms as visualized in Scheme 1 (main article) and a detailed scheme in the Experimental details. They both consist of a pinene-functionalized pyridine ring combined by a C–C bond with a phenyl ring (a fluorinated phenyl ring for the case of *R*,*R*-FpinppyH). However, upon the formation of Ir(III) complexes, the C–H activation of one of the C–H bonds of the phenyl ring is induced. The C–H activation occurs on the C–H group of a phenyl ring that is the closest to the pyridine ring, and this process is strictly related to the concomitant occurrence of the cyclometalation leading to the C,N-bidentate coordination of deprotonated *R*,*R*-pinppy and *R*,*R*-Fpinppy ligands to the Ir(III) centers. In other words, the formation of cyclometalated Ir(III) complexes is related to the appearance of the carbanion form of *R*,*R*-pinppyH and *R*,*R*-FpinppyH ligands, i.e., the generation of negatively charged *R*,*R*-pinppy$^-$ and *R*,*R*-Fpinppy$^-$ ligands.

The confirmation of the appearance of the key C–Ir bond is given by the SC-XRD experiments on the molecular precursors of ***R*,*R*-Ir** and ***R*,*R*-FIr**, and further a main heterometallic material of **Eu_2Ir_2** (Fig. 1, S4, and S5, as well as ref. S1). The related structural models undoubtedly indicate the presence of short C–Ir distances (2.05–2.06 Å), which are very close to the analogous N–Ir bonds for the coordinated pyridine part of the ligands, as typically observed for cyclometalated Ir(III) complexes bearing a carboanion form of 2-phenylpyridine (or its derivatives) as a ligand.[S30–S49] In this context, it is important to state that such a C–H activation of 2-phenylpyridine-type ligands occurring upon the cyclometalation and formation of Ir(III) complexes is broadly observed and is one of the most extensively studied as a source of variously functionalized cyclometalated Ir(III) complexes, mainly for their optical and optoelectronic properties.[S30–S49] For instance, the archetypal organo-iridium(III) complex, i.e., $[Ir^{III}(ppy)_3]^0$, which was reported as one of the very first high-performance electroluminescent metal complexes,[S30,S49,S50] is based on three 2-phenylpyridine ligands in their deprotonated (carbanion) forms (ppy$^-$) coordinated to the Ir(III) center. This type of the C–H activation of 2-phenylpyridine leading to its carbanion form is also observed for many other metal centers, such as Pt(II), Au(III), or Ru(II).[S51–S53] It can be considered as one of the main reactions utilized for organometallic complexes of transition metal ions, especially those explored for their broad optical and optoelectronic applications.[S30–S53] In Fig. S42, the representative set of the published cyclometalated Ir(III) complexes bearing the carbanion forms of the various derivatives of 2-phenylpyridine is shown to support the above-presented discussion. Following this discussion, everywhere in the article, we use the abbreviations of *R*,*R*-pinppyH and *R*,*R*-FpinppyH for the as-synthesized neutral forms of the 2-phenylpyridine derivatives, whereas the abbreviations of *R*,*R*-pinppy and *R*,*R*-Fpinppy are used for the carbanion forms of the respective ligands.

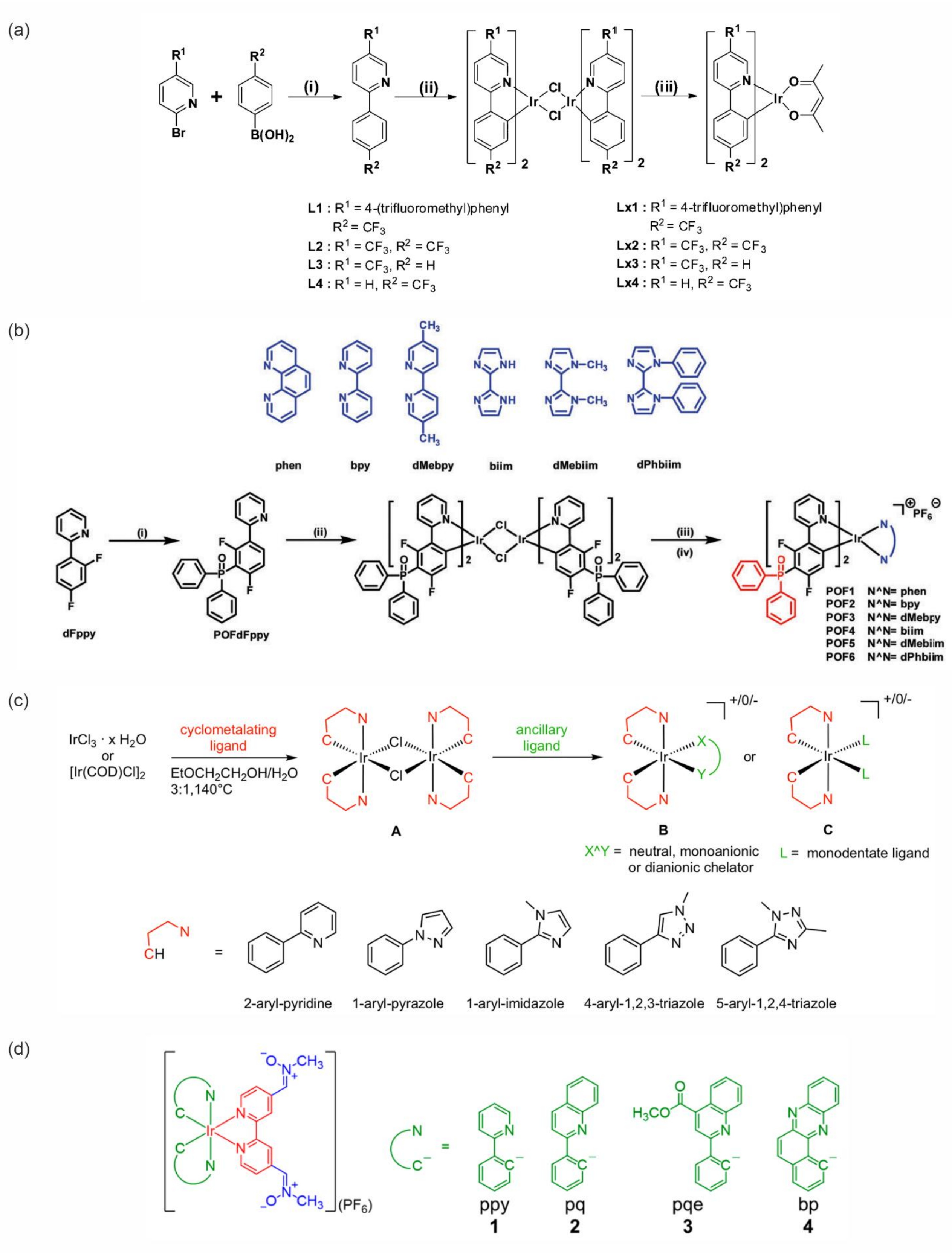

Fig. S42 The representative set of published cyclometalated Ir(III) complexes bearing the carbanion form of 2-phenylpyridine and its derivatives, including trifluoromethyl-substituted 2-phenylpyridine with acetyloacetonate co-ligands (a),[S32] diphenylphosphoryl-substituted 2-phenylpyridine with N,N-bidentate co-ligands (b),[S33] 2-arylpyrydine and its analogs with other N-containing aromatic rings used instead of pyridine with various co-ligands (c),[S39] and 2-phenylpyriidne and their more extended analogs with bis-nitrone-containing co-ligands (d).[S40] Part (a) was reproduced from Ref. S32 with permission from the Royal Society of Chemistry. Part (b) was reproduced from Ref. S33 with permission from the Royal Society of Chemistry. Part (c) was adapted under terms of the CC-BY license, ref. S39. Part (d) was adapted with permission from Ref. S40. Copyright 2024 American Chemical Society.

References to Supporting Information

S1 J. Rzepiela, M. Liberka, M. Zychowicz, J. Wang, H. Tokoro, K. Piotrowska, S. Baś, S. Ohkoshi and S. Chorazy, *Inorg. Chem. Front.*, 2024, **11**, 1366–1380.

S2 G. M. Sheldrick, *Acta Crystallogr., Sect. A: Found. Adv.,* 2015, **71**, 3–8.

S3 L. J. Farrugia, *J. Appl. Crystallogr.,* 2012, **45**, 849–854.

S4 R. Jankowski, J. J. Zakrzewski, M. Zychowicz, J. Wang, Y. Oki, S. Ohkoshi, S. Chorazy and B. Sieklucka, *J. Mater. Chem. C*, 2021, **9**, 10705−10717.

S5 S. Chorazy, J. J. Zakrzewski, J. Wang, S. Ohkoshi and B. Sieklucka, *CrysEngComm*, 2018, **20**, 5695–5706.

S6 M. Liberka, M. Zychowicz and S. Chorazy, *Inorg. Chem. Front*., 2024, **11**, 2081–2097.

S7 M. Llunell, D. Casanova, J. Cirera, J. Bofill, P. Alemany, S. Alvarez, M. Pinsky and D. Avnir. *SHAPE v. 2.1. Program for the Calculation of Continuous Shape Measures of Polygonal and Polyhedral Molecular Fragments*, University of Barcelona: Barcelona, Spain, 2013.

S8 D. Casanova, J. Cirera, M. Llunell, P. Alemany, D. Avnir and S. Alvarez, *J. Am. Chem. Soc.*, 2004, **126**, 1755–1763.

S9 A. Ruiz-Martínez, D. Casanova and S. Alvarez, *Chem. Eur. J.,* 2008, **14**, 1291–1303.

S10 A. Ruiz-Martínez and S. Alvarez. *Chem. Eur. J.*, 2009, **15**, 7470–7480.

S11 D. A. Kleinman, *Phys. Rev.,* 1962, **128**. 1761–1775.

S12 D. A. Kleinman, *Phys. Rev.,* 1977, **126**. 1977–1979.

S13 H.-J. Zhao, Y.-F. Zhang and L. Chen, *J. Am. Chem. Soc.,* 2012, **134**, 1993–1995.

S14 G. R. Crane and J. G. Bergman, *J. Chem. Phys.,* 1976, **64**, 27–29.

S15 C. A. Dailey, B. J. Burke and G. J. Simpson, *Chem. Phys. Lett.*, 2004, **390**, 8–13.

S16 J. Wang, J. J. Zakrzewski, M. Zychowicz, Y. Xin, H. Tokoro, S. Chorazy and S. Ohkoshi, *Angew. Chem. Int. Ed*., 2023, **62**, e202306372.

S17 F. Neese, *WIRES Comput. Mol. Sci.*, 2022, **12**, e1606.

S18 K. Momma and F. Izumi, *J. Appl. Crystallogr.*, 2011, **44**, 1272–1276.

S19 F. Weigend and R. Ahlrichs, *Phys. Chem. Chem. Phys.*, 2005, **7**, 3297–3305.

S20 E. Caldeweyher, S. Ehlert, A. Hansen, H. Neugebauer, S. Spicher, C. Bannwarth and S. Grimme, *J. Chem. Phys.*, 2019, **150**, 154122.

S21 R. Cammi, B. Mennucci and J. Tomasi, *J. Phys. Chem. A*, 2000, **104**, 5631–5637.

S22 E. van Lenthe, E. J. Baerends and J. G. Snijders, *J. Chem. Phys.*, 1993, **99**, 4597–4610.

S23 C. van Wüllen, *J. Chem. Phys.*, 1998, **109**, 392–399.

S24 D. A. Pantazis, X.-Y. Chen, C. R. Landis and F. J. Neese, *J. Chem. Theory Comput.*, 2008, **4**, 908–919.

S25 M. Buhl, C. Reimann, D. A. Pantazis, T. Bredow and F. Neese, *J. Chem. Theory Comput.*, 2008, **4**, 1449–1459.

S26 F. Neese, F. Wennmohs, A. Hansen and U. Becker, *Chem. Phys.*, 2009, **356**, 98–109.

S27 R. Izsák and F. Neese, *J. Chem. Phys.*, 2011, **135**, 144105.

S28 F. Neese, *J. Chem. Phys.*, 2005, **122**, 034107.

S29 N. Mohd Ali, V. L. MacLeod, P. Jennison, I. V. Sazanovich, C. A. Hunter, J. A. Weinstein and M. D. Ward, *Dalton Trans.* 2012, **41**, 2408–2419.

S30 K. Dedeian, P. I. Djurovich, F. O. Garces, G. Carlson and R. J. Watts, *Inorg. Chem*. 1991, **30**, 1687–1688.

S31 P. Wang, F.-F. Wang, Y. Chen, Q. Niu, L. Lu, H.-M. Wang, X.-C. Gao, B. Wei, H.-W. Wu, X. Cai and D.-C. Zou, *J. Mater. Chem. C* 2013, **1**, 4821–4825.

S32 C. Liu, X. Lv, Y. Xing and J. Qiu, *J. Mater. Chem. C* 2015, **3**, 8010–8017.

S33 H. Yu, C. Liu, Z. Yu, L. Zhang and J. Xiu, *J. Mater. Chem. C* 2017, **5**, 3519–3527.

S34 Y. Zhang, X. Chen, D. Song, D. Zhong, X. Yang, Y. Sun, B. Liu, G. Zhou and Z. Wu, *Inorg. Chem. Front.* 2020, **7**, 1651–1666.

S35 D. Rota Martir, C. Momblona, A. Pertegas, D. B. Cordes, A. M. Z. Slawin, H. J. Bolink and E. Zysman-Colman, *ACS Appl. Mater. Interfaces* 2016, **8**, 33907–33915.

S36 A. Y. Gitlina, F. Fadaei-Tirani, A. Ruggi, C. Plaice and K. Severin, *Chem. Sci.* 2022, **13**, 10370–10374.

S37 W.-Y. Wong, N.-Y. Chau, Q. Wang, L. Jiang, J. Li and D. Ma, *J. Mater. Chem. C* 2024, **12**, 14485–14495.

S38 A. Santoro, A. M. Prokhorov, V. N. Kozhevnikov, A. C. Whitwood, B. Donnio, J. A. G. Williams and D. B. Bruce, *J. Am. Chem. Soc.* 2011, **133**, 5248–5251.

S39 F. Monti, A. Baschieri, L. Sambri and N. Armaroli, *Acc. Chem. Res.* 2021, **54**, 1492–1505.

S40 E. C.-L. Mak, Z. Chen, L. C.-C. Lee, P. K.-K. Leung, A. M.-H. Yip, J. Shum, S.-M. Yiu, V. W.-W. Yam and K. K.-W. Lo, *J. Am. Chem. Soc*. 2024, **146**, 25589–25599.

S41 E. E. Turner, D. J. Breen, G. Kosgei, L. A. Crandall, G. M. Curtin, E. Jakubikova, R. M. O'Donnell, C. J. Ziegler and J. J. Rack, *Inorg. Chem*. 2022, **61**, 18842–18849.

S42 J.-X. Xie, C.-C. Lee, L.-M. Huang, H.-T. Lin, D. Luo, C.-H. Hsieh, S.-W. Liu and C.-H. Chen, *ACS Appl. Mater. Interfaces* 2023, **15**, 44022–44032.

S43 M. S. Lowry, J. I. Goldsmith, J. D. Slinker, R. Rohl, R. A. Pascal Jr., G. G. Malliaras and S. Bernhard, *Chem. Mater*. 2005, **17**, 5712–5719.

S44 X. Liu, J. Liu, D. Zhu, X. Yan, J. Chen, L. Duan, Y. Kang and D. Ma, *J. Am. Chem. Soc*. 2024, **146**, 29955–29963.

S45 S. Lamansky, P. Djurovich, D. Murphy, F. Abdel-Razzaq, R. Kwong, I. Tsyba, M. Bortz, B. Mui, R. Bau and M. E. Thompson, *Inorg. Chem*. 2001, **40**, 1704–1711.

S46 B. Schmid, F. O. Garces and R. J. Watts, *Inorg. Chem.* 1994, **33**, 9–14.

S47 A. Nakagawa, Y. Hisamatsu, S. Moromizato, M. Kohno and S. Aoki, *Inorg. Chem*. 2014, **53**, 409–422.

S48 T. U. Connell, C. L. Fraser, M. L. Czyz, Z. M. Smith, D. J. Hayne, E. H. Doeven, J. Agugiaro, D. J. D. Wilson, J. L. Adcock, A. D. Scully, D. E. Gomez, N. W. Barnett, A. Polyzos and P. S. Francis, *J. Am. Chem. Soc.* 2019, **141**, 17646–17658.

S49 T. Hofbeck and H. Yersin, *Inorg. Chem.* 2010, **49**, 9290–9299.

S50 Y. Kawamura, K. Goushi, J. Brooks, J. J. Brown, H. Sasabe and C. Adachi, *Appl. Phys. Lett.* 2005, **86**, 071104.

S51 J. Wu, B. Xu, Y. Xu, L. Yue, J. Chen, G. Xie and J. Zhao, *Inorg. Chem.* 2023, **62**, 19142–19152.

S52 V. K.-M. Au, K. M.-C. Wong, N. Zhu and V. W.-W. Yam, *Chem. Eur. J*. 2011, **17**, 130–142.

S53 B. Pena, N. A. Leed, K. R. Dunbar and C. Turro, *J. Phys. Chem. C* 2012, **116**, 22186–22195.